POLYPUBLIE
Polytechnique Montréal

POLYTECHNIQUE MONTRÉAL

UNIVERSITÉ D'INGÉNIERIE

Titre: Title:	3D Interlock Composites Multi-Scale Viscoelastic Model Development, Characterization and Modeling
Auteur: Author:	Alice Courtois
Date:	2018
Type:	Mémoire ou thèse / Dissertation or Thesis
Référence: Citation:	Courtois, A. (2018). 3D Interlock Composites Multi-Scale Viscoelastic Model Development, Characterization and Modeling [Thèse de doctorat, École Polytechnique de Montréal]. PolyPublie. https://publications.polymtl.ca/3178/

Document en libre accès dans PolyPublie
Open Access document in PolyPublie

URL de PolyPublie: PolyPublie URL:	https://publications.polymtl.ca/3178/
Directeurs de recherche: Advisors:	Martin Lévesque, & Edu Ruiz
Programme: Program:	Génie mécanique

UNIVERSITÉ DE MONTRÉAL

3D INTERLOCK COMPOSITES MULTI-SCALE VISCOELASTIC MODEL
DEVELOPMENT, CHARACTERIZATION AND MODELING

ALICE COURTOIS
DÉPARTEMENT DE GÉNIE MÉCANIQUE
ÉCOLE POLYTECHNIQUE DE MONTRÉAL

THÈSE PRÉSENTÉE EN VUE DE L'OBTENTION
DU DIPLÔME DE PHILOSOPHIÆ DOCTOR
(GÉNIE MÉCANIQUE)
JUIN 2018

UNIVERSITÉ DE MONTRÉAL

ÉCOLE POLYTECHNIQUE DE MONTRÉAL

Cette thèse intitulée :

3D INTERLOCK COMPOSITES MULTI-SCALE VISCOELASTIC MODEL
DEVELOPMENT, CHARACTERIZATION AND MODELING

présentée par : COURTOIS Alice
en vue de l'obtention du diplôme de : Philosophiæ Doctor
a été dûment acceptée par le jury d'examen constitué de :

M. THERRIAULT Daniel, Ph. D., président
M. LÉVESQUE Martin, Ph. D., membre et directeur de recherche
M. RUIZ Eduardo Antonio Julian, Ph. D., membre et codirecteur de recherche
Mme MULIANA Anastasia, Ph. D., membre
M. LAHELLEC Noël, Ph. D., membre externe

DEDICATION

To my family,

À ma famille,

ACKNOWLEDGEMENTS

RÉSUMÉ

Les matériaux composites, et plus particulièrement les composites à renforts tridimensionnels (3D), sont de plus en plus utilisés dans l'industrie aérospatiale. En effet, les renforts 3D ont été développés afin d'améliorer les propriétés hors-plan ainsi que la résistance à l'impact et au délaminage. Les composites à renforts 3D sont généralement fabriqués par transfert de résine (Resin transfer Molding, RTM). Cependant, le développement de contraintes résiduelles dans les pièces est intrinsèque au procédé de fabrication et peut induire des déformations géométriques. Ces contraintes résiduelles et ces déformations résultantes peuvent par la suite affecter les performances des pièces fabriquées. C'est pourquoi des outils numériques ont été développés pour prédire le développement des contraintes résiduelles pendant la fabrication. La précision de ces outils dépend, cependant, des modèles matériaux utilisés. En effet, les modèles doivent tenir compte de l'évolution de la température et du degré de polymérisation du matériau au cours du procédé de fabrication pour réussir à prédire précisément le développement des contraintes résiduelles et les déformations géométriques résultantes.

Cette thèse porte sur le développement d'un modèle viscoélastique linéaire thermodynamiquement admissible prédisant le comportement mécanique d'un matériau composite à renfort tissé 3D interlock, en fonction de la température et du degré de polymérisation. Le comportement vicsoélastique a été attribué entièrement à la résine. Le modèle a donc tout d'abord été développé pour prédire le comportement viscoélastique de la résine pure. Il a ensuite été étendu par homogénéisation afin de modéliser le comportement des torons de chaine et de trame. Finalement, suite à une seconde procédure d'homogénéisation, le modèle a été généralisé pour prédire les propriétés homogénéisées du composite. Ce modèle a été implémenté par une autre étudiante au doctorat dans un outil de calcul afin de prédire l'évolution des contraintes résiduelles au cours de la fabrication par RTM de pièces structurales en composites tissés 3D et permet de modéliser adéquatement le comportement viscoélastique qui apparait lors de la post-cuisson.

Une campagne expérimentale a d'abord été menée afin d'évaluer le comportement viscoélastique linéaire de la résine pure. Des échantillons entièrement et partiellement polymérisés ont été fabriqués (sept degrés de polymérisation différents à partir du point de gel) puis testés en flexion trois points dans une DMA (Dynamic Mechanical Analyser). Des essais de relaxation à différentes températures ont été réalisés, en portant attention à ne pas dépasser la température de transition vitreuse (T_g) des échantillons partiellement polymérisés afin d'éviter la progression de la polymérisation pendant les essais. Les échantillons entièrement polymérisés

ont par exemple été testés à 9 températures, entre 30°C et 150°C inclusivement. Le principe de correspondance temps-température (Time Temperature Superposition Principle, TTSP) a été appliqué et des courbes maitresses ont été construites pour chacun des essais. Les facteurs de translation ont été déterminés et leurs dépendances à la température et au degré de polymérisation ont été modélisées par une relation d'Arrhenius, en prenant la température de transition vitreuse comme température de référence. Le modèle de DiBenedetto a été utilisé pour relier la T_g au degré de polymérisation. Un modèle spectral a été identifié pour relier les modules de relaxation aux temps de relaxation. De plus, un paramètre dépendant du degré de polymérisation a été ajouté devant les modules de rigidité pour tenir compte de la tendance, observée expérimentalement, des échantillons partiellement polymérisés à être plus rigides que les échantillons entièrement polymérisés à basses températures. Le modèle viscoélastique linéaire développé à partir de cette campagne expérimentale a, par la suite, été validé en comparant les prédictions du modèle par rapport à des résultats d'essais de fluage indépendants.

Les propriétés mécaniques des torons ont été évaluées avec le logiciel Abaqus. Un Volume Élémentaire Représentatif (VER), considérant un arrangement idéal hexagonal des fibres, a été construit pour les torons de chaine et de trame compte tenu que la fraction volumique de fibres diffèrent pour ces deux types de torons. Les propriétés élastiques du fabricant ont été utilisées pour les fibres et le modèle viscoélastique linéaire identifié précédemment en fonction de la température et du degré de polymérisation pour la résine pure a été implémenté dans une sous-routine. La matrice de rigidité des torons a été obtenue en appliquant des conditions périodiques et six chargements unitaires. Des essais de relaxation à différentes températures et degrés de polymérisation ont été simulés et les paramètres du modèle pour prédire les propriétés homogénéisées des torons ont été optimisés afin de reproduire ces simulations, en considérant un comportement isotrope transverse. La dépendance à la température a été identifiée comme étant la même que celle de la résine pure.

Les propriétés homogénéisées des torons de chaine et de trame, ainsi que les propriétés de la résine, ont été ensuite utilisées afin d'obtenir les propriétés homogénéisées orthotropes du composite, en fonction de la température et du degré de polymérisation. Pour cela, un VER voxélisé construit à partir du logiciel WiseTex et des conditions périodiques mixtes ont été utilisés. Comme pour les torons, des chargements unitaires ont été appliqués pour obtenir la matrice de rigidité du composite. La même dépendance à la température que la résine a, cette fois, été supposée d'emblée. C'est pourquoi des essais de relaxation à différents degrés de polymérisation seulement ont été simulés. Les paramètres du modèle pour prédire les propriétés homogénéisées du composite ont été optimisés afin de reproduire au mieux les simulations. Une dépendance orthotropique de la matrice de rigidité au degré de polymérisation a été

identifiée.

Finalement, le modèle homogénéisé a été validé en comparant les prédictions du modèle par rapport à des essais de fluage à 120°C et 140°C sur composite. Trois configurations ont été testées : les torons de chaine et les torons de trame dans le sens longitudinal des échantillons, et les torons de chaine orientés à 45° de la direction longitudinale. Des essais de fluage à hautes températures ont été réalisés pour les trois configurations. Les prédictions du modèle ont reproduit les résultats expérimentaux dans le domaine linéaire identifié au préalable. Des écarts sont encore observés mais plusieurs sources d'erreurs ont pu être identifiées : la variabilité des fractions volumiques de fibres, la convergence du maillage mesoscopique et l'utilisation de VER idéalisés. Des écarts de moins de 10% ont été observés pour les 3 configurations, hormis pour les échantillons avec les torons de trame dans le sens longitudinal à 140°C.

Dans le cadre de cette thèse, un modèle viscoélastique linéaire a été développé pour prédire le comportement de composites à renforts tissés 3D en fonction de la température et du degré de polymérisation. Il est thermodynamiquement admissible et basé sur des résultats expérimentaux obtenus sur la résine pure à différentes températures et degrés de polymérisation. La dépendance au degré de polymérisation a été étendue au composite de façon à s'adapter à différents comportements (isotropie, orthotropie, anisotropie).

ABSTRACT

Composites with three-dimensional (3D) reinforcements are increasingly used in the aerospace industry to overcome the 2D laminates limitations (low impact and delamination resistance). Structural parts are now made of composites reinforced with 3D fabrics due to their high specific mechanical properties and delamination resistance. However, residual stresses development is inherent to the manufacturing process and can induce geometrical distortions, leading to performance losses. Numerical tools have been developed to predict the residual stresses but coherent input material models are required to improve the tools accuracy.

The aim of this thesis was to develop and validate a thermodynamically consistent linearly viscoelastic model to predict the mechanical properties of a composite made of an epoxy resin and a 3D interlock woven carbon fibers fabric, as a function of temperature and degree of cure (DoC). The model was developed for the neat epoxy resin first. Then, the warp and weft tows' properties were computed by homogenization and the composite's properties were finally obtained through a second homogenization procedure considering the resin, warp and weft tows behaviors, as functions of temperature and degree of cure. The model has been implemented by another Ph.D student into a numerical tool to predict the residual stresses development during 3D woven composite parts manufacturing and succeeded to model the viscoelastic behavior that occurred during the post-curing.

First, a characterization campaign on the epoxy resin was carried out. Temperature- and degree of cure-dependent linearly viscoelastic behavior was assessed through multi-temperature tests using a three point bending fixture in a Dynamic Mechanical Analysis (DMA) apparatus. Multi-temperature relaxation tests were performed in the resin's linear domain strain range on fully and partially cured specimens, at temperatures ranging from 30 °C to their respective glass transition temperatures. The viscoelastic constitutive model development was based on the Thermodynamics of irreversible processes to ensure a thermodynamically admissible model. The Time Temperature Superposition Principle (TTSP) was applied and master curves were constructed for each performed test to compute the shift factors. An Arrhenius law was identified to relate temperature and degree of cure into the shift factors, with the glass transition temperature T_g as reference temperature. The degree of cure-dependent glass transition temperature was added through the DiBenedetto relationship. The relaxation stiffness tensors were associated with the relaxation times through a continuous spectra function. Moreover, a DoC-dependent factor was added in front of the rigidity tensors to account for the partially cured specimens tendency to be stiffer than fully cured samples

at low temperatures. The model parameter set was identified to fit the multi-temperature relaxation data for the fully and partially cured specimens. The model was then successfully validated by comparing its predictions for fully cured specimens temperature-dependent creep responses against experimental data.

The developed temperature- and degree of cure-dependent linearly viscoelastic model for the studied epoxy resin was implemented into a user subroutine `UMAT` in Abaqus to compute the composite's warp and weft tows homogenized mechanical properties. Hexagonal fibers packing Representative Volume Elements (RVEs) were designed for the warp and weft tows assuming different fiber volume fractions (V_f). Periodic Boundary Conditions (PBC) were set and relaxation tests were simulated at different temperatures and degrees of cure, applying unitary loads, to compute the full warp and weft tows stiffness tensors. The model parameter set was identified to fit the simulations results, assuming a transversely isotropic behavior. The tows temperature dependence was identical to that of the resin.

The identified homogenized mechanical properties of the resin and warp and weft tows, as a function of temperature and degree of cure, were finally used to compute the composite's homogenized mechanical properties. The full stiffness tensor for the composite was computed through relaxation tests performed on an idealized voxelized mesoscale RVE with mixed uniform boundary conditions (MUBC) at 30 °C. Based on the results obtained for the tows, the composite temperature-dependence was assumed to be the same as that of the resin. An orthotropic degree of cure-dependence was identified to fit the simulations results.

Finally, the homogenized temperature- and degree of cure-dependent linearly viscoelastic model was validated by comparing its predictions against composite experimental temperature-dependent creep data. Three configurations were studied: fully cured warp, weft and 45° oriented composite specimens were manufactured. High temperatures creep tests were performed for each configuration using an universal tensile machine. The model succeeded to predict the composite behavior in its linear domain. Some discrepancies were still observed between the experimental composite specimens creep responses and the numerical homogenized model predictions. Less than 10% of discrepancies were observed, except for the weft oriented specimens at 140 °C. These discrepancies are explained by the mesh coarseness, fiber volume fractions variability and the use of idealized RVEs.

In this thesis, a thermodynamically consistent linearly viscoelastic model was developed to predict the mechanical behavior of a composite reinforced with 3D woven fabric, as a function of temperature and DoC. The model is based on experimental data obtained for the resin at different temperatures and DoCs. The DoC-dependence was updated for the composite to fit any behavior (isotropy, orthotropy, anisotropy).

TABLE OF CONTENTS

LIST OF TABLES

LIST OF FIGURES

LIST OF SYMBOLS AND ABBREVIATIONS

Symbols

α	Degree of cure
α_{gel}	Gel point
β	Model parameter (continuous spectrum equation)
χ	Hidden (internal) variables
ε	Strain
η	Entropy density
λ	DiBenedetto material parameter
ω_k	Inverted relaxation times
$\log \tau_{\text{peak}}$	Peak position (continuous spectrum equation)
Ψ	Helmoltz's free energy
ρ	Mass density
σ	Stress
τ_k	Relaxation time
ξ	Reduced time $(= t')$
a	Model parameter (Arrhenius equation)
a_{T}	Shift factors
b	Model parameter (Arrhenius equation)
°C	Celsius degree
$\mathbf{C}^{(k)}$	Relaxation stiffness tensor
$\mathbf{C_0}$	Instantaneous relaxation tensor
$\mathbf{C}_\infty$	Fully relaxed stiffness tensor
$\mathbf{C}_m$	Warp/weft stiffness tensor
$\mathbf{C}_M$	Mesoscopic RVE stiffness tensor
$d(t_i)$	Experimental values (residue equation)
E	Elastic modulus
E_a	Activation energy
Err_m	Relative error (mesh convergence study for the microscopic RVE)
Err_M	Relative error (mesh convergence study for the mesoscopic RVE)
g	Heat flux
H	Peak height (continuous spectrum equation)
K_1	Model parameter ($p(\alpha)$)
K_2	Model parameter ($p(\alpha)$)

L_i	RVE edge lengths
l_{peak}	Peak width (continuous spectrum equation)
$m(t_i)$	Resin's model predictions (residue equation)
M_i	Material constants
$\text{N}_{elements}$	Number of elements
p_i	Nonlinearizing functions
$\mathbf{p}_m$	Model parameter for tows DoC-dependence
$\mathbf{p}_M$	Model parameter for mesoscopic RVE DoC-dependence
q	Homogenized model predictions (residue equation)
r	Residue
r_a	Residue for axial stiffness components
R	Universal gas constant
s	Simulated values (residue equation)
T	Temperature
T_{g}	Glass transition temperature
T_{g}^0	Glass transition temperature of uncured resin
T_{g}^∞	Glass transition temperature of fully cured resin
T_{ref}	Reference temperature
u_i	Displacements
V	Volume
V_f	Fiber volume fraction

Abbreviations

2D	Two-dimensional
3D	Three-dimensional
APBC	Approximate Periodic Boundary Conditions
C3D8	Fully integrated eight-node brick element
C3D8R	Eight-node brick element with reduced integration
CHILE	Cure Hardening Instantaneous Linear Elastic
CTE	Coefficient of Thermal Expansion
DIC	Digital Image Correlation
DGEBF	DiGlycidyl Ether of Bisphenol F
DMA	Dynamic Mechanical Analysis
DoC	Degree of Cure
DSC	Differential Scanning Calorimetry
FE	Finite Element

FFT	Fast-Fourier Transform
KUBC	Kinematic Uniform Boundary Conditions
MUBC	Mixed Uniform Boundary Conditions
NSERC	Natural Sciences and Engineering Research Council of Canada
ONERA	Office National d'Étude et Recherches Aérospatiales - The French Aerospace Lab
PBC	Periodic Boundary Conditions
Ph.D.	Philosophiæ Doctor
PMUBC	Periodic compatible Mixed uniform Boundary Conditions
PVT	Pressure Volume Temperature
$PVT\alpha$	Pressure Volume Temperature DoC
RTM	Resin Transfer Molding
RVE	Representative Volume Element
SCFM	Self-Consistent Field Micromechanics
SUBC	Stress Uniform Boundary Conditions
TTSP	Time-Temperature Superposition Principle
UD	Unidirectional

CHAPTER 1   INTRODUCTION

The aerospace industry is seeking to reduce CO_2 emissions by reducing weight. For this reason, composites are being increasingly used in structural aerospace applications due to their high specific mechanical properties (i.e., rigidity/mass), corrosion and fatigue resistance. When properly used, these materials could lead to significant mass savings if they were to replace their metallic counterparts.

Classical two-dimensional (2D) laminated composites exhibit high in-plane properties but present poor out-of-plane properties, triggering low impact and delamination resistance. Three-dimensional (3D) reinforcements, where fibers are strategically placed through the thickness, were developed over the last forty years to increase the composites out-of-plane properties. Recently, Safran group and General Electrics manufactured the LEAP engine where the fan blades and fan cases were made out of 3D interlock woven composites, as shown in Figure 1.1. 3D woven composites are generally manufactured by Resin Transfer Molding (RTM), which consists in injecting a liquid resin through a fibrous preform and then curing it according to a dedicated cycle. The resin's inherent chemical shrinkage during the curing process and the significant mismatch between the fibers and matrix Coefficients of Thermal Expansion (CTE), as well as friction interactions between the part and the mold, induce geometrical distortions and internal stresses in the molded parts. These distortions and internal stresses may have an impact on performance in gas turbine engines and must be controlled or predicted. Since the residual stresses evolve throughout the process' history and strongly depend on the composite mechanical properties, and hence in the resin's degree of cure (DoC) and thermal history, accurate input models for the multiscale temperature and DoC-dependent material behavior are required to predict the residual stresses development during manufacturing.

The NSERC-Safran Industrial Research Chair on novel 3D Composite Materials for the Aerospace Industry held at Polytechnique by Prof. Edu Ruiz aims to understand and develop manufacturing processes for structural composite parts. One line of research was focused on the residual stresses development during manufacturing and was decomposed into two sub-projects: *i*) the first sub-project, which is the subject of this thesis, dealt with the multiscale characterization and modeling of 3D interlock composites temperature and degree of cure-dependent mechanical properties; *ii*) the second sub-project dealt with the characterization and modeling of the residual stress development during 3D interlock composite parts manufacturing by RTM.

Figure 1.1 a) LEAP engine of Safran group (Julian, 2013-11-16) - b) Single fan blade made of 3D woven composites used in the LEAP engine (Drouin, 2017)

This work focused on modeling the multiscale mechanical behavior of an aerospace carbon/epoxy composite material made of 3D interlock woven fabrics. This study aimed at developing a multiscale temperature- and degree of cure-dependent linearly viscoelastic model. It addressed three objectives, namely the development of a temperature- and DoC-dependent viscoelastic model for the neat epoxy resin in collaboration with Onera (the French Aerospace Lab, France), the development of a multiscale homogenization model for a 3D woven carbon fabric reinforced composite material and the homogenization model validation against experimental data. The homogenized properties will then be implemented by another student into a commercially available finite element package and used to predict real parts distortions and process induced stresses.

This thesis is organized as follows. Chapter 2 presents a litterature survey on 3D fabrics, viscoelastic models and multiscale homogenization. Chapter 3 introduces the project objectives and the ensuing publication strategy. The two articles resulting from this work are presented in Chapters 4 and 5. Chapter 4 relates the developed temperature- and degree of cure-dependent linearly viscoelastic model for the studied epoxy resin and Chapter 5 presents the numerical multiscale homogenization methodology performed for a 3D interlock woven composite, in addition to the comparison between the predicted homogenized mechanical properties and experimental data. Chapter 6 discusses the articles and presents complementary studies performed during this project. The contributions of this thesis and its limitations are finally reported in Chapter 7.

CHAPTER 2   LITERATURE REVIEW

This chapter is a comprehensive literature review on the multiscale modeling of temperature- and DoC-dependent composites mechanical properties. Matrix behavior characterization techniques and modeling are described. Then, composites reinforced with 3D fabrics are introduced and their manufacturing and characterization methods are presented. Homogenization approaches to compute composites mechanical properties are finally described.

2.1   Notations

Scalar quantities are represented by light-faced letters (e.g., a), second-order tensors by bold Greek letters (e.g., $\boldsymbol{\sigma}$, $\boldsymbol{\varepsilon}$) and fourth order tensors by bold Roman letters (e.g., $\mathbf{C}$).

2.2   Thermoset resins

Thermoset polymers, like epoxy, undergo through an irreversible molecular cross-linking during the manufacturing. This process is quantified by the degree of cure, α. Initially liquid ($\alpha = 0$), the cross-linking of growing polymer chains advances until a three-dimensional molecular network is formed. An abrupt change in its viscosity occurs as an interconnected network is created and is referred to as the gel point (α_{gel}). The glass transition is the reversible change from a glassy to a rubbery state and the glass transition temperature, T_g, is the temperature around which the change occurs.

Thermosets are typically used in aerospace and automotive industries due to their high specific stiffness, fatigue life and corrosion resistance. Over the last decades, the mechanical properties of thermoset resins have been characterized and modeled. The main models found in the literature to describe the mechanical properties evolution as a function of degree of cure and temperature are presented herein.

2.2.1   Elastic mechanical properties modeling

Elastic models assume that there is an instantaneous linear relationship between stresses and strains, which can be temperature- and DoC-dependent. Johnston (1997) introduced the Cure Hardening Instantaneous Linear Elastic (CHILE) model to account for the temperature

softening and cure hardening occurring during manufacturing processes:

$$\boldsymbol{\sigma} = \mathbf{E}(T, \alpha) : \boldsymbol{\varepsilon} \tag{2.1}$$

where $\boldsymbol{\sigma}$ and $\boldsymbol{\varepsilon}$ are the stress and strain tensors, respectively, and $\mathbf{E}$ is the temperature- and degree of cure-dependent instantaneous elastic modulus. Several authors proposed different expressions whether the resin was before or after the gelation point (Bogetti et Gillespie, 1992; Ruiz et Trochu, 2005b; Khoun *et al.*, 2009; Msallem *et al.*, 2010). Indeed, the resin mechanical properties have been assumed negligible before the gel point as the resin is very compliant (Adolf et Chambers, 1997; Simon *et al.*, 2000; Khoun *et al.*, 2009; Khoun et Hubert, 2010; Msallem *et al.*, 2010). Khoun *et al.* (2009) proposed five discrete behaviors as a function of temperature and degree of cure, starting from the gel point, for an epoxy resin:

$$E = \begin{cases} 0 & \text{if } \alpha < \alpha_{gel} \\ E_1 & \text{if } T^* < T_1 \\ E_2 + (E_1 - E_2)\frac{T^* - T_2}{T_1 - T_2} & \text{if } T_1 < T^* < T_2 \\ E_3 + (E_2 - E_3)\frac{T^* - T_3}{T_2 - T_3} & \text{if } T_2 < T^* < T_3 \\ A_m \cdot \exp(-K_m \cdot T^*) & \text{if } T_3 < T^* < T_4 \\ E_4 & \text{if } T_4 < T^* \end{cases} \tag{2.2}$$

where $T^* = T - T_g(\alpha)$. T_g follows the DiBenedetto equation (DiBenedetto, 1987) which relates the glass transition temperature T_g to the degree of cure α as:

$$\frac{T_\mathrm{g} - T_\mathrm{g}^0}{T_\mathrm{g}^\infty - T_\mathrm{g}^0} = \frac{\lambda\alpha}{1 - (1 - \lambda)\alpha} \ . \tag{2.3}$$

T_g^0 and T_g^∞ are the uncured and the fully cured resin glass transition temperatures, respectively, and λ is a material parameter. An increase in the T_g is expected as the DoC increases. However, discontinuities of the derivative are noticeable at the transition temperatures complexifying the future numerical implementation. With more parameters to determine but a continuous function, Ruiz et Trochu (2005b) developed a model for a polyester resin which introduced an after-gel-point DoC:

$$E = E_{agp} + (E_c - E_{agp})[c \cdot \exp(d\hat{\alpha}) + e\hat{\alpha}]W(T_g) \tag{2.4}$$

where E_{agp} is the modulus after the gel point and E_c the fully cured modulus. Both depend on the temperature only. $\hat{\alpha}$ is the normalized degree of cure between the after-gel-point

degree and the one at the end of the reaction.

The main limitation of elastic models is that they do not account for stress relaxation and creep that occur at high temperatures. Recent works (Benavente *et al.*, 2017) showed that elastic models were not able to accurately predict the physical phenomena occurring during the curing, cooling and post-curing of 3D woven composite plates. The authors concluded that time-, temperature- and DoC-dependent input models were required to accurately predict distortions over the whole manufacturing process.

2.2.2 Viscoelastic mechanical properties modeling

Most thermoset resins exhibit a time-dependent response when subjected to a mechanical load. Creep and relaxation are viscoelastic behaviors that occur when a constant stress (creep) or strain (relaxation) is applied to the material and the strain or stress is measured, respectively, as shown in Figure 2.1. During creep, strain increases through time while a stress load is maintained constant and the material recovers to its original state when the stress is removed. During relaxation, a strain level is maintained and the stress decreases slowly towards a horizontal asymptote. For most polymers, viscoelastic behaviors are accentuated by temperature increase and low degree of cure.

Viscoelastic constitutive theories are developed to predict material behaviors under certain conditions. They have to respect the principles of thermodynamics. The first and second principles are met through the Clausium-Duhem inequality, namely :

$$\boldsymbol{\sigma} : \frac{\mathrm{d}\boldsymbol{\varepsilon}}{\mathrm{d}t} - \left(\frac{\mathrm{d}\Psi}{\mathrm{d}t} + \rho\eta\frac{\mathrm{d}T}{\mathrm{d}t}\right) - \frac{g \cdot \nabla T}{T} \geq 0 \tag{2.5}$$

where Ψ is Helmoltz's free energy, ρ the mass density, η the entropy density and g the heat flux. Two main approaches were elaborated from this inequality to develop constitutive theories, depending on the free energy time-dependence management: Rational thermodynamics (Caruthers *et al.*, 2004; Adolf et Chambers, 2007) and the Thermodynamics of irreversible processes (Biot, 1954; Schapery, 1964).

In Rational thermodynamics, the time derivative of the free energy is given by:

$$\frac{\mathrm{d}\Psi}{\mathrm{d}t} = \frac{\partial\Psi}{\partial\boldsymbol{\varepsilon}} : \frac{\mathrm{d}\boldsymbol{\varepsilon}}{\mathrm{d}t} + \frac{\partial\Psi}{\partial T}\frac{\mathrm{d}T}{\mathrm{d}t} + \frac{\partial\Psi}{\partial\nabla T} \cdot \frac{\mathrm{d}\nabla T}{\mathrm{d}t} \tag{2.6}$$
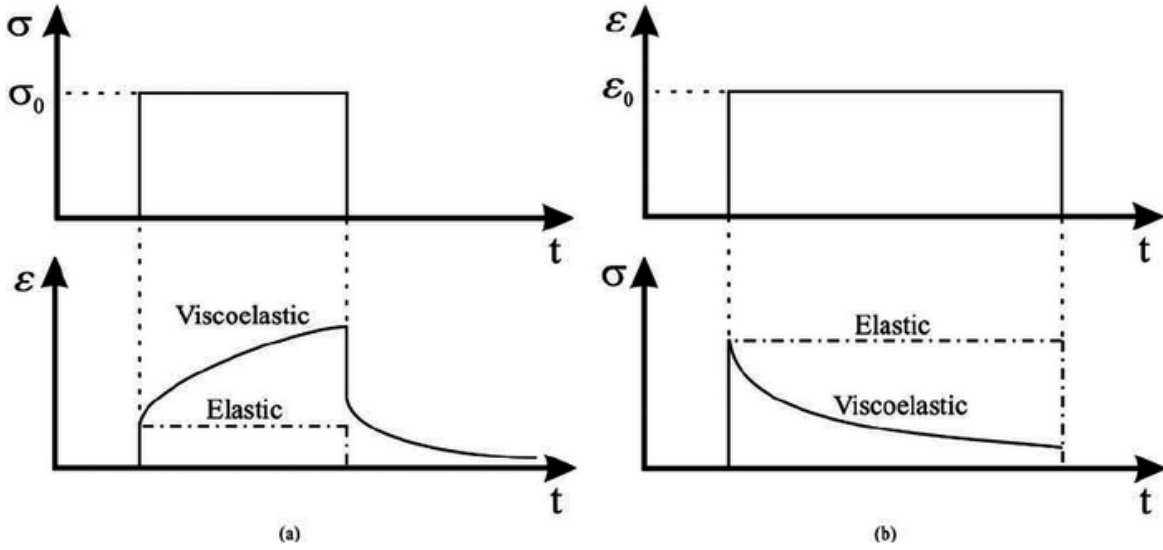
Figure 2.1 Viscoelastic behaviors : creep (a)) and relaxation (b)) (Misra *et al.*, 2008)

where $\boldsymbol{\varepsilon}$ is the strain tensor, T the temperature and ∇T the temperature gradient. Then,

$$\begin{cases} \frac{\partial \Psi}{\partial \boldsymbol{\varepsilon}} = \sigma \\ \frac{\partial \Psi}{\partial T} = -\rho \eta \\ \frac{\partial \Psi}{\partial \nabla T} = 0 \end{cases} \tag{2.7}$$

have then to be met to respect the Clausius-Duhem inequality. The free energy is expanded through a rigorous Taylor series expansion in Rational thermodynamics, leading to doubly convoluted integrals relating stresses and strains histories (Caruthers *et al.*, 2004).

In Thermodynamics of irreversible processes, the free energy is expressed with an additional term as

$$\frac{d\Psi}{dt} = \frac{\partial \Psi}{\partial \boldsymbol{\varepsilon}} : \frac{d\boldsymbol{\varepsilon}}{dt} + \frac{\partial \Psi}{\partial T} \frac{dT}{dt} + \frac{\partial \Psi}{\partial \nabla T} \cdot \frac{d\nabla T}{dt} + \frac{\partial \Psi}{\partial \boldsymbol{\chi}} : \frac{d\boldsymbol{\chi}}{dt} \tag{2.8}$$

where $\boldsymbol{\chi}$ represents the hidden variables characterizing the material's internal state and

$$\frac{\partial \boldsymbol{\Psi}}{\partial \boldsymbol{\chi}} = -\mathbf{B} : \frac{d\boldsymbol{\chi}}{dt} \tag{2.9}$$

has to be met as well as Equation 2.7. **B** is a semi-definite and symmetric tensor. A modified second order Taylor series expansion around a reference state is then used in the Thermodynamics of irreversible processes leading to a single convolution integral (Lévesque

et al., 2008).

Linearly viscoelastic constitutive theory development

Linearly viscoelastic constitutive theories in the Thermodynamics of irreversible processes were formalized by Biot (1954) through a thermodynamics framework and recalled by Lévesque *et al.* (2008). Assuming an adiabatic and isothermal load history, the Clausium-Duhem inequality (Equation 5.21) reduces to:

$$\left(\boldsymbol{\sigma} - \frac{\partial \Psi}{\partial \boldsymbol{\varepsilon}} \right) : \dot{\boldsymbol{\varepsilon}} - \frac{\partial \Psi}{\partial \boldsymbol{\chi}} : \dot{\boldsymbol{\chi}} \geq 0. \tag{2.10}$$

Equation 2.10 can be recast as:

$$\boldsymbol{f} : \dot{\boldsymbol{\varepsilon}} + \boldsymbol{b} : \dot{\boldsymbol{\chi}} \geq 0 \tag{2.11}$$

where $\boldsymbol{f}$ and $\boldsymbol{b}$ are called thermodynamic forces. Linear viscoelasticity assumes that these two forces are linearly related to the strain and hidden variables rate as :

$$\boldsymbol{f} = \mathbf{F} : \dot{\boldsymbol{\varepsilon}} \quad \text{and} \quad \boldsymbol{b} = \mathbf{B} : \dot{\boldsymbol{\chi}} \tag{2.12}$$

where $\mathbf{F}$ and $\mathbf{B}$ are positive semi-definite and symmetric tensors, which ensures the mathematical coherence of Equation 2.10. The Clausius-Duhem inequality has to be met for any load history. A reversible load history can thus be assumed, which implies constant internal variables. So, the constitutive theory is expressed as:

$$\boldsymbol{\sigma} = \left. \frac{\partial \boldsymbol{\Psi}}{\partial \boldsymbol{\varepsilon}} \right|_{\chi = \text{cte}}. \tag{2.13}$$

Linear viscoelasticity assumes also that the free energy Ψ is a Taylor expansion of the variables and is minimal at the initial state (i.e., when $\boldsymbol{\varepsilon} = \boldsymbol{\chi} = 0$), then:

$$\Psi(\boldsymbol{\varepsilon}, \boldsymbol{\chi}) = \frac{1}{2} \begin{bmatrix} \boldsymbol{\varepsilon} & \boldsymbol{\chi} \end{bmatrix} : \mathbf{L} : \begin{bmatrix} \boldsymbol{\varepsilon} \\ \boldsymbol{\chi} \end{bmatrix} \quad \text{with} \quad \mathbf{L} = \begin{bmatrix} \mathbf{L_1} & \mathbf{L_2} \\ (\mathbf{L_2})^T & \mathbf{L_3} \end{bmatrix}, \tag{2.14}$$

where

$$\mathbf{L}_1 = \frac{\partial \Psi}{\partial \varepsilon_i \partial \varepsilon_j} \ ; \ \mathbf{L}_2 = \frac{\partial \Psi}{\partial \varepsilon_i \partial \chi_r} \ ; \ \mathbf{L}_3 = \frac{\partial \Psi}{\partial \chi_r \partial \chi_s} \ . \tag{2.15}$$

$\mathbf{L_1}$ and $\mathbf{L_3}$ are positive definite. Thus, $\mathbf{L}$ is symmetric and positive definite as well. In a basis where $\mathbf{L_3}$ and $\mathbf{B}$ are diagonal, combining Equations 2.10, 2.12 and 2.14 leads to:

$$B_{rr}\dot{\chi}_r + L_{3rr}\chi_r + L_{2ir}\varepsilon_i = 0 \tag{2.16}$$

This relation is thus an uncoupled set of differential equations. Using the Laplace transform, the differential equations' solutions become:

$$\chi_r(t) = -\frac{L_{2ri}}{L_{3rr}}\int_0^t (1 - \exp[-\omega_r(t-\tau)])\frac{\mathrm{d}\varepsilon_i}{\mathrm{d}\tau}\mathrm{d}\tau \tag{2.17}$$

where $\omega_r = \frac{L_{3rr}}{B_{rr}}$. Combining Equations 2.13, 2.14 and 2.17 leads to the constitutive theory:

$$\boldsymbol{\sigma}(t) = \mathbf{C}_\infty : \boldsymbol{\varepsilon}(t) + \int_0^t \sum \mathbf{C^{(k)}} \exp[-\omega_k(t-\tau)] : \frac{\mathrm{d}\boldsymbol{\varepsilon}}{\mathrm{d}\tau}\mathrm{d}\tau \tag{2.18}$$

where $\mathbf{C^{(k)}}$ are positive semi definite and symmetric. $\mathbf{C}_\infty$ is the fully relaxed stiffness tensor and ω_k are the inverted relaxation times associated to the relaxation moduli $\mathbf{C^{(k)}}$. It should be noted that Equation 2.18 accounts for any class of material symmetry. In one dimension (1D), Equation 2.18 is typically referred to as the generalized Maxwell model.

Spectral formulations

Spectral formulations consist in associating variables with relaxation times, yielding using a spectrum of variables (Chaboche, 1997). Maire (1992) proposed a spectral formulation to predict unidirectional (UD) laminates behavior. The authors defined a continuous spectrum through a Gaussian distribution. Defining a continuous spectrum allows reducing the number of parameters to identify: instead of finding all variables, only the coefficients of the new relation have to be found. This methodology has been used by Vieille *et al.* (2016), who proposed a linear spectral viscoelastic model combined with a generalized Norton-type viscoplastic model to compute the properties of thermoplastic laminates at high temperature.

Extension to nonlinearly visoelastic constitutive theories

Nonlinearly viscoelastic models were developed to predict the nonlinear behavior of polymers. Maire (1992) introduced a nonlinear spectral formulation, which was widely recalled and adapted in composites damage models (Schieffer *et al.*, 2002; Marcin, 2010). Haj-Ali et Muliana (2004); Lévesque *et al.* (2008); Sawant et Muliana (2008) and Crochon (2014) proposed nonlinear viscoelastic models based on the integral formulation developed by Schapery

(1970). Schapery (1970) introduced nonlinearizing functions to develop nonlinear viscoelastic constitutive theories in a thermodynamics framework. The free energy expansion (Equation 2.14) was modified as:

$$\Psi(\boldsymbol{\varepsilon}, \boldsymbol{\chi}) = \Psi_0 + \frac{1}{2}p_4\boldsymbol{\varepsilon} : \mathbf{L}_1 : \boldsymbol{\varepsilon} + p_3\boldsymbol{\varepsilon} : \mathbf{L}_2 : \boldsymbol{\chi} + \frac{1}{2}p_2\boldsymbol{\chi} : \mathbf{L}_3 : \boldsymbol{\chi} \tag{2.19}$$

and

$$\frac{\partial \boldsymbol{\Psi}}{\partial \boldsymbol{\chi}} = -p_1\mathbf{B} : \frac{\mathrm{d}\boldsymbol{\chi}}{\mathrm{d}t}, \tag{2.20}$$

where p_1, p_2, p_3 and p_4 are positive scalar functions that can depend on state variables such as strain $\boldsymbol{\varepsilon}(t)$, temperature T, or degree of cure DoC. Equation 2.16 becomes:

$$p_1B_{rr}\dot{\chi}_r + p_2L_{3rr}\chi_r + p_3L_{2ir}\varepsilon_i = 0 \tag{2.21}$$

Using the reduced time introduced by Schapery (1964),

$$\xi(t) = \int_0^t \frac{p_2(\rho)}{p_1(\rho)}\mathrm{d}\rho, \tag{2.22}$$

the solution of Equation 2.21 yields

$$\boldsymbol{\sigma}(t) = p_4\mathbf{C}_\infty : \boldsymbol{\varepsilon}(t)$$
$$+ \left(\frac{\partial p_3}{\partial \boldsymbol{\varepsilon}} \otimes \boldsymbol{\varepsilon} + p_3\mathbf{I}\right) : \int_0^t \sum_{k=1}^K \mathbf{C}^{(k)} \exp\left(-\omega_k\left(\xi(t) - \xi(\tau)\right)\right) : \frac{\mathrm{d}}{\mathrm{d}\tau}\left[\frac{p_3}{p_2}\boldsymbol{\varepsilon}(\tau)\right]\mathrm{d}\tau. \tag{2.23}$$

Temperature dependence

Temperature dependence can be modeled through the Time-Temperature Superposition (TTS) principle (Ferry, 1980) that states that an increase in temperature in thermorheologically simple materials does not change but only accelerates the viscous effects. Sihn et Tsai (1999) detailed the principle through Figure 2.2 showing typical creep compliance (D_c) evolution as a function of time for different temperatures. Figure 2.2 a) shows that a master curve can be obtained by horizontally shifting the individual curves by a temperature-dependent shift factor a_T. The reduced time, $t' = \frac{t}{a_\mathrm{T}}$ also called ξ, is then defined. The shift factor, a_T, is typically set to 1 at a reference temperature T_0 and then scaled for increasing temperatures. Figure 2.2 b) shows a_T as a function of temperature.

The Williams-Landel-Ferry (WLF) equation was proposed many years ago to express the
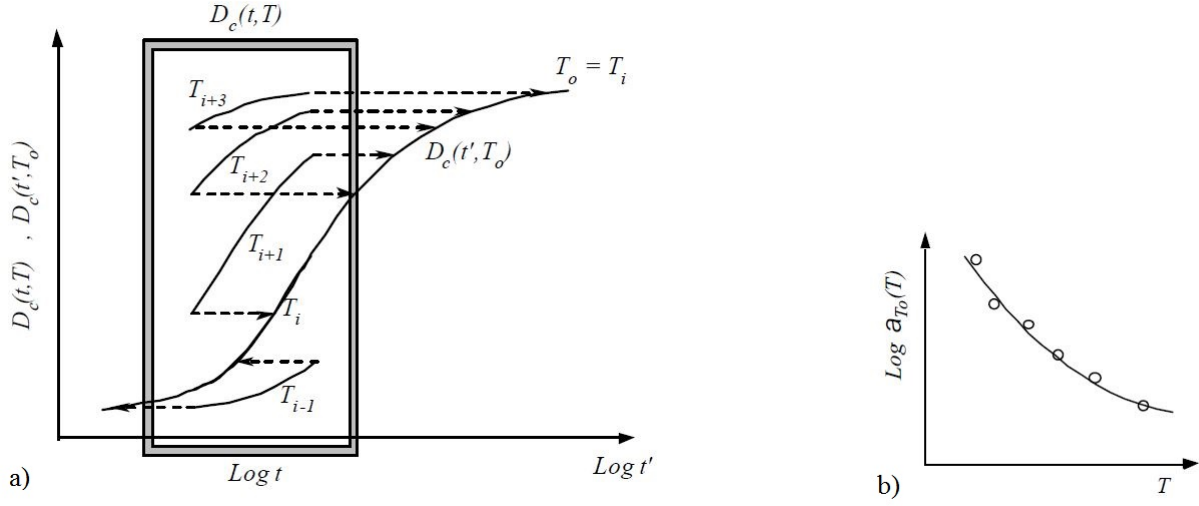
Figure 2.2 Time-temperature superposition principle - a) Master curve construction from creep compliance (D_c) evolution - b) Shift factors, a_T, as a function of temperature (Sihn et Tsai, 1999)

relationship between a_T and T (Williams *et al.*, 1955) as:

$$\log(a_T) = \frac{-M_1(T - T_{\text{ref}})}{M_2 + T - T_{\text{ref}}}, \tag{2.24}$$

where M_1 and M_2 are adjustable material constants. Other authors relied on Arrhenius equation (Sihn et Tsai, 1999; Hojjati *et al.*, 2004; Miyano *et al.*, 2007), expressed as:

$$\log(a_T) = \frac{E_a}{\ln(10)R} \left(\frac{1}{T} - \frac{1}{T_{\text{ref}}} \right), \tag{2.25}$$

where R is the universal gas constant (8.314 J/(Kmol)) and E_a is the activation energy (J/mol). Finally, Simon *et al.* (2000) used the Vogel equation that combines both the WLF and the Arrhenius models as:

$$\log(a_T) = \log \frac{\tau_i(T)}{\tau_i(T_{\text{ref}})} = \frac{M}{T - T_\infty} - \frac{M}{T_{\text{ref}} - T_\infty}, \tag{2.26}$$

where M is a material constant and T_∞ is expressed as a function of T_g ($T_\infty = T_g - M_2$) if the WLF equation applies or $T_\infty = 0$ if the Arrhenius relationship does.

Vertical shift factors have also been introduced for thermorheologically complex materials (e.g., Schapery (1974); Miyano *et al.* (2008); Crochon (2014)). As explained by Zobeiry (2006), horizontal shift factors could be insufficient to construct master curves for some materials, thus defined as thermorheologically complex (Schapery, 1974).

Degree of cure dependence

Thermoset matrix exhibit a stronger viscoelastic behavior at low DoC. Simon *et al.* (2000) took into account the DoC by introducing the glass transition temperature T_g in the shift factors and using the DiBenedetto relationship (DiBenedetto, 1987) (Equation 2.3) as:

$$\log a_{\mathrm{T},\alpha} = \log \frac{M}{T - T_\infty} - \frac{M}{T_g(\alpha) - T_\infty}. \tag{2.27}$$

Kim et White (1996) proposed an alternative relationship that reads:

$$\log a_\mathrm{T} = c_1(\alpha)T + c_2(\alpha), \tag{2.28}$$

where $c_1(\alpha)$ is the slope of the curve $\log a_\mathrm{T}$ as a function of the temperature and $c_2(\alpha)$ is the ordinate at origin. Their model has only been applied to materials after the gel point. O'Brien *et al.* (2001) used a rheometer to obtain data before the gel point and added a DoC-dependence in each term of their Prony series to describe an epoxy resin's shear relaxation modulus as:

$$G(t,\alpha) = G_\infty(\alpha) + \sum_{i=1}^{N} G_i(\alpha) \exp\left(-\frac{t}{\tau_i(\alpha)}\right), \tag{2.29}$$

where G_∞ is the equilibrium modulus. Ruiz et Trochu (2005b) proposed a relationship for linearly viscoelastic materials as:

$$C(\xi) = C_0 \exp[-M_1(\xi + M_4)^{M_2}](\xi + M_4)^{-M_3}, \tag{2.30}$$

where M_i are material elastic constants. The DoC-dependence was introduced through the parameters M_1 and M_3 by linear relations and through C_0 by a power function. Saseendran et al. distinguished the viscoelastic behavior of an epoxy resin below (Saseendran *et al.*, 2016) and above its glass transition temperature (Saseendran *et al.*, 2017b) and proposed to take the DoC-dependence through a cure shift function in both cases.

2.2.3 Viscoelastic constitutive theories numerical implementation strategies

Implementation of viscoelastic constitutive theories into Finite Element (FE) codes using integral formulation requires, in theory, storing the whole loading history, for all time steps. Two main strategies have been developed to circumvent this difficulty.

Taylor *et al.* (1970) developed a so-called recursive method for a linearly viscoelastic behavior. The technique consists in introducing a recursive expression to relate two time steps. They

assumed a linear variation of the load history and divided the integral into recursive parts. An exact analytical expression was then obtained. Similarly, Haj-Ali et Muliana (2004) used the recursive method for a nonlinear viscoelastic model. In this case, linear convergence rate was exhibited. Crochon *et al.* (2010) developed a recursive strategy with a quadratic convergence rate that accelerates calculation while preserving the same level of accuracy.

Others proposed to differentiate the integral formulation in first order differential equations instead. This strategy enables the use of well-known finite-difference methodologies (e.g., Euler, Crank-Nicholson, Runge-Kutta). Crochon *et al.* (2010) proposed a differential method based on the derivation of the integral formulation, valid for any material symmetry. The authors showed that the differential strategies are as effective as the recursive strategies for low order finite-difference schemes and become beneficial for fourth-order schemes like Runge-Kutta.

2.2.4 Poisson's ratio modeling

The Poisson's ratio is the ratio of transversal strain to axial strain during a tensile test where the force is applied. Most authors considered epoxy resins as isotropic with a constant Poisson's ratio of 0.35 over time and cure (Bogetti et Gillespie, 1992; Kim et White, 1996; O'Brien *et al.*, 2001). Others studied the cure and time dependences of the Poisson's ratio. O'Brien *et al.* (2007) developed a cure-dependent viscoelastic model for two epoxy resins Poisson's ratio through the glass transition temperature during creep tests. The shift factors used to construct the Poisson's ratio master curves were the same as those for the creep compliance master curves. Ersoy *et al.* (2010) assumed a Poisson's ratio evolution from 0.37 in the glassy state (manufacturer data) to 0.5 at the rubbery state (as nearly incompressible). More recently, based on experimental relaxation data, Saseendran *et al.* (2017a) proposed a degree of cure-dependent viscoelastic Poisson's ratio ranging from 0.32 to 0.44 for an epoxy resin. However, to the best of the author's knowledge, no proper comparison has been done in resins behavior models between the assumption of a constant Poisson's ratio and the use of a cure-, temperature- and/or time-dependent Poisson's ratio.

2.2.5 Mechanical properties characterization

Dedicated equipment and methodologies have been developed for measuring local composites constituents and their properties. Universal testing machines and Dynamic Mechanical Analyser (DMA) have been widely used in the literature to characterize the material viscoelastic behavior during creep and relaxation tests. In dynamic mechanical testing, the material's properties are obtained by a frequency or temperature sweep using a DMA. DMA testing

relies typically on smaller samples than classical creep / relaxation samples and provides results in a shorter time due to faster thermal equilibrium. However, accurate strain measurements in DMA is more challenging than on universal testing machines used for creep / relaxation tests.

Interconversions have been typically used for predicting the relaxation response of material parameters obtained under creep tests, or vice-versa. Algorithms like that of Luk-Cyr *et al.* (2013) have been developed for this task. Data obtained from frequency-sweep DMA tests have also been converted to the time domain when the obtained properties were to be used into a FE homogenization framework. For that reason, some authors chose to conduct directly relaxation tests in the time domain (Kim et White, 1996; Simon *et al.*, 2000; Ruiz *et al.*, 2004; Brauner *et al.*, 2017) using tension, three point bending, cantilever tests mostly on DMA instruments. Three point bending offers the advantage that the material response is not affected by the clamping boundaries and the specimen is free to expand (Hwang *et al.*, 1992).

Manufacturing and testing partially cured samples is challenging and time consuming. First, for low DoC, the polymer is quite compliant, which makes its handling in the mechanical testing equipment quite challenging. Epoxy samples are even brittle at room temperature at DoCs just above gelation. Moreover, partially cured samples tested above their T_g undergo a chemical reaction progression, thus affecting the readings (O'Brien *et al.*, 2001; Ruiz *et al.*, 2004; Zarrelli *et al.*, 2006). To overcome this difficulty, some authors combined several characterization instruments to simultaneously measure multiple properties during polymerization. Billotte *et al.* (2013) developed a device combining a DMA instrument and a novel heat flux cell. Isothermal dynamic mechanical tests were conducted on an epoxy resin during cure. DoC's evolution was simultaneously measured with mechanical properties, thermal expansion and chemical shrinkage. Peron *et al.* (2014) focused on the use of a pressurizable dilatometer which measures the evolution of pressure, volume and temperature during cure. The method is usually referred to as PVT measurement. Meng *et al.* (2009) also used this apparatus to measure the bulk modulus through pressure relaxation measurements. Peron *et al.* (2014) proposed further $PVT\alpha$ measurements to overcome the limitation of the evolution of properties during the full cure cycle. The same principle as that of Billotte *et al.* (2013) was put into practice in this $PVT\alpha$ instrument for an epoxy resin : temperature, volume change and DoC were simultaneously recorded for an applied pressure by using heat flux sensors. O'Brien *et al.* (2001) combined a parallel plate rheometer to analyze behavior prior to gel and a three-point bending setup to measure the post-gel mechanical properties of an epoxy resin.

2.3 Composites reinforced with 3D textile fabrics

3D textile composites are multiscale structured materials: tows are made of aligned fibers and matrix, and stitched/knitted/braided/woven tows form the fabric. The microscopic scale features the individual fibers and the matrix, withing the tows. The mesoscopic scale features the tows constituting the fibrous architecture and the surrounding matrix (Lomov *et al.*, 2007). One can define a unit cell, which is a fraction of the part that is repeatable in the three orthogonal directions, to construct the whole part, or a Representative Volume Element (RVE), which is a volume fraction of the part that behaves as the part. RVEs are usually used to compute effective properties.

2.3.1 3D textile fabrics

3D textile fabrics are multiscale structured materials with aligned fibers in the three directions (in plane and out of plane). The presence of fibers in the through-thickness direction increases the delamination and damage resistance when compared to traditional 2D laminates composites (Mouritz *et al.*, 1999). Moreover, 3D reinforcement architecture design can be optimized for each specific application, reducing material waste and weight.

A tow or yarn is made of thousand aligned fibers. Warp tows in a fabric are aligned along the longitudinal direction of the fabric roll, weft tows along the in-plane orthogonal direction and transversal or binding tows are placed through the thickness. 3D fabrics can be stitched, knitted, braided or woven (Long, 2005). Stitching consists in joining tows with out-of-plane tows to improve 2D fabrics delamination resistance (see Figure 2.3 a)). Braiding techniques were developed to improve the torque, shear and impact properties (Tan *et al.*, 1997) (see Figure 2.3 b)). Knitting consists in interlacing tows loops, thus improving out-of-plane properties but decreasing in-plane properties (see Figure 2.4). 3D woven fibrous architectures are then the most used 3D textile reinforcements due to their high production rate and numerous
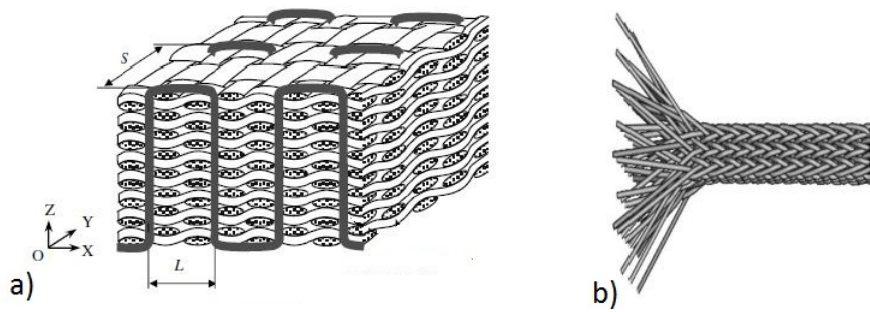
Figure 2.3 a) 3D stitched fabric (Nie *et al.*, 2008) - b) 3D braided fabric (Sun et Sun, 2004)
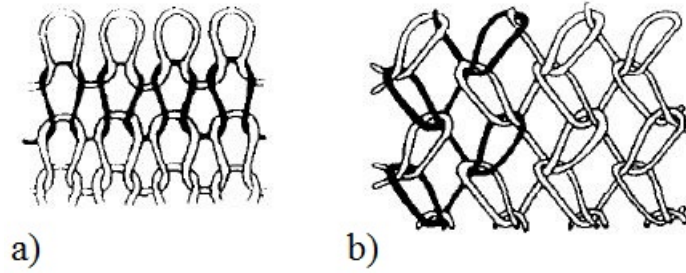
Figure 2.4 a) Warp knitted fabric - b) Weft knitted fabric (Tan *et al.*, 1997)

possibilities of patterns (Potluri *et al.*, 2012). They are increasingly used in aerospace industry in crankcases, fan blades or rocket engines. 3D woven architectures can be categorized in two groups: 3D woven fabrics manufactured with warp, weft and binding tows such as orthogonal woven fabrics shown in Figure 2.5 a) and those manufactured with warp and weft tows only, such as the angle interlock (cf. Figure 2.5 b)) or the layer-to-layer interlock (cf. Figure 2.5 c)). Interlock reinforcements consist in superimposed weft tows bound together in-plane and out-of-plane by warp tows.

2.3.2 3D woven composites manufacturing

3D woven composites are usually manufactured by Resin Transfer Molding (RTM) where the fabric is placed into a closed mold and the resin, pre-heated to reduce its viscosity, is injected under pressure at a particular temperature. The resin is cured when the fabric is fully impregnated. Friction interactions between the mold and the part and chemical shrinkage occur as the resin reticulates and evolves from a liquid to a rubbery and solid state. If the temperature varies, thermal expansion occurs during the curing. When fully cured, the solid resin gives shape to the part and the mold is cooled down. Frictions interactions take place
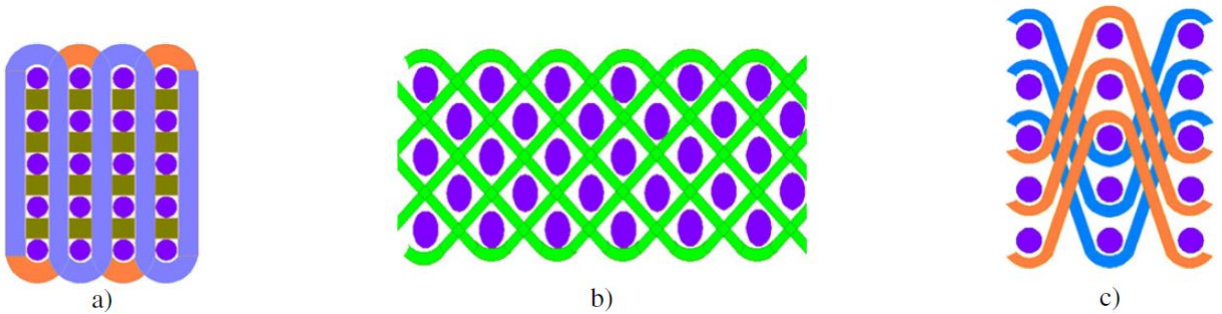
Figure 2.5 3D composite weaves - a)Orthogonal weave - b)Angle interlock weave - c)Layer-to-layer interlock weave (Potluri *et al.*, 2012)

until part's ejection and thermal effects until temperature stabilization. Figure 2.6 recalls the main steps of the RTM process. This process yields good surface finishes for both sides of the part and high fiber volume fractions are reached when compared to autoclave or infusion processes.

Interactions between the mold and the part, chemical shrinkage and mismatch in coefficients of thermal expansion (CTE) between fibers and matrix induce residual stresses that may distort the part (Palerosi et de Almeida, 2007).

2.4 Homogenization principles

Homogenization consists in predicting the behavior of an heterogeneous material from its constituents' properties. Textile composites overall properties are usually obtained through a two-step homogenization strategy for complex reinforcements. First, a micro homogenization computes the properties of impregnated tows from the constituents properties (resin and fiber tows), a tow being similar to a unidirectional composite. This is typically done through analytical models. Then, a second homogenization step is carried out to obtain the overall properties of impregnated tows in the resin phase. This is usually done through numerical methods. Figure 2.7 schematizes the multiscale homogenization principle. To limit the calculation time of the second step, the material's behavior is generally developed from the RVE. Tows are usually assumed to be transversely isotropic (Verpoest et Lomov, 2005; Kim *et al.*, 2008; Staub *et al.*, 2012; Xu *et al.*, 2015) and woven composite to be orthotropic (Kim *et al.*, 2008; Wu, 2009; Xu *et al.*, 2015).
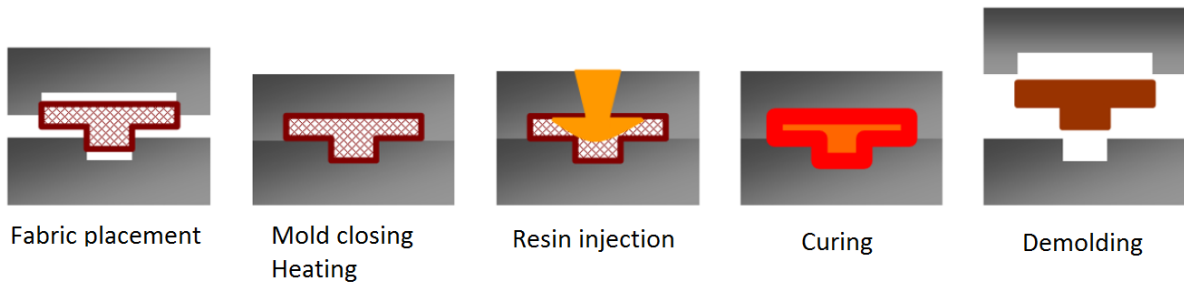
Figure 2.6 Main step of Resin Transfer Molding process (Renaud, 2016)
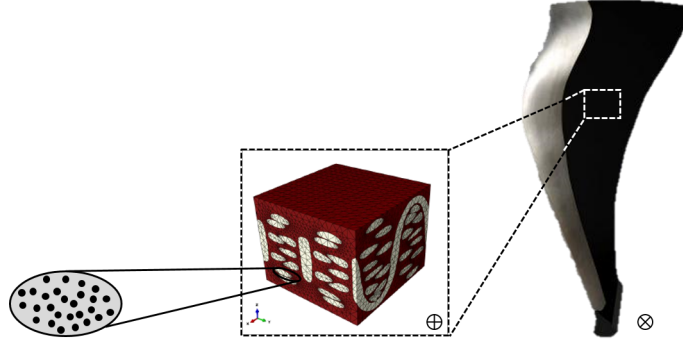
Figure 2.7 Multiscale homogenization: from the microscale (impregnated tows) to mesoscale modeling ($\oplus$ Bayraktar *et al.* (2012)), in order to obtain the overall composite behavior ($\otimes$ Drouin (2017))

2.4.1 Analytical methods

Elastic properties

Several formulations exist to compute composites linearly elastic overall properties. In early years, the so-called rule of mixtures and the classical laminate theory have been used to predict the composite's elastic behavior. However, the models met issues to compute accurately the overall properties of textile composites for high fiber volume fractions and significant weaving (El Mourid, 2014). Semi-empirical models were developed to improve the rule of mixtures. One of them is the Chamis model (Chamis, 1989) which preserves the rule of mixture relations for the longitudinal modulus E_{11} and the Poisson's ratio ν_{12} but computes the other properties as follows:

$$
\begin{cases}
E_{11} = V^f E_{11}^f + V^m E^m; \quad E_{22} = \dfrac{E^m}{1-\sqrt{V^f}\left(1-\frac{E^m}{E_{22}^f}\right)}; \quad \nu_{12} = V^f \nu_{12}^f + V^m \nu^m; \\[2em]
G_{12} = \dfrac{G^m}{1-\sqrt{V^f}\left(1-\frac{G^m}{G_{12}^f}\right)}; \quad G_{23} = \dfrac{G^m}{1-\sqrt{V^f}\left(1-\frac{G^m}{G_{23}^f}\right)}
\end{cases}
\tag{2.31}
$$

where E_{22}, G_{12} and G_{23} are the transversal and the two shear composite moduli, V^f is the fiber volume fraction and superscripts ^{f} and ^{m} represent the fiber and the matrix properties, respectively.

The inclusions methods are an alternative analytical homogenization technique which consider the fibers as inclusions in an homogeneous matrix. A common material model obeying CHILE formulation is the SCFM (Self-Consistent Field Micromechanics) model as presented by Bogetti et Gillespie (1992); Johnston *et al.* (2001); Svanberg *et al.* (2005); Ersoy *et al.*

(2010); Khoun *et al.* (2011). It is generally used to model unidirectional composites (as a tow is considered). This is an iterative scheme which assumes first that each inclusion is surrounded by an isotropic matrix and then isolated inside the homogeneous material. For low inclusions' volume fractions, the dilute solution is generally preferred. This method considers that ellipsoidal inclusions (fibers) exist inside an infinite phase (resin) and there are no interaction between phases. This dilute solution is efficient on materials with low inclusions' volume fractions. Finally, the Mori-Tanaka model takes into account interactions between inclusions making it more accurate for materials with higher inclusions' volume fraction than the dilute solution. Gommers *et al.* (1998) used the Mori-Tanaka model for modeling the linearly elastic behavior of textile composites. The authors considered tows as several ellipsoidal inclusions having the same orientation. The weaving and the tortuosity of the fibers was considered through orientation distribution functions.

Viscoelastic properties

The correspondence principle has been used to predict composites viscoelastic response through linearly elastic homogenization models. This principle consists in transforming viscoelastic laws in the Laplace-Carson domain and inputting the transformed properties into a linearly elastic homogenization scheme. An inverse transformation is then needed to obtain the coefficients in the time domain. The inversion usually requires numerical methods, like the collocation method of Schapery (1962) or the improved method of Lévesque *et al.* (2007). Lévesque *et al.* (2004) studied the nonlinear viscoelastic behavior of particle reinforced composites using the Mori-Tanaka scheme. Svanberg *et al.* (2005) used the SCFM relations to model the linearly viscoelastic woven composites behavior and added a factor to take into account the weaving influence on the properties. El Mourid *et al.* (2013) studied the linearly viscoelastic behavior of woven and braided composites and found that the Mori-Tanaka model delivered more accurate predictions than the self consistent scheme. However, both analytical techniques failed to accurately predict the responses for high volume fractions. Internal variables formulations were proposed by Ricaud et Masson (2009) to account for ageing behaviors and Blanc *et al.* (2011) to predict the linearly viscoelastic response of a three-phase media, using the correspondence principle.

Time-domain schemes have been introduced in order to avoid going into the Laplace domain. Lahellec et Suquet (2007) developed a time-domain scheme based on internal variables formulation to obtain the linearly viscoelastic composites response.

2.4.2   Numerical methods

Effective properties are typically obtained by applying boundary conditions to the RVE and then by solving the mechanical problem. The effective stiffness tensor C_{ijkl} must then meet the condition:

$$\bar{\sigma}_{ij} = C_{ijkl}\bar{\varepsilon}_{kl} \tag{2.32}$$

and effective stresses $\bar{\sigma}_{ij}$ and strains $\bar{\varepsilon}_{ij}$ are obtained from (Kanit *et al.*, 2003; Berger *et al.*, 2006; Rao *et al.*, 2008; Huang et Gong, 2018)

$$\begin{cases} \bar{\sigma}_{ij} = \frac{1}{V}\int_V \sigma_{ij}dV \\ \bar{\varepsilon}_{ij} = \frac{1}{V}\int_V \varepsilon_{ij}dV \end{cases} \tag{2.33}$$

where σ and ε are the stresses and strains, respectively, at each node or Gauss points and V is the RVE volume. The components of the stiffness tensor are computed applying six independent unit loads, detailed in Figure 2.8.

RVE modeling

The RVE geometry modeling is an important aspect in homogenization procedure as it influences the mechanical properties (Cox *et al.*, 1996). Commercially available software, like WiseTex (Verpoest et Lomov, 2005) or TexGen (Robitaille *et al.*, 1998; Sherburn, 2007), have been developed to automatically model fabric architectures, which are used further into FE software such as Abaqus. Micro and meso characteristics of the material are required, such as tows cross-sectional shapes, weave angle, tows density and architecture pattern. Tows tension, compression, bending and torsion are also modeled, as well as the fiber interactions. The tows centerlines are first constructed and their cross-sections are then extruded from the centerlines. Tows cross-sections were idealized as circular (Wang et Sun, 2001; Zhou

Unitary displacement	Applied strain	Components of the stiffness tensor
1	$[0.01; 0; 0; 0; 0; 0]^T$	$\bar{C}_{11}; \bar{C}_{21}; \bar{C}_{31}; \bar{C}_{41}; \bar{C}_{51}; \bar{C}_{61}$
2	$[0; 0.01; 0; 0; 0; 0]^T$	$\bar{C}_{12}; \bar{C}_{22}; \bar{C}_{32}; \bar{C}_{42}; \bar{C}_{52}; \bar{C}_{62}$
3	$[0; 0; 0.01; 0; 0; 0]^T$	$\bar{C}_{13}; \bar{C}_{23}; \bar{C}_{33}; \bar{C}_{43}; \bar{C}_{53}; \bar{C}_{63}$
4	$[0; 0; 0; 0.02; 0; 0]^T$	$\bar{C}_{14}; \bar{C}_{24}; \bar{C}_{34}; \bar{C}_{44}; \bar{C}_{54}; \bar{C}_{64}$
5	$[0; 0; 0; 0; 0.02; 0]^T$	$\bar{C}_{15}; \bar{C}_{25}; \bar{C}_{35}; \bar{C}_{45}; \bar{C}_{55}; \bar{C}_{65}$
6	$[0; 0; 0; 0; 0; 0.02]^T$	$\bar{C}_{16}; \bar{C}_{26}; \bar{C}_{36}; \bar{C}_{46}; \bar{C}_{56}; \bar{C}_{66}$

Figure 2.8 Six independent unit loads to compute the stiffness tensor (El Mourid, 2014)

et al., 2004) or lenticular (Lapeyronnie *et al.*, 2011), among others presented in Figure 2.9. Some authors considered constant cross-section through the architecture (Wang et Sun, 2001; Couégnat, 2008), while others took into consideration the variability of the tows cross-section that occurs due to the weaving pattern or compaction (Lomov *et al.*, 2001; Zhou *et al.*, 2004; Verpoest et Lomov, 2005). Weaving and density remain challenging, especially for high fiber volume fraction V_f, as interpenetration often occur during the RVE construction. Techniques have been developed to limit this shortcoming, like manually inserting spaces between tows (Grail, 2013). Voxel-like meshes were also computed to prevent the interpenetration issue (Kim et Swan, 2003). The RVE is meshed by cubic brick elements and properties are assigned to each element depending on its position. The accuracy of the architecture pattern and fiber volume fractions depends on the elements size. Other authors focused on the tows modeling themselves to prevent such issue (Wang et Sun, 2001; Zhou *et al.*, 2004; Durville, 2010) by managing the contact between fibers. Durville (2009) generated "macro-fibers" based on multifilament yarn mechanics (Wang *et al.*, 2010) to simulate the weaving process. No assumption on the cross-section is required and the macro-fibers rearrange themselves automatically according to the architecture pattern. Figure 2.10 shows a fabric geometry construction using the method proposed by Durville (2009). Otherwise, fibers packings were idealized by rectangular or hexagonal array (Ansar *et al.*, 2011), presented in Figure 2.11. Square (Berger *et al.*, 2006), rectangular (Choi et Sankar, 2006; Kari *et al.*, 2008; Xu *et al.*, 2012; Pathan *et al.*, 2017a), and hexagonal (Guinovart-Díaz *et al.*, 2001) RVEs are usually used to compute the properties of tows for rectangular or hexagonal fiber packings, as shown in Figure 2.12.

Computed tomography of molded composite samples were performed to obtain real composites mesoscopic architectures (Stig et Hallström, 2013). This method is a non destructive test consisting in scanning the specimen to detect the effective path of each tow in the fibrous structure. Micro-tomography and microscopy were also used to visualize the tows microscopic characteristics (fiber volume fraction, fibers arrangement) (Stig et Hallström, 2012). Figure 2.13 shows a tomographic scan of a composite material and microscopic transversal cross-section of a yarn. The main drawback of using tomography is that the data exploitation and interpretation are time-consuming and the equipment is expensive (Sisodia *et al.*, 2016).
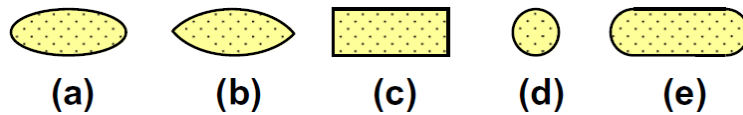
Figure 2.9 Tows cross-sectional shapes: (a) Ellipsoidal (b) Lenticular (c) Rectangular (d) Circular (e) Racetrack (Ansar *et al.*, 2011)
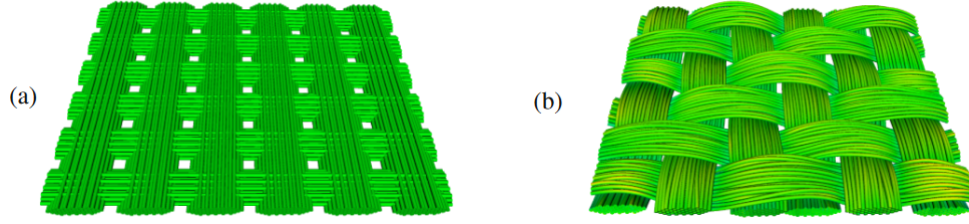
Figure 2.10 Fabric geometry construction based on multifilament yarn mechanics. a) Initial configuration before weaving - b) Configuration after weaving for plain weave (Durville, 2009)
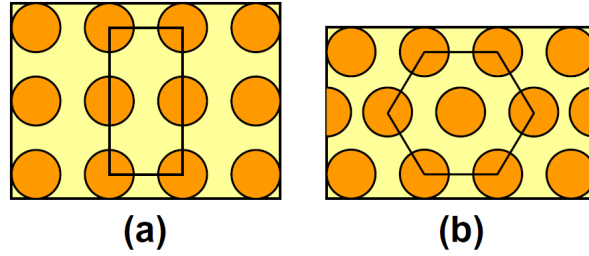
Figure 2.11 Idealized fiber packings. (a) Rectangular array - (b) Hexagonal array (Ansar *et al.*, 2011)

Moreover, reconstruction algorithms are as important as data acquisition (Charron, 2017) and can be challenging due to low contrast between the constituents or noise.

Boundary conditions

The RVEs have been typically modeled with FE technique with boundary conditions as mechanical or thermal loads. Kinematic Uniform Boundary conditions (KUBC), Stress Uniform Boundary Conditions (SUBC), Mixed Uniform Boundary Conditions (MUBC) and Periodic Boundary Conditions (PBC) are the most widely applied conditions (Van der Sluis *et al.*,

Figure 2.12 RVE for rectangular and hexagonal fibers arrangement. a) Square RVE for rectangular fibers packing- b) Rectangular and hexagonal RVE for hexagonal fibers packing

Figure 2.13 a) Microscopic transversal cross-section of a yarn (Lapeyronnie *et al.*, 2011)- b) Tomographic scan of a composite material (Madra *et al.*, 2017)

2000; Kanit *et al.*, 2003; Berger *et al.*, 2006; Barello et Lévesque, 2008; Rao *et al.*, 2008; Wang *et al.*, 2017; Huang et Gong, 2018). KUBC consists in applying a displacement u at points x belonging to the boundary ∂V, SUBC imposing a traction vector at points x and MUBC both (Kanit *et al.*, 2003; Pahr et Zysset, 2008):

$$\begin{cases} \text{KUBC:} & u(x) = Ex, \quad \forall x \in \partial V \\ \text{SUBC:} & t(x) = Sn, \quad \forall x \in \partial V \\ \text{MUBC:} & (t(x) - Sn) \cdot (u(x) - Ex) = 0, \quad \forall x \in \partial V \end{cases} \tag{2.34}$$

where E and S are constant tensors. Periodic boundary conditions are usually applied on periodic microstructures and are imposed to pairs of nodes that are on opposite parallel surfaces denoted as k^+ and k^- (Pahr et Zysset, 2008):

$$\text{PBC: } u(x)^{k^+} - u(x)^{k^+} = E\Delta x^k \quad \forall x \in \partial V^k, \tag{2.35}$$

where Δx^k is a constant distance vector between corresponding surfaces.

Bornert *et al.* (2001a) and Kanit *et al.* (2003) studied the different boundary conditions and concluded that PBC yield converged effective properties for smaller RVEs than KUBC and SUBC. Figure 2.14 shows the convergence studies on shear and bulk moduli for different RVE sizes. Hazanov et Huet (1994) showed that results applying KUBC and SUBC are the upper and lower bounds, respectively, compared to the results with MUBC.

Applying PBC is well-known to lead to the most accurate results (Bornert *et al.*, 2001a; Kanit *et al.*, 2003; Ghossein et Lévesque, 2014). However, a periodic mesh is necessary and this task can be challenging for non periodic microstructures and with the discretization of the RVE. To overcome this issue, specific set of MUBC that leads to the same results as
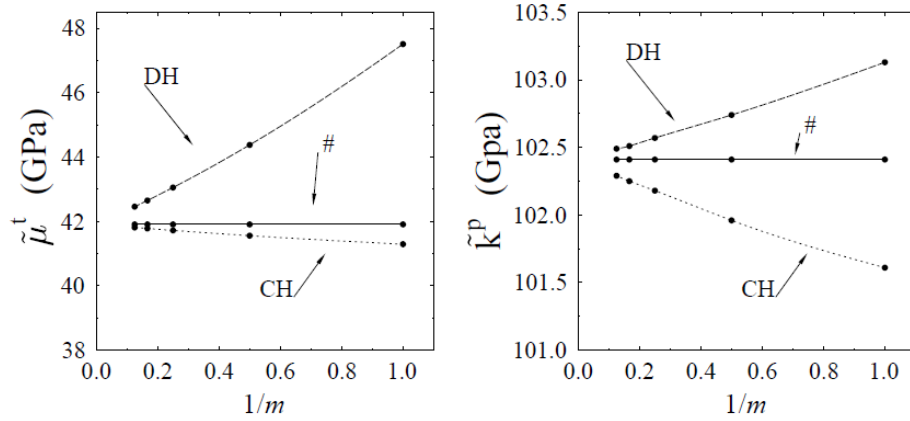
Figure 2.14 Shear $\tilde{\mu}^t$ and bulk $\tilde{k}^p$ moduli as a function of the RVE size $1/m$, with KUBC ("DH"), SUBC ("CH") and PBC ("#") (Bornert *et al.*, 2001a)

the use of PBC was proposed by Pahr et Zysset (2008) for orthotropic materials. Figure 2.15 details the corresponding Periodic compatible Mixed Uniform Boundary Conditions (PMUBC). Schneider *et al.* (2017) also studied PBC on fully periodic RVE and concluded that the meticulous work behind that was not worth the results accuracy. The authors proposed instead to apply Approximate Periodic Boundary Conditions (APBC) via surface-to-surface constraints (cf. Figure 2.16). Their method is easily applicable in commercial FE software and showed similar results as those obtained by applying PBC. Nguyen *et al.* (2012) proposed also a method to apply PBC on non-periodic mesh but their method requires high programming skills.

Homogenization for elastic materials

Numerical homogenization approaches to predict elastic behavior are widely present in the literature. Among others who worked on composites reinforced with 3D fabrics, Rao *et al.* (2008) studied the effect of different 3D architectures on composites' elastic mechanical properties. Lapeyronnie *et al.* (2011) used a numerical homogenization method to predict the elastic properties of 3D angle-interlock composites. 3D orthogonal woven composites elastic moduli were computed by Green *et al.* (2014) for different RVEs to analyse the effect of using idealized RVEs. The authors concluded that computations based on idealized RVEs overestimate the elastic properties. Huang et Gong (2018) studied the voids impact on 3D woven composites' elastic mechanical behavior through multiscale FE models and showed that the voids in tows impact on the elastic properties more than the voids in the resin phase.

	East	West	North	South	Top	Bottom
Tensile 1	$u_1 = {}^0\varepsilon_{11}\frac{l_1}{2}$ $t_2 = t_3 = 0$	$u_1 = -{}^0\varepsilon_{11}\frac{l_1}{2}$ $t_2 = t_3 = 0$	$u_2 = 0$ $t_1 = t_3 = 0$	$u_2 = 0$ $t_1 = t_3 = 0$	$u_3 = 0$ $t_1 = t_2 = 0$	$u_3 = 0$ $t_1 = t_2 = 0$
Tensile 2	$u_1 = 0$ $t_2 = t_3 = 0$	$u_1 = 0$ $t_2 = t_3 = 0$	$u_2 = {}^0\varepsilon_{22}\frac{l_2}{2}$ $t_1 = t_3 = 0$	$u_2 = -{}^0\varepsilon_{22}\frac{l_2}{2}$ $t_1 = t_3 = 0$	$u_3 = 0$ $t_1 = t_2 = 0$	$u_3 = 0$ $t_1 = t_2 = 0$
Tensile 3	$u_1 = 0$ $t_2 = t_3 = 0$	$u_1 = 0$ $t_2 = t_3 = 0$	$u_2 = 0$ $t_1 = t_3 = 0$	$u_2 = 0$ $t_1 = t_3 = 0$	$u_3 = {}^0\varepsilon_{33}\frac{l_3}{2}$ $t_1 = t_2 = 0$	$u_3 = -{}^0\varepsilon_{33}\frac{l_3}{2}$ $t_1 = t_2 = 0$
Shear 12	$u_2 = {}^0\varepsilon_{21}\frac{l_1}{2}$ $u_3 = 0, t_1 = 0$	$u_2 = -{}^0\varepsilon_{21}\frac{l_1}{2}$ $u_3 = 0, t_1 = 0$	$u_1 = {}^0\varepsilon_{12}\frac{l_2}{2}$ $u_3 = 0, t_2 = 0$	$u_1 = -{}^0\varepsilon_{12}\frac{l_2}{2}$ $u_3 = 0, t_2 = 0$	$u_3 = 0$ $t_1 = t_2 = 0$	$u_3 = 0$ $t_1 = t_2 = 0$
Shear 13	$u_3 = {}^0\varepsilon_{31}\frac{l_1}{2}$ $u_2 = 0, t_1 = 0$	$u_3 = -{}^0\varepsilon_{31}\frac{l_1}{2}$ $u_2 = 0, t_1 = 0$	$u_2 = 0$ $t_1 = t_3 = 0$	$u_2 = 0$ $t_1 = t_3 = 0$	$u_1 = {}^0\varepsilon_{13}\frac{l_3}{2}$ $u_2 = 0, t_3 = 0$	$u_1 = -{}^0\varepsilon_{13}\frac{l_3}{2}$ $u_2 = 0, t_3 = 0$
Shear 23	$u_1 = 0$ $t_2 = t_3 = 0$	$u_1 = 0$ $t_2 = t_3 = 0$	$u_3 = {}^0\varepsilon_{32}\frac{l_2}{2}$ $u_1 = 0, t_2 = 0$	$u_3 = -{}^0\varepsilon_{32}\frac{l_2}{2}$ $u_1 = 0, t_2 = 0$	$u_2 = {}^0\varepsilon_{23}\frac{l_3}{2}$ $u_1 = 0, t_3 = 0$	$u_2 = -{}^0\varepsilon_{23}\frac{l_3}{2}$ $u_1 = 0, t_3 = 0$

Figure 2.15 Periodicity compatible mixed uniform boundary conditions (PMUBC) set to apply on a RVE. ${}^0\varepsilon$ is a constant tensor, l_i are the volume element edges lengths, u_i denote displacements and t_i forces.(Pahr et Zysset, 2008)
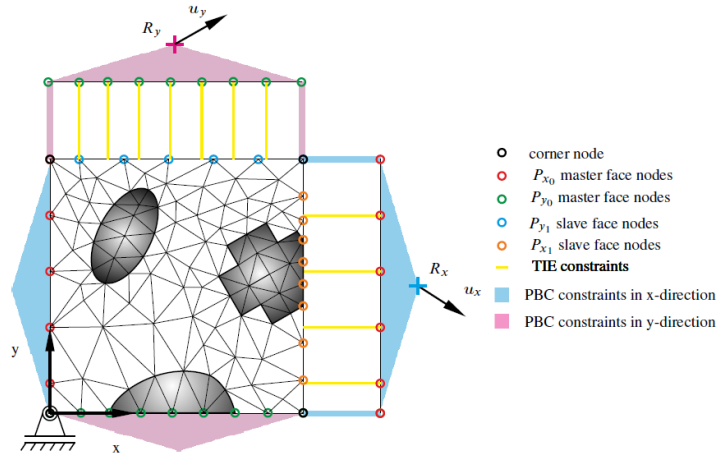
Figure 2.16 Sketch of Approximate Periodic Boundary Conditions (APBC)(Schneider *et al.*, 2017)

Homogenization for viscoelastic materials

Numerical homogenization is a very vast field, but very few authors dealt with the homogenization of viscoelastic 3D woven composites. Authors dealt mostly with spherical particles reinforced composites (Lévesque *et al.*, 2004; Fisher et Brinson, 2001; Muliana et Kim, 2007; Zhang et Li, 2009; Tran *et al.*, 2011). Fisher et Brinson (2001) considered viscoelastic inclusions embedded into a viscoelastic matrix and viscoelastic interphases between them. Viscoelastic composites are otherwise usually modeled as linearly elastic inclusions embedded into viscoelastic matrix (Lévesque *et al.*, 2004; Muliana et Kim, 2007). Viscoelastic behavior for short-fibers composites was also dealt in literature (Staub *et al.*, 2012; Gusev, 2017), as well as unidirectional composites (Zobeiry *et al.*, 2016; Pathan *et al.*, 2017b). Viscoelastic properties of braided composites was studied by El Mourid *et al.* (2013), who compared analytical and numerical homogenization techniques. Muliana et Haj-Ali (2008) proposed and experimentally validated a multiscale framework to analyse the thermo-viscoelastic behavior of multi-layered composites.

Few authors worked on the homogenization of temperature-dependent viscoelastic models (Muliana et Haj-Ali, 2008; Sawant et Muliana, 2008; Cai et Sun, 2014; Zobeiry *et al.*, 2016). Cai et Sun (2014) studied 3D braided composites' thermoviscoelastic properties and used the same temperature-dependence for the composites as that of the resin. Some authors dealt also with experimental tests to validate their predictions (Haj-Ali et Muliana, 2004; Muliana et Haj-Ali, 2008; Sawant et Muliana, 2008; Xu *et al.*, 2015). Creep and relaxation experimental data were usually compared to model predictions (Muliana et Haj-Ali, 2008; Sawant et Muliana, 2008).

An extensive literature review was done by Dixit et Mali (2013) on the modeling of woven composites mechanical properties but only elastic and/or 2D woven composites are discussed. In regard of this section, temperature-dependent viscoelastic FE homogenization approach for 3D interlock woven composite materials are non-existent in the literature yet, to the best of the author's knowledge.

2.5 Composites characterization techniques

The characterization methods presented in Subsection 2.2.5 were also used for composite samples. White et Hahn (1990) manufactured partially cured composite specimens by interrupting the molding cycle, cooling down the samples and testing them in tension. A DSC (Differential Scanning Calorimetry) instrument was used to characterize each specimens' DoC and relate it to the composite's mechanical properties. Others characterized shear or storage

moduli of partially cured samples with a DMA instrument (Kim et Daniel, 2002; Ersoy *et al.*, 2010). Melo et Radford (2003) and Ropers *et al.* (2016) based their viscoelastic model on DMA tests for transversely isotropic laminae and, unidirectional and woven thermoplastic composites, respectively. Ruiz *et al.* (2004) performed DMA tests for two composites, a non crimp glass fabric and a continuous strand mat with polyester resin. The flexural modulus of both materials were measured at different V_f and DoCs (from 45% to fully cured). Yanjun *et al.* (2006); Lomov *et al.* (2008); Lapeyronnie *et al.* (2011) et Charmetant *et al.* (2012) performed tension tests on warp and weft oriented 3D interlock woven composite specimens to get elastic properties. Three point bending tests were also performed by Lapeyronnie *et al.* (2011) and Nie *et al.* (2008) on 3D interlock woven composites and 3D stitched composites, respectively. Vieille *et al.* (2016) performed isothermal creep/recovery and multirelaxation tests on woven laminates.

Strain gauges have been glued to the specimens to measure strain evolution during mechanical testing (Yanjun *et al.*, 2006; Nie *et al.*, 2008). The choice of gauges is crucial and challenging. It must be compatible with the specimens material and the range of strain experienced during the experiment. The installation of gauges is moreover a meticulous work. Extensometers have been installed onto the samples for higher strain levels (Nie *et al.*, 2008; Lapeyronnie *et al.*, 2011). Digital image correlation (DIC) is being more an more used due to the main advantage of not interacting with the tested material (Vieille *et al.*, 2016).

However, testing materials at different temperatures remains challenging whatever the means of measurement. Thermal expansion of the measurements device interferes with the material response (for gauges and extensometers) and the setup for DIC gets tricky due to the oven and noise can be detected because of convection.

CHAPTER 3   OBJECTIVES AND RATIONALE

The main objective of this research project was to predict the response of a composite material made of a DiGlycidyl Ether of Bisphenol F (DGEBF) epoxy resin and a 3D interlock woven fabric, with a fiber volume fraction of 51%, for different DoC and temperatures. A four-layer 3D interlock woven reinforcement made of Hexcel IM10 carbon fibers with an unbalanced warp/weft ratio was chosen. Due to confidentiality, no other specific detail, nor the commercial name of the material, can be disclosed.

In that regard, the literature survey revealed the following:

- Polymer resins' mechanical behavior is modeled using multiple approaches leading to different levels of accuracy. Materials which show a strong time dependence need a more complex viscoelastic model than a linearly elastic model. Temperature- and/or DoC- dependencies have been accounted for in viscoelastic models. While measuring temperature-dependent viscoelastic properties is well established, measuring DoC-dependence remains a challenge. Indeed, manufacturing partially cured samples at a precise DoC and manipulating them is tricky. Moreover, testing above their T_g could be problematic due to the low stiffness of the material at such temperatures and because the polymerization would continue. That is why models found in the literature are not systematically validated against experiments along the whole temperature and DoC ranges, but are extrapolated. Moreover, no unique modeling technique has been endorsed by the scientific community. This implies that each scientific group chooses its own modeling recipe that best fits the tested material.

- To obtain the whole composite materials' properties, two homogenization steps are required : at micro- (fiber/resin interaction) and macro-levels (fabric ply/resin interaction). FE modeling is preferred for complex structures. Furthermore, authors showed that numerical methods allow more accurate predictions than analytical solutions, especially for high volume fractions composites. The use of the Laplace domain to apply elastic relationships and inverse transformation to obtain the properties back in the time domain is the most popular strategy instead of analytical viscoelastic homogenization strategy.

  Modeling the 3D interlock woven fabric is also a challenge due to its complex architecture and fibers interactions. Tows are usually assumed transversely isotropic whose packing is idealized by an hexagonal arrangement, and woven composite orthotropic.

Periodic boundary conditions lead to the most accurate results but alternatives were developed for non periodic microstructures. To the best of the author's knowledge, temperature-dependent viscoelastic behavior of 3D interlock woven composites have not been reported.

Recursive and differential techniques are proposed in the literature to implement viscoelastic constitutive theories into FE codes. Differential methods allow using higher order FE schemes, which could considerably decrease the execution time of vast numerical campaigns.

- Several experimental techniques were recalled to measure elastic and viscoelastic properties for polymer and composite specimens. However, limited information exists on partially cured samples and temperature-dependence experiments remain challenging in regard to the set-up and measurements accuracy. Moreover, scientific studies of 3D woven composites' viscoelastic behavior as a function of temperature is non existent in the literature.

Based on the findings in the literature, three specific objectives have been defined in order to reach the main objective, namely:

1. **Develop a temperature- and DoC-dependent viscoelastic model for the epoxy resin**

   A characterization campaign was conducted to obtain the epoxy resin's viscoelastic behavior. Mechanical properties were determined as a function of the temperature and degree of cure by relaxation tests. A thermodynamically consistent viscoelastic model was then developed to predict the resin's behavior as a function of temperature and degree of cure.

   The article entitled "Viscoelastic Behavior Of An Epoxy Resin During Cure Below The Glass Transition Temperature: Characterization And Modeling" has been accepted for publication in the Journal of Composite Materials. This journal publishes original research on advanced composite materials. The author of this thesis wrote 85% of the paper. The preliminary modeling part was developed during a 6 months stay at Onera in France. Professors M. Lévesques and E. Ruiz, and Dr. L. Marcin and Dr. M. Hirsekorn contributed to the redaction.

2. **Perform the numerical multi-scale homogenization of a 3D interlock woven carbon fabric reinforced composite**

   The composite's effective properties was computed through a two-step FE homogenization procedure where the yarns were first homogenized and used in the mesoscopic

model where they were considered as homogeneous. The fibers' properties and FE mesh of the 3D interlock woven fabric was provided by the industrial partner while the resin's mechanical model developed at objective 1 was used. Hexagonal packing was designed in Abaqus and PBC were applied to compute the warp and weft yarns properties, while MUBC were applied on the mesoscale voxelized RVE.

3. **Validate the homogenized model with experimental data**

   The homogenized model was experimentally validated by studying the behavior of molded composite specimens. The parts viscoelastic behavior was analyzed from creep tests as a function of the temperature using an universal tension machine.

   The article entitled "Temperature- And Cure-Dependent Linearly Viscoelastic Model For 3D Interlock Woven Composites: Numerical Multiscale Homogenization Approach And Experimental Validation" was submitted for publication to the International Journal of Solids and Structures. This journal publishes original research on mechanics of solids and structures. This second paper reached the two last objectives, dealing with the multiscale homogenization and the experimental validation on composite specimens. The author of this thesis wrote 85% of the paper. Professors M. Lévesques and E. Ruiz and Dr. L. Marcin contributed to the redaction.

CHAPTER 4   ARTICLE 1 : VISCOELASTIC BEHAVIOR OF AN EPOXY RESIN DURING CURE BELOW THE GLASS TRANSITION TEMPERATURE: CHARACTERIZATION AND MODELING

A. Courtois, M. Hirsekorn, M. Benavente, A. Jaillon, L. Marcin, E. Ruiz, M. Lévesque (2018).

4.1 Abstract

This paper presents a viscoelastic temperature- and degree-of-cure-dependent, constitutive model for an epoxy resin. Multi-temperature relaxation tests on fully and partially cured rectangular epoxy specimens were conducted in a DMA (Dynamic Mechanical Analysis) apparatus with a three-point bending clamp. Master curves were constructed from the relaxation test results based on the Time Temperature Superposition (TTS) hypothesis. The influence of the degree of cure was included through the cure dependent glass transition temperature which was used as reference temperature for the shift factors. The model parameters were optimized by minimization of the differences between the model predictions and the experimental data. The model predictions were successfully validated against an independent creep-like strain history over which the temperature varied.

4.2 Introduction

Process-induced residual stresses arise in the liquid molding of composites due to the differential volumetric changes of the constituents and the mechanical interactions between the mold and the parts. Volume changes stem from the chemical shrinkage of the resin as well as from the coefficients of thermal expansion (CTE) mismatch between the resin and fibers. Process-induced residual stresses result in unwanted distortions in composite parts. Numerical tools have been developed to predict residual stresses in composite parts made by different manufacturing processes such as autoclave (Bogetti et Gillespie, 1992) or RTM (Resin Transfer Molding) (Ruiz et Trochu, 2006). The main challenges lie in the fact that the resin evolves from a liquid to a viscoelastic solid state through a complex time and temperature dependent process.

Resin's gel point (α_{gel}) corresponds to a given degree of cure for which an infinite polymer network is created. This is typically associated with a steep buildup of the resin's mechanical

properties. A number of authors have therefore developed degree-of-cure-dependent constitutive models for polymer resins. Most authors assumed that before the gel point the resin is so compliant that residual stresses are relaxed immediately (Adolf et Chambers, 1997; Simon *et al.*, 2000; Khoun *et al.*, 2009; Msallem *et al.*, 2010; Khoun et Hubert, 2010). Bogetti et Gillespie (1992) proposed a modified degree of cure rule of mixtures where an epoxy's Young's modulus for a given degree of cure (α) was related to those of the fully cured and uncured conditions. Ruiz et Trochu (2005b) proposed a model where the resin's stiffness depended on an after-gel-point degree of cure (α_{agp}) after which the resin exhibited a significant rigidity.

The gel point of epoxy resins lies typically at degrees of cure between 0.6 and 0.7. Khoun et Hubert (2007) found an α_{gel} of 0.7 for an epoxy resin by taking the degree of cure when the storage and loss moduli are equal. Zarrelli *et al.* (2002) obtained an α_{gel} between 0.64 and 0.66 through isothermal rheometric experiments. Simon *et al.* (2000) and Prasatya *et al.* (2001) determined the gel point of an epoxy resin theoretically to $\alpha_{\text{gel}} = 0.63$.

The polymer network formation is in fact a continuous process transforming the resin from a viscous liquid before the gel point to a viscoelastic solid with increasing viscosity. Therefore, stress relaxation remains important as long as the resin is not fully polymerized and at temperatures close to the glass transition temperature T_{g}. T_{g} defines the temperature around which the polymer evolves from a brittle glassy state to a viscous rubbery state. The resin's mechanical properties drop around that temperature and stress relaxation becomes much more important. Since T_{g} is usually exceeded during manufacturing processes, relaxation will be important during curing and at the first stages of the cooling process. The residual stresses are only really set towards the end of the cooling phase.

Several authors therefore proposed temperature and cure dependent viscoelastic models for epoxy resins. For example, Kim et White (1996) proposed to model the α-dependency through time shift factors a_{T}. Simon *et al.* (2000) used the cure dependent glass transition temperature T_{g} as the reference temperature and relied on the DiBenedetto equation (DiBenedetto, 1987) to relate T_{g} with the degree of cure. O'Brien *et al.* (2001) introduced the α-dependency through the stiffness of a linearly viscoelastic model. These models were all developed for epoxy resins and each reproduced experimental data reasonably well. However, very few authors reported and discussed the inherent variability of such measurements and validated their model on independent data sets. The respect of thermodynamics principles was also rarely accounted for. Caruthers *et al.* (2004) and Adolf et Chambers (2007) developed a thermodynamically consistent viscoelastic approach for thermosets during cure based on rational thermodynamics, which led to doubly convoluted integrals linking strains and stresses histories. Lévesque *et al.* (2008) summarized the viscoelastic constitutive theories

developed by Biot (1954) and Schapery (1964) based on the thermodynamics of irreversible processes, which led to single convoluted integrals. Single convoluted integrals can be cast under a differential form (Crochon *et al.*, 2010), which delivers highly efficient implementation algorithms, which is a clear advantage of such formulations.

While some authors already attempted to merge viscoelasticity, temperature, and cure dependencies (Simon *et al.*, 2000; O'Brien *et al.*, 2001; Ruiz et Trochu, 2005b; Zarrelli *et al.*, 2010; Mahnken, 2013), the experimental data sets used to obtain the constitutive theories parameters were usually limited to fully cured specimens or to very few partially cured specimens. O'Brien *et al.* (2001) measured viscoelastic properties on the entire range of degrees of cure through creep tests and needed conversion calculations to obtain relaxation modulus. Adolf *et al.* (2004) obtained the parameters through an extensive experimental campaign on four different polymers in the glass transition region.

The purpose of this work was to characterize, predict and validate the relaxation behavior of a viscoelastic epoxy resin by accounting for its temperature and degree of cure dependencies, based on a thermodynamically rigorous approach, easily implementable. The paper is organized as follows: the material studied, the specimen manufacturing, the thermo-mechanical testing procedures and the experimental results are first presented. The mechanical model is then detailed with the parameter optimization and the model predictions are finally validated on different load cases.

4.3 Material and experimental procedures

A commercial DGEBF epoxy resin (DiGlycidyl Ether of Bisphenol F), already prepared, was studied in this work. Specifications can't be disclosed for confidentiality reasons.

4.3.1 Samples manufacturing

Dedicated silicon molds, shown in Figure 4.1, were used to produce 150 rectangular fully and partially cured specimens of nominal dimensions of 50mm × 10mm × 2.7mm. The fully cured specimens were held at 180°C during 180 minutes under a pressure of 0.55MPa to limit porosities. Partially cured specimens were produced by interrupting the cure cycle after 81, 68, 59, 54, 49 and 45 min at 165°C. The samples were then cooled down by convection outside the mold at room temperature, which was too low for the studied resin to continue curing. For each mold and curing cycle, one sample was broken into smaller parts that served as Differential Scanning Calorimetry (DSC) samples. The degrees of cure and the glass transition temperatures were then measured by DSC on two to four samples for each

mold and curing cycle, after the cooling. The modulated mode was used and a ramp of 2°C/min from 25°C to 290°C was applied. These measurements showed that the six partially cured specimen batches were polymerized at 94%, 90%, 86%, 80%, 74% and 66%, at ±0.2%, respectively, with a maximum contrast of 0.5% for each silicon mold. The lowest degree of cure is therefore close to the values for the gel point found by Simon *et al.* (2000), Prasatya *et al.* (2001), Zarrelli *et al.* (2002) and Khoun et Hubert (2007). In fact, the specimens at 66% cure were very fragile and demolding and polishing was particularly challenging, but mechanical testing was still possible. The gel point of the studied resin lies therefore not much below 66%, and the tested specimens cover well the whole range of cure from the gel point to full polymerization.
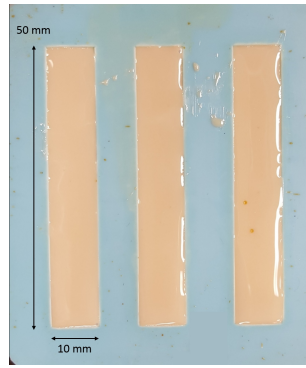
Figure 4.1 Silicon mold used to manufacture epoxy samples for DMA tests

4.3.2   Thermo-mechanical testing in the linearly viscoelastic domain

RTM manufactured composite parts are submitted to small deformations during the process. For this reason, this work focused on strains in the order of 0.1%. Relaxation tests were performed for strain levels of $\varepsilon_1 = 0.05\%$ and $\varepsilon_2 = 2\varepsilon_1 = 0.1\%$ at 30°C and 150°C with a three-point bending clamp in a TA Instruments Q800 DMA apparatus on fully cured specimens to ascertain the linearly viscoelastic domain in this strain range. Figure 4.2 shows the experimental set-up. The stress evolution is then plotted in Figures 4.3 and 4.4 at 30°C and 150°C, respectively, for samples tested at the two different applied strains. The stress responses to a strain of 0.05%, multiplied by 2, were added and compared to the stress evolution resulting from an applied strain of 0.1%. Figures 4.3 and 4.4 show that the stress response due to a strain of 0.1% and twice the stress response to an applied strain of 0.05% are very close to each other, for both temperatures. It can therefore be assumed that the studied resin remains in the linearly viscoelastic range for strain and temperatures below 0.1% and 150°C (below the glass transition temperature), respectively, for a fully cured state. It was

assumed that this observation held for the other degrees of cure (for strain below 0.1% and temperatures below their glass transition temperature).
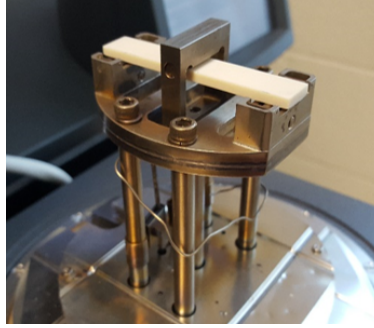
Figure 4.2 Experimental set-up: three-point bending clamp installed on a DMA Q800
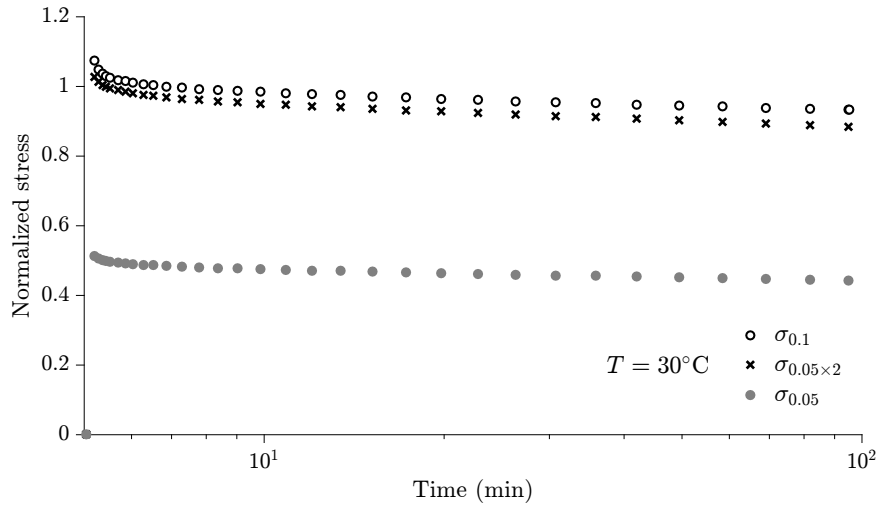
Figure 4.3 Determination of the linearly viscoelastic range during a relaxation experiment at 30°C. $\sigma_{0.1}$ represents the stress evolution for a strain level of 0.1%. $\sigma_{0.05}$ represents the stress evolution for a strain level of 0.05%. $\sigma_{0.05\times2}$ corresponds to $2 \times \sigma_{0.05}$. The figure suggests that the material obeys a linearly viscoelastic constitutive theory for a strain range of 0.1% and a temperature of 30°C

Multi-temperature relaxation tests were then carried out on fully and partially cured specimens. Starting from 30°C, the specimens were bent to 0.1% of strain and held at constant strain for 90 minutes to measure relaxation behavior. After each relaxation phase, the bending load was removed and 10 minutes of recovery was allowed. The temperature was then increased by 15°C over a heating phase of 10 minutes. The temperature was held constant at the new level for an additional 5 minutes prior to initiating the following relaxation phase in order to ensure the apparatus and sample thermal equilibrium. This procedure was repeated up to a temperature below the glass transition temperature (150°C for the fully cured
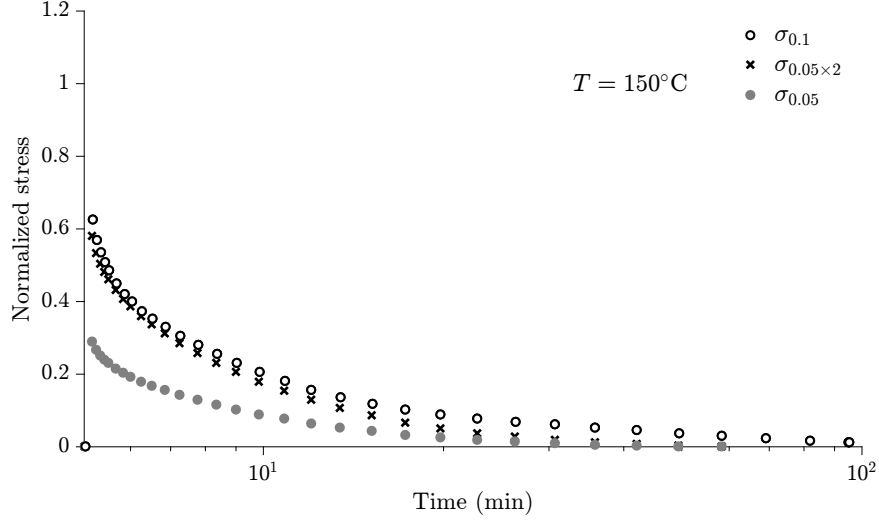
Figure 4.4 Determination of the linearly viscoelastic range during a relaxation experiment at 150°C. $\sigma_{0.1}$ represents the stress evolution for a strain level of 0.1%. $\sigma_{0.05}$ represents the stress evolution for a strain level of 0.05%. $\sigma_{0.05 \times 2}$ corresponds to $2 \times \sigma_{0.05}$. The figure suggests that the material obeys a linearly viscoelastic constitutive theory for a strain range of 0.1% and a temperature of 150°C

specimens for example), because above T_g the resin becomes too compliant to obtain reliable experimental data with the used DMA apparatus. The limitation to temperatures below T_g also ensures that the degree of cure does not evolve significantly during the experiments. The entire load history was considered further in the parameters determination through the model implementation, as detailed in Section 4.4.4.

4.3.3 Experimental results

Figure 4.5 shows the relaxation curves for fully and partially cured samples at the tested temperatures. Note that stress values were normalized by the actual stress measured at the beginning of relaxation, on fully cured samples and at 30°C, for confidentiality. For clarity, only the average stress evolution is plotted for each degree of cure. The full experimental data of all specimens are shown in section *Comparison between model predictions and experimental relaxation data.* The figure shows that the relaxation rate increased as the temperature raised and the cure decreased. Moreover, there is at first sight no clear hierarchy between the responses at different degrees of cure at 30°C and 45°C. Since the temperature was limited to T_g, the lower was the degree of cure, the lower was the last tested temperature.
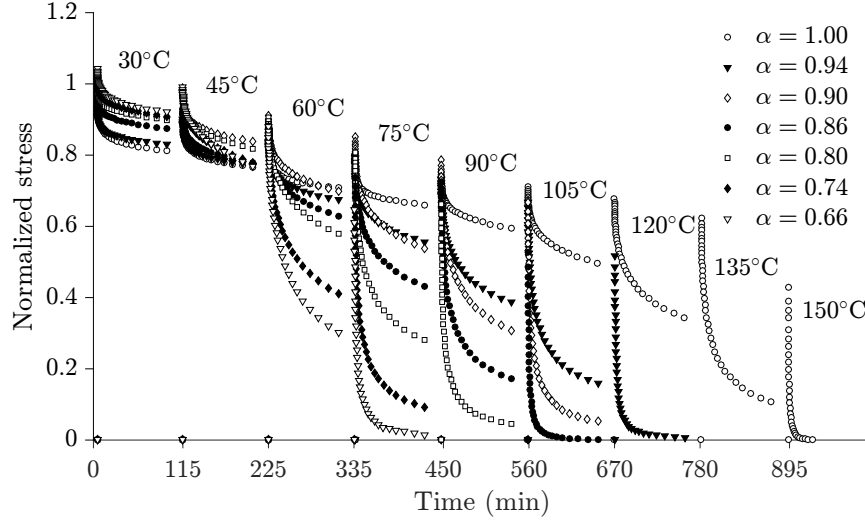
Figure 4.5 Normalized average stress relaxation curves for partially and fully cured samples, from α=0.66 to α=1.0

4.4 Mechanical model

This section recalls the thermodynamics of irreversible processes framework developed by Biot (1954) and Schapery (1964), and summarized by Lévesque *et al.* (2008), used to write viscoelastic constitutive theories. Then, a special form of the viscoelastic model is proposed to account for the influence of the degree of cure. The model equations are defined based on the experimental observations presented previously. The final parts of this section comprise a description of the numerical implementation of the model, the parameter optimization procedure and the comparison between model results and experimental data.

4.4.1 Background

Combining the first and second laws of thermodynamics leads to the well-known Clausius-Duhem inequality (Schapery, 1970):

$$\boldsymbol{\sigma} : \frac{\mathrm{d}\boldsymbol{\varepsilon}}{\mathrm{d}t} - \left(\frac{\mathrm{d}\Psi}{\mathrm{d}t} + \rho\eta\frac{\mathrm{d}T}{\mathrm{d}t} \right) - \frac{q \cdot \nabla T}{T} \geq 0 \tag{4.1}$$

where Ψ is Helmoltz's free energy, ρ the mass density, η the entropy density and q the heat flux. Constitutive theories must meet this inequality to meet the first two principles of thermodynamics. Two main paths have been undertaken to derive constitutive theories from Equation 4.1 (Crochon, 2014): rational thermodynamics (Caruthers *et al.*, 2004; Adolf et Chambers, 2007) and thermodynamics of irreversible processes (Biot, 1954; Schapery, 1964). The rational thermodynamics approach relies on a rigorous Taylor series expansion of the free

energy which leads to doubly convoluted integrals linking stresses and strains histories. In the thermodynamics of irreversible processes, the free energy is expanded through a modified second order Taylor series around a reference state (Lévesque *et al.*, 2008) and leads to a single convolution integral relating the stresses and strains histories, but for which the parameters can depend on stress, temperature, etc. In addition, this approach expresses the free energy as a function of state and hidden variables. When assuming an adiabatic and isothermal loading history, Equation (4.1) becomes

$$\left(\sigma_i - \frac{\partial \Psi}{\partial \varepsilon_i}\right)\dot{\varepsilon}_i - \frac{\partial \Psi}{\partial \chi_r}\dot{\chi}_r = f_i\dot{\varepsilon}_i + b_r\dot{\chi}_r \geq 0 \tag{4.2}$$

where χ_r are internal variables and f_i and b_r are the thermodynamics forces that can be expressed as a function of state and internal variables ($f_i = F_{ij}\dot{\varepsilon}_j$, $b_r = B_{rs}\dot{\chi}_s$, with F and B constant matrices) in case of linear viscoelasticity. The free energy can then be expanded (Crochon, 2014):

$$\Psi(\boldsymbol{\varepsilon}, \boldsymbol{\chi}) = \Psi_0 + \frac{1}{2}\boldsymbol{\varepsilon} : \mathbf{L}_1 : \boldsymbol{\varepsilon} + \boldsymbol{\varepsilon} : \mathbf{L}_2 : \boldsymbol{\chi} + \frac{1}{2}\boldsymbol{\chi} : \mathbf{L}_3 : \boldsymbol{\chi} \tag{4.3}$$

where Ψ_0 is the free energy in the equilibrium state,

$$\mathbf{L}_1 = \frac{\partial \Psi}{\partial \varepsilon_i \partial \varepsilon_j} \; ; \mathbf{L}_2 = \frac{\partial \Psi}{\partial \varepsilon_i \partial \chi_r} \; ; \mathbf{L}_3 = \frac{\partial \Psi}{\partial \chi_r \partial \chi_s} \text{ and } \mathbf{L} = \begin{bmatrix} \mathbf{L}_1 & \mathbf{L}_2 \\ (\mathbf{L}_2)^{\mathrm{T}} & \mathbf{L}_3 \end{bmatrix}. \tag{4.4}$$

$\mathbf{L}$ is symmetric and positive semi-definite. As shown by Lévesque *et al.* (2008), linearly viscoelastic models can then be written in the general form

$$\boldsymbol{\sigma}(t) = \mathbf{L}_1 : \boldsymbol{\varepsilon}(t) + \mathbf{L}_2 : \boldsymbol{\chi}(t) \tag{4.5a}$$

$$\mathbf{B} : \dot{\boldsymbol{\chi}} + \mathbf{L}_3 : \boldsymbol{\chi} + (\mathbf{L}_2)^{\mathrm{T}} : \boldsymbol{\varepsilon} = \mathbf{0} \tag{4.5b}$$

where

$$\frac{\partial \boldsymbol{\Psi}}{\partial \boldsymbol{\chi}} = -\mathbf{B} : \dot{\boldsymbol{\chi}} \tag{4.6}$$

The solution of Equation (4.5) yields (Luk-Cyr *et al.*, 2013):

$$\sigma_i(t) = \left(L_{1_{ij}} - \frac{L_{2_{ir}}L_{2_{jr}}}{L_{3_{rr}}}\right)\varepsilon_j + \frac{L_{2_{ir}}L_{2_{jr}}}{L_{3_{rr}}}\int_0^t \exp\left[-\frac{L_{3_{rr}}}{B_{rr}}(t-\tau)\right]\frac{\mathrm{d}\varepsilon_j}{\mathrm{d}\tau}\mathrm{d}\tau, \tag{4.7}$$

which can be cast under the form

$$\boldsymbol{\sigma}(t) = \mathbf{C}_\infty : \boldsymbol{\varepsilon}(t) + \int_0^t \sum_{k=1}^N \mathbf{C_k} \exp\left(-\frac{t-\tau}{\tau_k}\right) : \frac{\mathrm{d}\boldsymbol{\varepsilon}}{\mathrm{d}\tau}\mathrm{d}\tau \tag{4.8}$$

$\mathbf{C}_\infty$ is the fully relaxed tensor and the $\mathbf{C_k}$ are the relaxation tensors associated with the relaxation times τ_k. The $\mathbf{C_k}$ are positive semi-definite and symmetric. In one dimension (1D), Equation (4.8) is typically referred to as the generalized Maxwell model.

Following the same thermodynamically rigorous approach, Schapery (1969) has introduced nonlinear constitutive theories through scalar nonlinearizing functions. The expansion of the free energy becomes

$$\Psi(\boldsymbol{\varepsilon}, \boldsymbol{\chi}) = \Psi_0 + \frac{1}{2}\boldsymbol{\varepsilon} : \mathbf{L}_1 : \boldsymbol{\varepsilon} + p_3 \boldsymbol{\varepsilon} : \mathbf{L}_2 : \boldsymbol{\chi} + \frac{1}{2}p_2 \boldsymbol{\chi} : \mathbf{L}_3 : \boldsymbol{\chi} \tag{4.9}$$

and

$$\frac{\partial \boldsymbol{\Psi}}{\partial \boldsymbol{\chi}} = -p_1 \mathbf{B} : \dot{\boldsymbol{\chi}} , \tag{4.10}$$

where p_1, p_2 and p_3 are scalar functions that can depend on state variables such as strain $\boldsymbol{\varepsilon}(t)$, temperature T, or degree of cure α. Included into the formulation recalled by Lévesque *et al.* (2008), (Eq. 4.5) yields ((see Crochon *et al.*, 2010)):

$$\boldsymbol{\sigma}(t) = \frac{\partial \Xi}{\partial \boldsymbol{\varepsilon}}(t) + \left(\frac{\partial p_3}{\partial \boldsymbol{\varepsilon}} \otimes \mathbf{L}_2 : \boldsymbol{\varepsilon}(t) + p_3 \mathbf{L}_2\right) : \boldsymbol{\chi}(t) \tag{4.11a}$$

$$p_1 \mathbf{B} : \dot{\boldsymbol{\chi}} + p_2 \mathbf{L}_3 : \boldsymbol{\chi} + p_3 \left(\mathbf{L}_2\right)^{\mathrm{T}} : \boldsymbol{\varepsilon} = \mathbf{0} \tag{4.11b}$$

where Ξ is a scalar function. Solution of Equation (4.11) yields

$$\boldsymbol{\sigma}(t) = \frac{\partial \Xi}{\partial \boldsymbol{\varepsilon}} + \left(\frac{\partial p_3}{\partial \boldsymbol{\varepsilon}} \otimes \boldsymbol{\varepsilon} + p_3 \mathbf{I}\right) : \int_0^t \Delta \mathbf{C}\left(\xi(t) - \xi(\tau)\right) \frac{\mathrm{d}}{\mathrm{d}\tau}\left[\frac{p_3(\tau)}{p_2(\tau)}\boldsymbol{\varepsilon}(\tau)\right]\mathrm{d}\tau \tag{4.12}$$

where $\Delta \mathbf{C}(t) = \sum_{k=1}^N \mathbf{C_k} \exp\left(-\frac{t}{\tau_k}\right)$ and

$$\xi(t) = \int_0^t \frac{p_2(\rho)}{p_1(\rho)}\mathrm{d}\rho = \int_0^t \frac{1}{a_{\mathrm{T}}(\rho)}\mathrm{d}\rho \tag{4.13}$$

is a *reduced time*. The time (ρ) dependence of p_2 and p_3 in Equation (4.12) is interpreted through the time dependence of the state variables, on which p_2 and p_3 depend.

The factor a_{T} in Equation (4.13) is called a *shift factor*. When $p_2 = p_3 = 1$ and $p_1 = a_{\mathrm{T}}(T)$, Equation (4.13) reduces to the so-called Time Temperature Superposition Principle

(TTSP, Ferry (1980)). The TTSP can be used to construct master curves by shifting relaxation or creep curves obtained at different temperatures on the logarithmic time scale by a temperature-dependent shift factor. A good superposition of the relaxation or creep curves has to be observed. The relaxation/creep time can be extended to ensure a true superposition or tests at closer temperatures can be carried out. It was found by different authors Crowson et Arridge (1979); Sadeghinia *et al.* (2012) that for epoxy resins the evolution of a_T with temperature changes around the glass transition temperature T_g. Below T_g, it is well described by an Arrhenius relationship (Hojjati *et al.*, 2004; Miyano *et al.*, 2007)

$$\log a_\mathrm{T} = \frac{E_\mathrm{a}}{\ln 10 R}\left(\frac{1}{T} - \frac{1}{T_\mathrm{ref}}\right),\tag{4.14}$$

while above T_g, the well-known Williams-Landel-Ferry equation (WLF) (Williams *et al.*, 1955)

$$\log a_\mathrm{T} = \frac{-M_1(T - T_\mathrm{ref})}{M_2 + T - T_\mathrm{ref}}\tag{4.15}$$

is the most appropriate. In these equations, E_a is an activation energy (J/mol), R the universal gas constant (8.314 J/(Kmol)), M_1 and M_2 are adjustable material constants, and T_ref is the reference temperature.

4.4.2 The proposed viscoelastic model

In the studied strain range relevant for the formation of residual stresses, the viscoelastic behavior of the studied resin is linear with strain. The nonlinearizing functions in Equations (4.11,4.12) are therefore supposed to depend only on temperature and degree of cure. Introducing $\Xi = \frac{1}{2}\boldsymbol{\varepsilon} : \mathbf{C}_\infty : \boldsymbol{\varepsilon}$, $p_1 = p(\alpha)a_\mathrm{T}(T,\alpha)$, and $p_2 = p_3 = p(\alpha)$, Equation (4.12) becomes

$$\begin{aligned}\boldsymbol{\sigma}(t) = \mathbf{C}_\infty : \boldsymbol{\varepsilon}\\ + \int_0^t p(\alpha) \sum_{k=1}^N \mathbf{C_k} \exp\left[-\frac{1}{\tau_k}\left(\int_0^t \frac{1}{a_\mathrm{T}(T,\alpha)}\mathrm{d}\rho - \int_0^\tau \frac{1}{a_\mathrm{T}(T,\alpha)}\mathrm{d}\rho\right)\right] : \frac{\mathrm{d}\boldsymbol{\varepsilon}}{\mathrm{d}\tau}\mathrm{d}\tau\end{aligned}\tag{4.16}$$

In one dimension, Equation (5.1) reduces to:

$$\begin{aligned}\sigma(t) = C_\infty : \varepsilon\\ + \int_0^t p(\alpha) \sum_{k=1}^N C_k \exp\left[-\frac{1}{\tau_k}\left(\int_0^t \frac{1}{a_\mathrm{T}(T,\alpha)}\mathrm{d}\rho - \int_0^\tau \frac{1}{a_\mathrm{T}(T,\alpha)}\mathrm{d}\rho\right)\right] : \frac{\mathrm{d}\varepsilon}{\mathrm{d}\tau}\mathrm{d}\tau\end{aligned}\tag{4.17}$$

The model obeys the TTS principle through the cure and temperature dependent shift factors $a_T(T, \alpha)$. The relaxation modulus is written in a Prony series as in Equation (4.12). The cure dependence of the relaxation modulus is described by the function $p(\alpha)$.

4.4.3 Model identification

Shift factors

According to the TTS principle, each individual isothermal relaxation curve was shifted along the logarithmic time scale to construct master curves for every degree of cure, with 30°C taken as the reference temperature. The shift factors a_T were determined automatically with a Matlab program developed at Onera that seeks the shift along the logarithmic time scale minimizing the average distance of the stress values with respect to the relaxation curve at the next lower temperature. In this way, an independent shift factor was determined for each temperature. One shift factor set for each degree of cure is plotted for clarity in Figure 4.6. It can be seen that the temperature dependence of the shift factors is well approximated
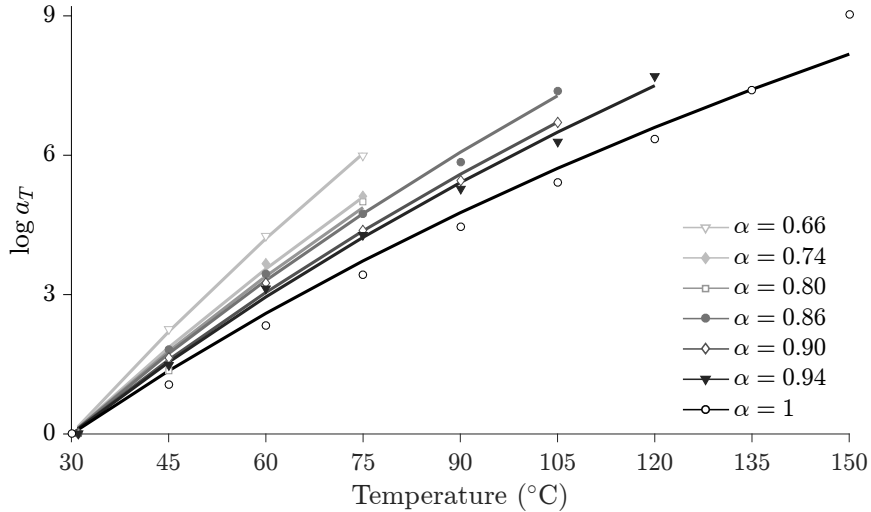
Figure 4.6 Shift factors with respect to $T_{\text{ref}} = 30°C$ as a function of the temperature $(T < T_{\text{g}})$ obtained from the master curve construction, from $\alpha = 0.66$ to $\alpha = 1$, together with the Arrhenius model identified individually for each degree of cure

by the Arrhenius relationship given by Equation (4.14). However, the slope of the curves decrease with the degree of cure, indicating that the activation energy E_{a} depends on cure.

The activation energy determined by fitting the Arrhenius model individually to the shift factors obtained for each specimen is plotted as a function of the degree of cure in Figure 4.7. A decreasing linear relationship between the degree of cure and the activation energy was observed, suggesting that the relaxation mechanisms of partially cured specimens were more

sensitive to temperature. We therefore introduce the cure dependence of the shift factors
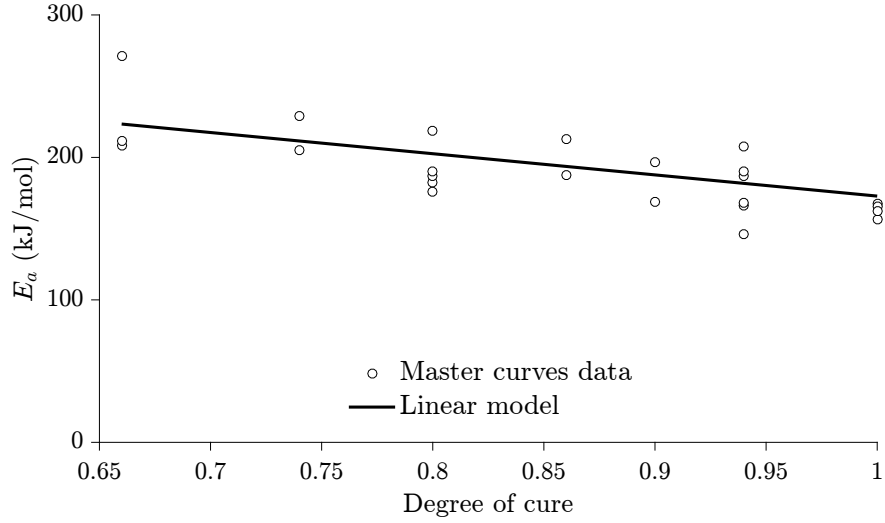
Figure 4.7 Master curve data for the E_a α-dependency, from α=0.66 to α=1.0, together with the postulated linear model

into the Arrhenius relationship (Eq. 4.14) through an activation energy of the form

$$E_\mathrm{a}(\alpha) = a\alpha + b, \tag{4.18}$$

with a and b being adjustable parameters.

Master curves

The master curves were constructed using the method described in the previous paragraph with the independent shift factors for each temperature. Figure 4.8 shows the relaxation data of a partially cured specimen for each temperature along a logarithmic time scale and the resulting master curve, with a good overlap for each step (No discontinuity in the mastercurves). This observation supports the relevance of using the TTSP for the studied epoxy resin. The master curves for each degree of cure are shown in Figure 4.9 as a function of the reduced time ξ. One curve for each degree of cure is plotted, for clarity. It can be seen that master curves for higher degrees of cure are stiffer that those for lower α. Moreover, the relaxation modulus decrease was delayed for higher degrees of cure. The same lack of hierarchy noticed in the experimental relaxation results can be observed at the beginning of the master curves, corresponding to the first temperature steps.

Every specimen master curve was independently fitted with Prony series in order to obtain a first approximation of the $E_k = p(\alpha)C_k$. The relaxation times τ_k were set to one per
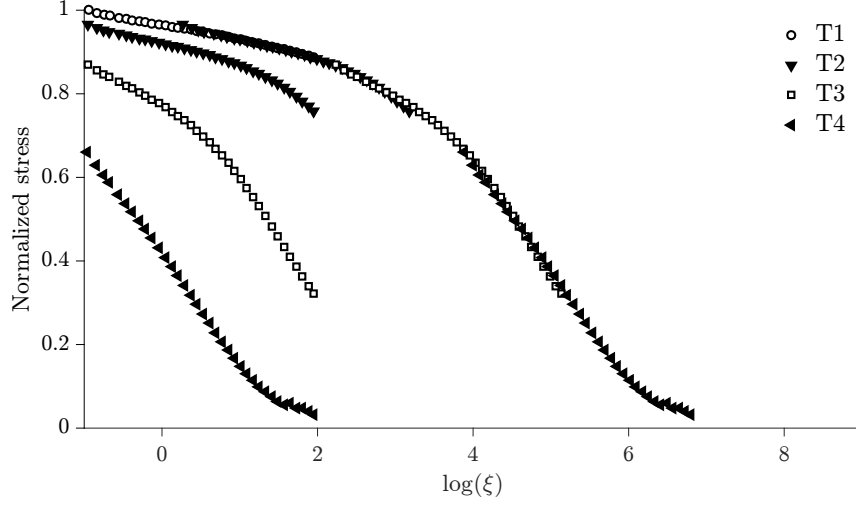
Figure 4.8 Master curve construction for a partially cured sample at $T_{\text{ref}} = 30°\text{C}$
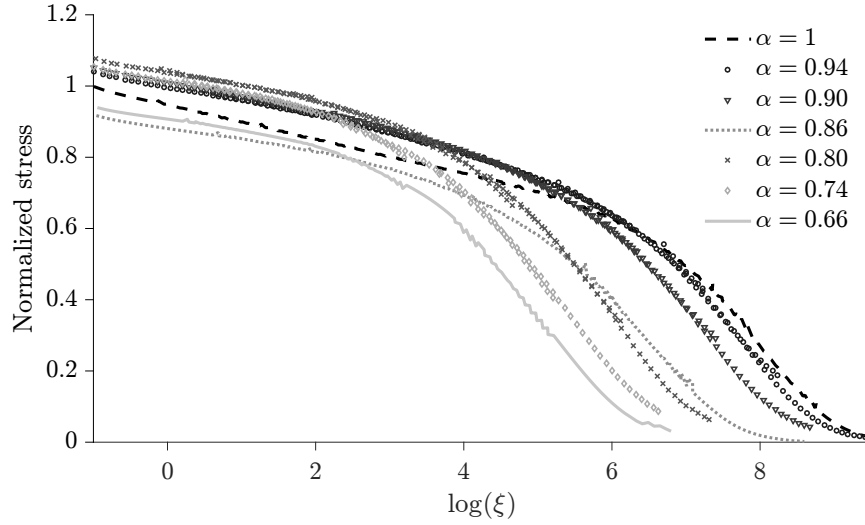
Figure 4.9 Master curves for partially and fully cured samples at $T_{\text{ref}} = 30°\text{C}$, from α=0.66 to α=1.0

decade and every E_k was associated with a τ_k such that $E_k(\tau_k)$. Similar distributions for $E_k = p(\alpha)C_k(\tau_k)$ were obtained for each degree of cure, as can be seen in Figure 4.10. These distributions exhibit a plateau of approximately constant E_k at short relaxation times, followed by a peak that can be well fitted by a Gaussian distribution at longer relaxation times. Therefore, the distribution of the $C_k(\tau_k)$ was assumed to be of the shape

$$
C_k(\tau_k) = \left[\exp\left[-\left(\frac{\log \tau_k - \log \tau_{\text{peak}}}{l_{\text{peak}}} \right)^2 \right] + \beta \left[1 - \text{erf}\left(\frac{\log \tau_k - \log \tau_{\text{peak}}}{l_{\text{peak}}} \right) \right] \right]
$$
$$
\times \frac{\log \tau_{k+1} - \log \tau_{k-1}}{2} (C_0 - C_\infty) \quad (4.19)
$$
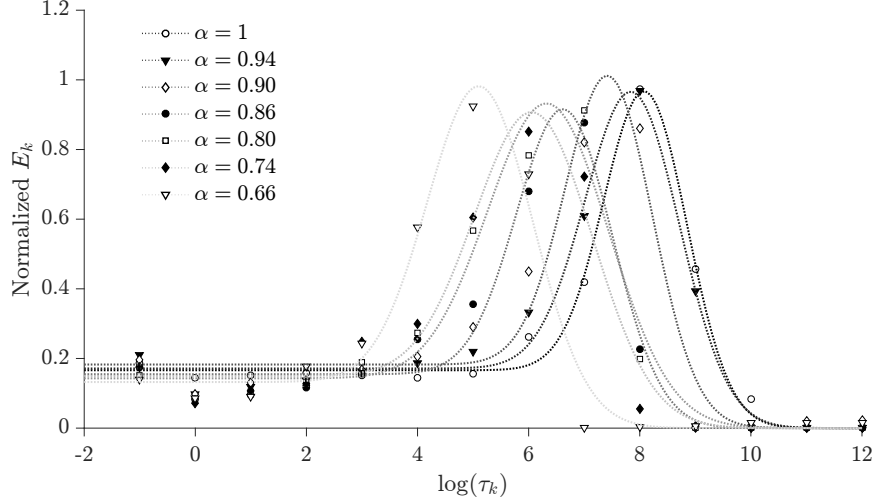
Figure 4.10 E_k distributions with $T_{\mathrm{ref}} = 30°\mathrm{C}$, from α=0.66 to α=1.0, and best fitting continuous functions (Eq. 5.2) computed individually for each degree of cure

where C_0 is the instantaneous relaxation tensor

$$C_0 = C_\infty + p \sum_{k=1}^{k} C_k \tag{4.20}$$

and β, l_{peak} and $\log \tau_{\mathrm{peak}}$ are adjustable parameters related to the peak height, the plateau height, the peak width and the position of the peak on the relaxation time axis, respectively. erf is defined as

$$\mathrm{erf}(x) = \frac{2}{\sqrt{\pi}} \int_0^x \exp(-t^2)\mathrm{d}t \tag{4.21}$$

C_k can therefore be interpreted as a sum of a Gaussian and a sigmoid distribution.

For illustration purposes, Figure 4.11 shows the discrete E_k extracted from a fully cured specimen master curve, the fitted E_k as well as the sigmoid and Gaussian parts. The advantage of using this continuous function to approximate the E_k is that it reduces greatly the number of independent parameters of the model (from 15 (one E_k per relaxation time) to 4), thus facilitating the optimization process required for obtaining the model parameters.

Influence of the degree of cure

Figure 4.10 shows that the peak position $\log \tau_{\mathrm{peak}}$ increases monotonically with the degree of cure. Since both asymptotes of the continuous function towards short relaxation times (the plateau) and long relaxation times (zero) are horizontal, instead of introducing a cure dependent peak position, an α-dependency can be introduced into the shift factors a_{T}. The approach of Simon *et al.* (2000) was adopted to use the cure dependent glass transition
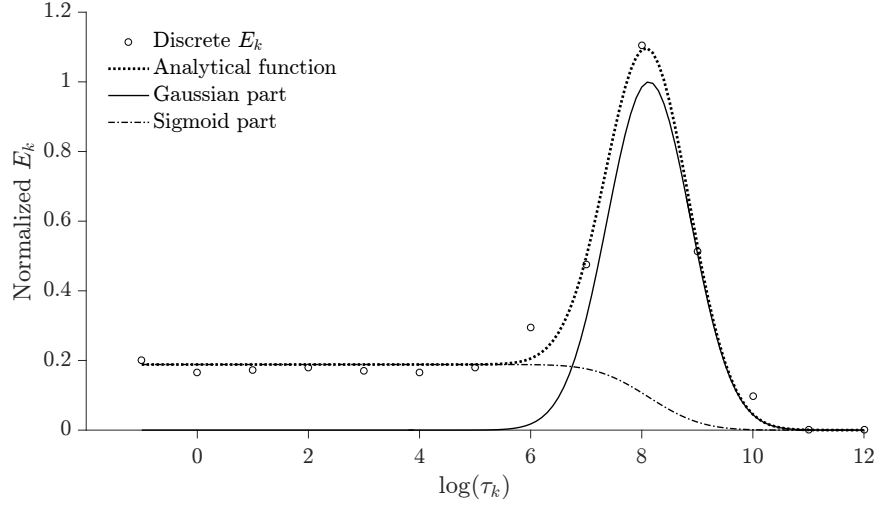
Figure 4.11 Discrete E_k values for $\alpha = 1.0$ and corresponding analytical relationship

temperature T_{g} as reference temperature for the shift factors.

The evolution of T_{g} with the degree of cure was determined from DSC measurements. It is well approximated by the DiBenedetto equation (DiBenedetto, 1987):

$$\frac{T_{\mathrm{g}} - T_{\mathrm{g}0}}{T_{\mathrm{g}\infty} - T_{\mathrm{g}0}} = \frac{\lambda\alpha}{1 - (1 - \lambda)\alpha} \tag{4.22}$$

where $T_{\mathrm{g}0}$ and $T_{\mathrm{g}\infty}$ are the glass transition temperatures of the uncured and the fully cured resin, respectively, and λ is a material parameter. Both the experimental DSC results and the DiBenedetto model are plotted in Figure 4.12.
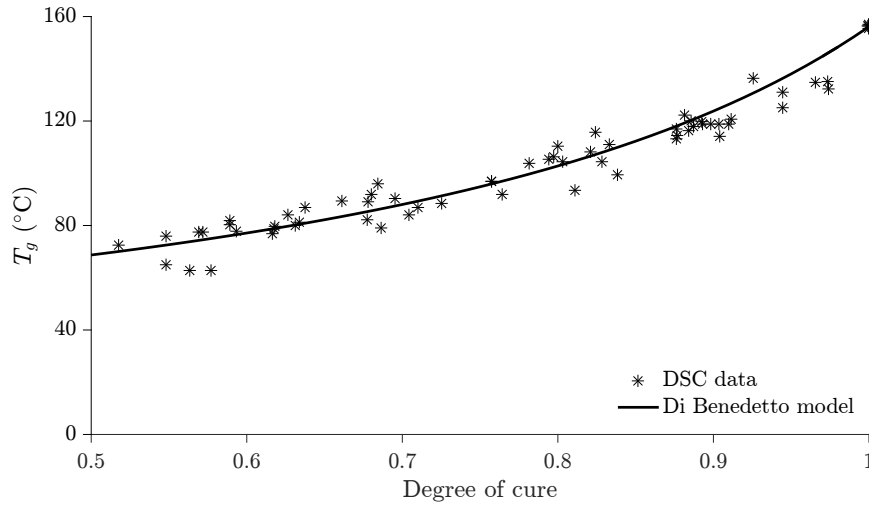
Figure 4.12 Comparison between DSC data and the DiBenedetto model

Figure 4.13 reports the same plots as that of Figure 4.10, but for each degree of cure $T_{\mathrm{ref}} =$

$T_g(\alpha)$ was taken as the reference temperature. The figure shows that the curves almost collapse into a single distribution, which confirms that the approach of Simon *et al.* (2000) is appropriate for the studied resin. However, the peak areas vary slightly with the degree of cure. Its values that yield the curves shown in Figure 4.13 are plotted in Figure 4.14 as a function of the degree of cure. The heights or widths variations lead to similar effects.
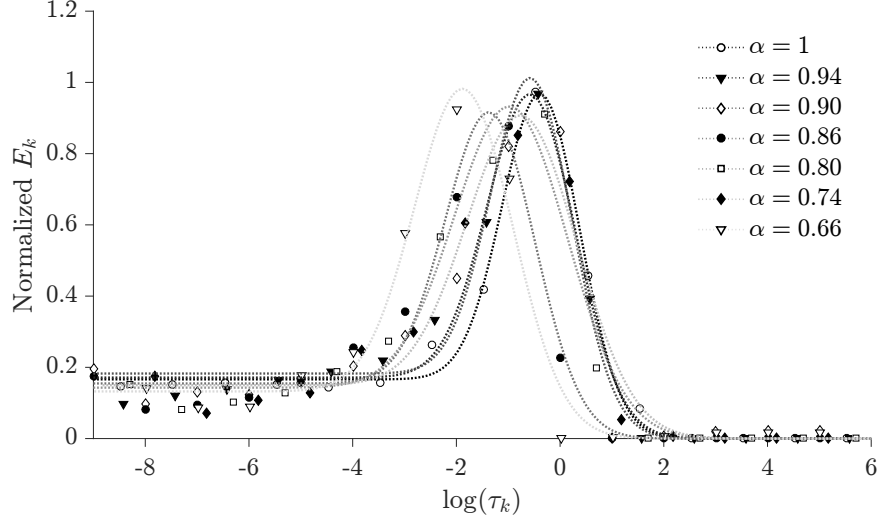
Figure 4.13 E_k distributions with $T_{\mathrm{ref}} = T_{\mathrm{g}}(\alpha)$, from α=0.66 to α=1.0
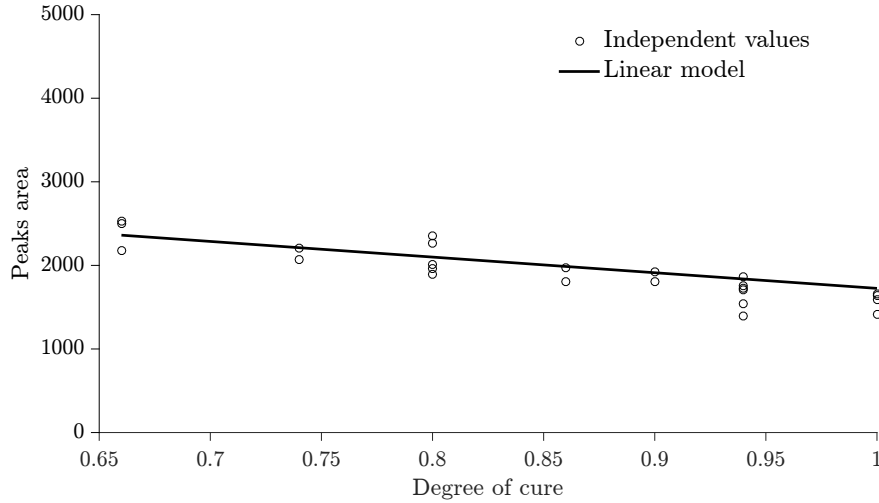
Figure 4.14 Discrete peak area values extracted from each master curve fit and a linear approximation, from α=0.66 to α=1.0

The peaks width was therefore fixed and the cure dependence focused on the peak heights and was accounting for through parameter $p(\alpha)$ in $E_k = p(\alpha)C_k$. It can be deduced that $p = \frac{area}{l_{peak}\sqrt{\pi}}$ decreases with the degree of cure, the same way as the peaks area shown in Figure

4.14. Therefore, $p(\alpha)$ was set to

$$p(\alpha) = K_1\alpha + K_2 \tag{4.23}$$

where K_i are constants.

With these specifications, the model (Eq. 4.17) reduces to

$$
\begin{aligned}
\sigma(t) = {}& C_\infty : \varepsilon \\
&+ \int_0^t p(\alpha) \sum_{k=1}^N C_k \exp\left[-\frac{1}{\tau_k}\left(\int_0^t \frac{1}{a_\mathrm{T}(T,T_\mathrm{g}(\alpha),\alpha)}\mathrm{d}\rho - \int_0^\tau \frac{1}{a_\mathrm{T}(T,T_\mathrm{g}(\alpha),\alpha)}\mathrm{d}\rho\right)\right] : \frac{\mathrm{d}\varepsilon}{\mathrm{d}\tau}\mathrm{d}\tau
\end{aligned} \tag{4.24}
$$

p_α was obtained from Equation 4.23 and involved fitting parameters K_1 and K_2. The C_k were obtained from Equation 5.2 and involved parameters β, l_peak and $\log\tau_\mathrm{peak}$. C_∞ was obtained from Equation 4.20 and involved C_0 and C_k. The shift factors a_T were computed from Equation 4.14 and involved parameters E_a and $T_\mathrm{ref} = T_g$. E_a was obtained from Equation 4.18 and involved constants a and b, as well as T_g from Equation 5.4, which involved fitting λ.

4.4.4 Numerical implementation

The model (Eq. 4.24) was implemented in Matlab using a recursive strategy (Taylor *et al.*, 1970; Muliana *et al.*, 2016). The time scale was divided into several small increments over which the strain evolution was assumed as linear as a function of time. The temperature and degree of cure were assumed constant over each increment. Under these assumptions, Equation (4.24) can be integrated and written considering the internal variables and the instantaneous relaxation tensor (Eq. 4.20):

$$\sigma = C_0\varepsilon - p\sum_{k=1}^N C_k\chi_k \tag{4.25a}$$

$$\text{where } \chi_k = \int_0^t \left[1 - \exp\left(-\frac{t-\tau}{a_\mathrm{T}\tau_k}\right)\right]\frac{\mathrm{d}\varepsilon}{\mathrm{d}\tau}\mathrm{d}\tau \tag{4.25b}$$

leading to the incremental form

$$\Delta\sigma = C_0\Delta\varepsilon - p\sum_{k=1}^N C_k\Delta\chi_k \tag{4.26}$$

C_∞, p and C_k being material constants, $\Delta\chi_k$ was developed as Machado *et al.* (2016):

$$\Delta\chi_k = \chi_k^{n+1} - \chi_k^n$$
$$= \frac{\tau_k}{\Delta\xi}\left[\frac{\Delta\xi}{\tau_k} + \exp\left(\frac{-\Delta\xi}{\tau_k}\right) - 1\right]\Delta\varepsilon + \left[1 - \exp\left(\frac{-\Delta\xi}{\tau_k}\right)\right](\varepsilon^n - \chi_k^n) \quad (4.27a)$$

$$\text{where } \Delta\xi = \frac{\Delta t}{a_\mathrm{T}} \quad (4.27b)$$

The strain state (total strain and values of the internal variables χ_k) at the end of each recovery phase was taken as the starting state of the following loading step, because 10 min of recovery plus heating was not sufficient to let the specimens fully recover. The heating phases were modeled as recovery phases with zero applied stress and increasing temperature.

4.4.5 Parameter optimization

As stated previously, each specimen master curve was first independently fitted with Prony series, yielding discrete values for the shift factors and relaxation moduli. On the basis of these discrete values, continuous functions were defined in order to reduce the number of independent parameters of the model. In the final model, these continuous functions are used to calculate the relaxation moduli E_k for each discrete relaxation time τ_k (one per decade). The parameters of the continuous functions obtained from the independent master curve fits are used as initial parameter set for an optimization of the model parameters based on a simulation of the whole experimental dataset (all relaxation and recovery curves, for all tested temperatures and degrees of cure). Only the DiBenedetto parameters, $T_{\mathrm{g}0}$, $T_{\mathrm{g}\infty}$ and λ, were identified separately from the others to fit the DSC measurements. The relaxed modulus C_∞ was also fixed separately to the horizontal asymptote of the relaxation curves of the fully cured samples at the highest temperature. The remaining seven unknown model parameters (a and b from Eq. (4.18), β, l_peak and $\log\tau_\mathrm{peak}$ from Eq. (5.2), K_1 and K_2 from Eq. (4.23)) were obtained by minimizing the cost function:

$$r = \frac{\sum(m(t_i) - d(t_i))^2}{\sum[d(t_i)]^2} \quad (4.28)$$

with Matlab's `lsqnonlin` algorithm. During the relaxation and recovery phases, $m(t_i)$ are the predicted and $d(t_i)$ the experimentally measured stress or strain, respectively. The residue of one multi-temperature relaxation test was defined as the sum of the residues of the different relaxation and recovery phases. The parameter set that minimized the discrepancies between the model predictions and the experimental data is listed in Table 4.1. The E_k calculated

with these parameters are shown in Figure 4.15 for each tested degree of cure together with the corresponding continuous functions of Equation (5.2).
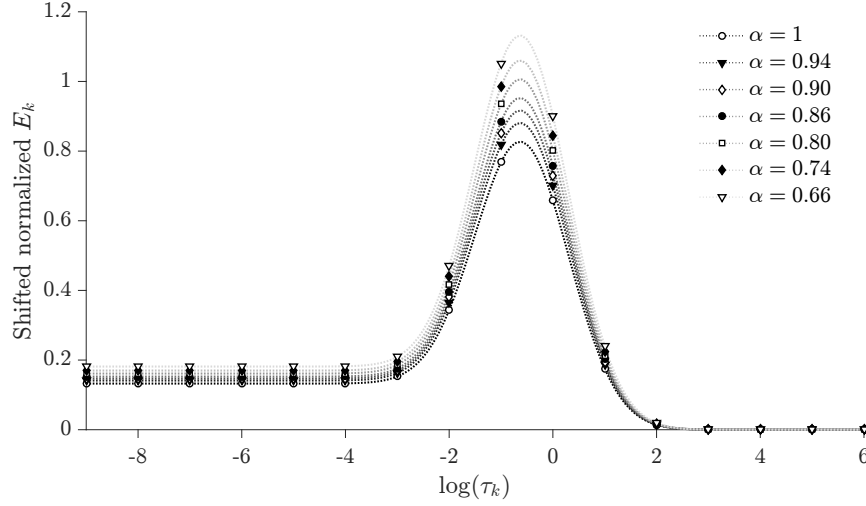
Figure 4.15 E_k values after parameter optimization, with $T_{\text{ref}} = T_{\text{g}}$

4.4.6 Comparison between model predictions and experimental relaxation data

The numerically calculated stress curves of the multi-temperature relaxation tests are shown in Figures 4.16 and 4.17 and compared to the experimental data of all tested specimens. The stress evolution predicted by the model globally lies within the experimental data range for the tested temperatures and degrees of cure, which shows that the stress evolution in time during relaxation, and its dependence on temperature and cure is well taken into account in the model. Due to the large variability in the experimental data observed for certain degrees of cure, there may be important differences between the model predictions and an individual test. It is therefore important that several tests are carried out for a given degree of cure, in order to evaluate these variabilities.

4.5 Model validation: comparison with independent experimental creep data

Creep experiments were carried out in order to test the robustness of the proposed model. Fully cured epoxy specimens were manufactured according to the protocol detailed previously.

Table 4.1 Optimized model parameters

a [kJ/mol]	b [kJ/mol]	K_1	K_2	β	l_{peak}	$\log \tau_{\text{peak}}$	λ	C_∞ [MPa]
-62.18	256.81	-363	697	0.087	1.28	-0.57	0.27	6.27
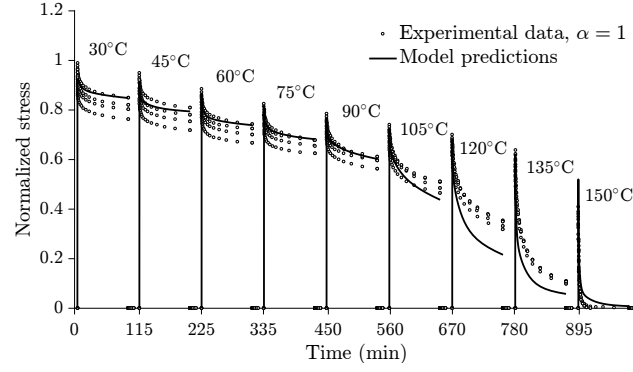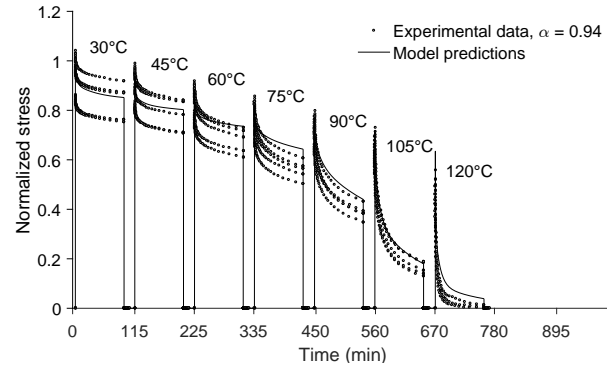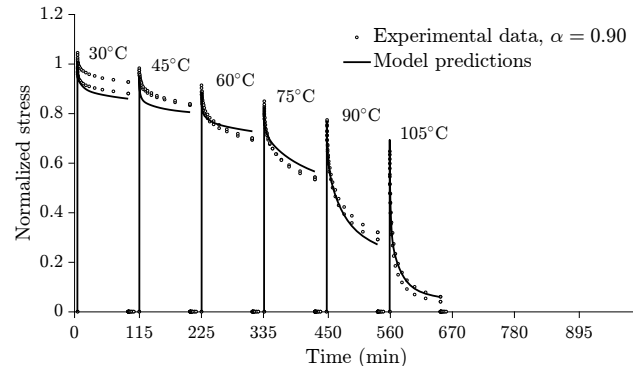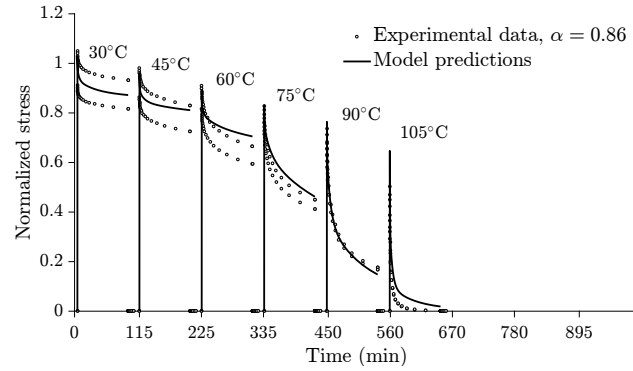
Figure 4.16 Model predictions compared to the normalized experimental stress relaxation for the fully cured specimens (a) and the specimens cured at 94% (b), 90% (c), 86% (d)
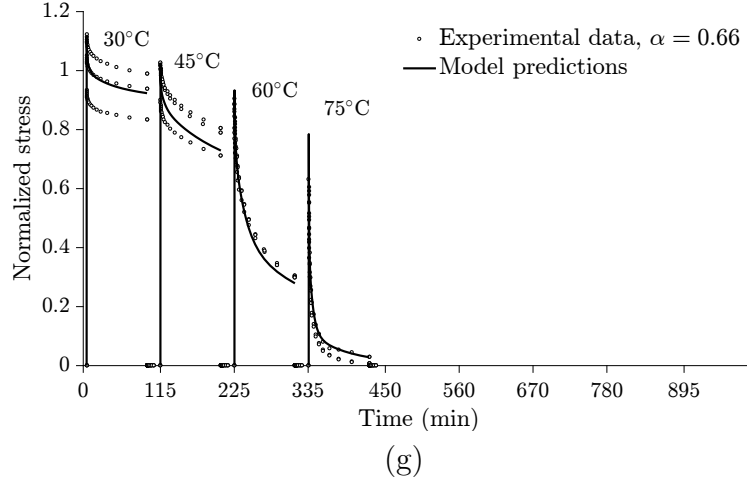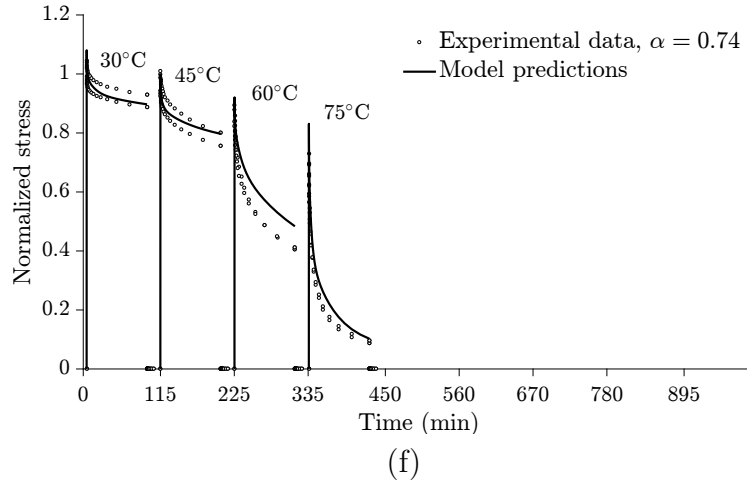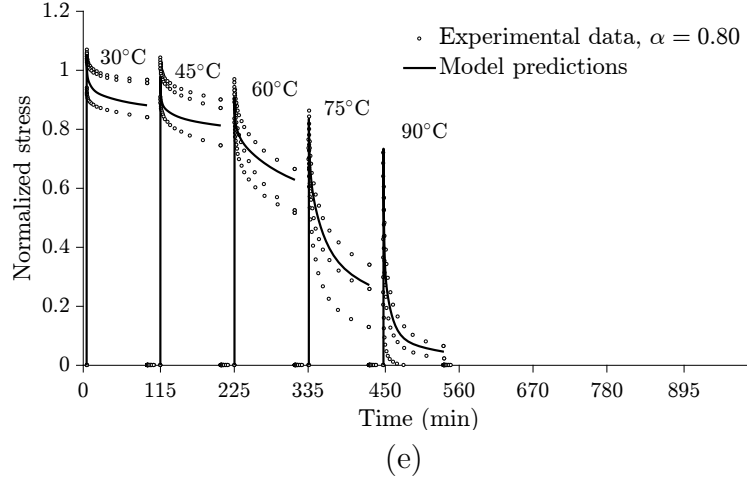
Figure 4.17 Model predictions compared to the normalized experimental stress relaxation for the fully cured specimens (a) and the specimens cured at 80% (e), 74% (f), and 66% (g)

The same DMA and clamp as described in the *Thermo-mechanical testing* section were used. These tests were deemed as a challenging validation case since model parameters were extracted from relaxation curves. Moreover, the samples were tested under non-isothermal

conditions. The thermal expansion was then taken into account, considering a CTE of $67.10^{-6}(m/(mK))$.

Temperature and force ramps were successively applied onto the specimens, as shown in Figure 4.18. The temperature ramps were of 0.5°C/min to ensure the apparatus and sample thermal equilibrium and the force ramp of 0.1N/min. After a stabilization at 30°C, a temperature ramp was applied to 45°C and a force ramp until 1N followed. Then, temperature and force ramps were alternated successively until 80°C, 1.5N, 120°C, and 2N. Finally, a temperature ramp until 150°C was applied.
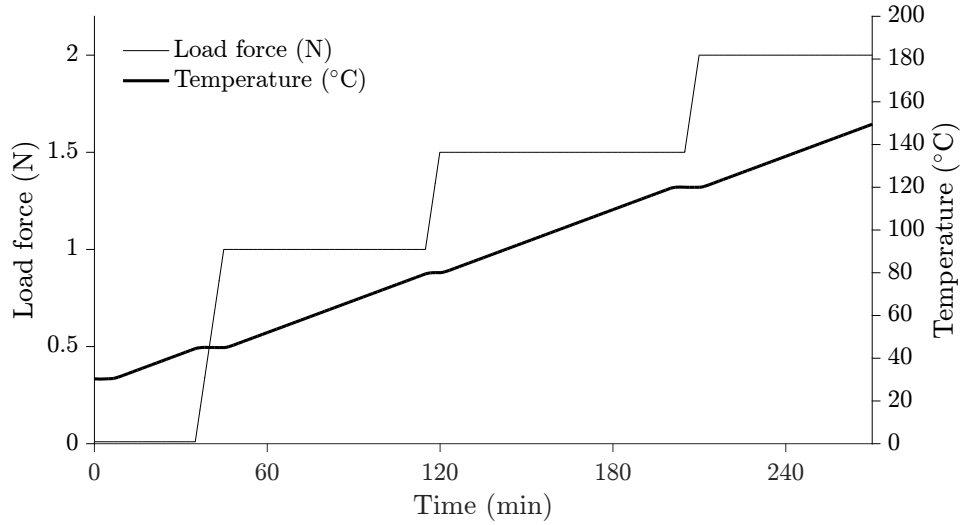
Figure 4.18 Temperature (°C) and load (N) applied on fully cured specimens

The experimentally measured strain was compared with the model predictions, considering the optimized parameters a and b from Equation 4.18, K_1 and K_2 from Equation 4.23, β, l_{peak} and $\log \tau_{\text{peak}}$ form Equation 5.2, λ from Equation 5.4 and C_∞ from 4.20, gathered in Table 4.1. Figure 4.19 shows a good agreement between the predictions and the experimental data in the range of temperatures for which the model was identified.

4.6   Discussions

It should be noted that we were expecting an increase of the instantaneous elastic stiffness with an increasing degree of cure. However, it can be seen from Figure 4.14 that p decreases with cure, which means that the instantaneous elastic stiffness also decreases with the degree of cure. A statistical analysis was carried out to confirm this trend.

The experimental data set was split into two groups : group A contained the experimental data obtained for 100% and 94% cured specimens while group B contained the experimental
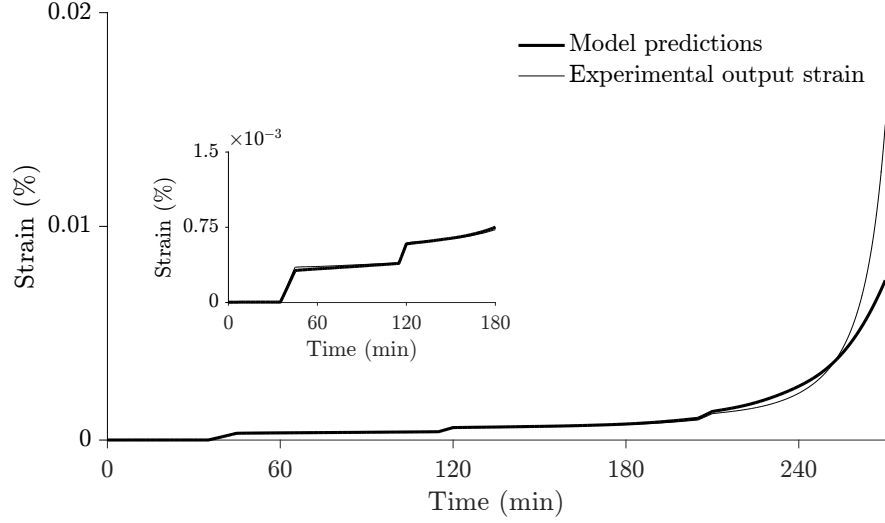
Figure 4.19 Model predictions compared to the experimental creep data on a fully cured specimen

data for 80%, 74% and 66% cured specimens. Figure 4.20 shows the mean relaxation stress curves obtained at 30°C for groups A and B, along with a 95% confidence internal on this mean value. At the lowest tested temperature, the stress relaxation is the weakest and thus the contribution of the instantaneous elastic stiffness is the most important. The figure shows that none of the confidence intervals overlap, which evidences statistically different responses between group A and group B. This observation supports the fact that the instantaneous elastic stiffness decreases with an increase in degree of cure. The chemico-physical reasons for this observation are still an open question to be investigated in the future.
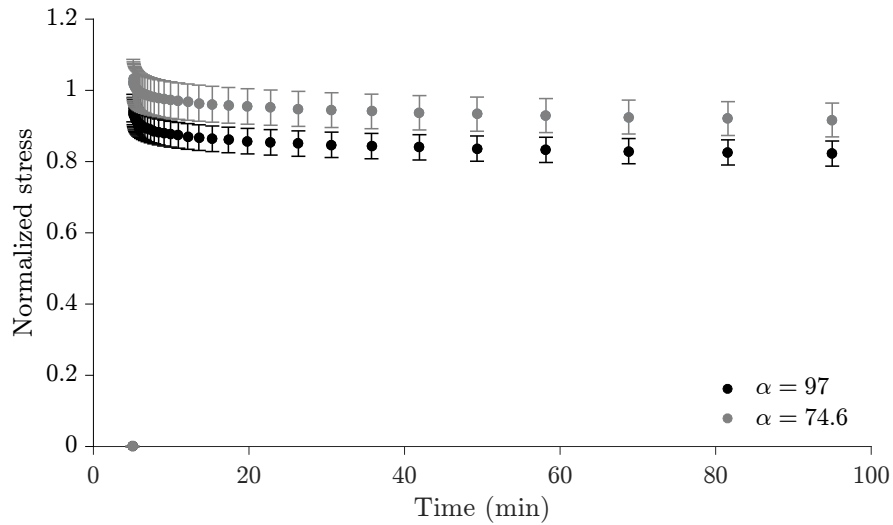
Figure 4.20 Experimental relaxation stress at 30°C, gathering the data in two groups, with confidence intervals of 95%

4.7 Conclusions

This work proposed a thermodynamically consistent viscoelastic model to predict the coupled degree of cure- and temperature-dependent response of an epoxy resin. The proposed model was able to reproduce the experimental data used for identifying its parameters within their variability. Its predictions are also in good agreement with the strain evolution observed in an independent non-isothermal multi-level creep experiment used for validating the model.

The observation of the experimental data revealed that there is a significant scatter in the results. Moreover, the partially cured samples were quite brittle, which complicated their mechanical testing. Further tests would be required to obtain more confidence in the mean responses. Moreover, it was found that partially cured samples were stiffer at low temperatures than fully cured samples, while an opposite tendency would be expected. The chemico-physical reasons for this behavior should be investigated further.

Since for the identification of the proposed viscoelastic model only unidirectional experimental data was available, its formulation in this article is limited to 1D. The model can easily be extended into 3D, but for a proper formulation of the 3D behavior, multi-axial experimental data would be needed, in particular on the evolution of the Poisson ratio during relaxation.

4.8 Acknowledgements

CHAPTER 5   ARTICLE 2 : NUMERICAL MULTISCALE HOMOGENIZATION APPROACH FOR LINEARLY VISCOELASTIC 3D INTERLOCK WOVEN COMPOSITES

A. Courtois, L. Marcin, M. Benavente, E. Ruiz, M. Lévesque (2018).

5.1   Abstract

This work aims at modeling the homogenized behavior of a polymer matrix composite reinforced with three dimensional (3D) woven fabric. The effective warp and weft tows' properties were determined by numerical homogenization with Abaqus considering elastic fibers, a viscoelastic matrix and periodic boundary conditions. The temperature- and cure-dependent linearly viscoelastic model previously developed by the authors for this particular polymer matrix was implemented into a subroutine using a differential strategy. A second homogenization procedure was carried out to obtain the mesoscopic structure homogenized behavior. Moreover, rectangular composite plates were manufactured by Resin Transfer Molding (RTM) and isothermal creep tests were carried out to study the material's viscoelastic behavior at high temperatures below the resin's glass transition temperature. Experimental results were compared to the temperature-dependent homogenized linearly viscoelastic model predictions. This model is a step forward for the accurate prediction of the residual stresses developed during the manufacturing of structural parts made out of 3D woven interlock composites.

5.2   Introduction

3D woven composites are increasingly used in structural aircraft parts (Marsh, 2006). These materials have specific in-plane properties similar to those of 2D woven composites, but much higher out-of-plane properties and delamination resistance (Mouritz *et al.*, 1999).

However, as for 2D laminates, minimizing manufacturing induced distortion is a major challenge in the production of high tolerance 3D woven composite parts. These distortions result from residual stresses generated during the process. Residual stresses originate from the mismatch in coefficients of thermal expansion (CTE) between the matrix and fibers, the matrix chemical shrinkage during cure and tool-part interactions. Residual stresses occurring during the manufacturing of laminates and woven composites have been computed using elastic and

viscoelastic models (Ruiz et Trochu, 2005a; Ding *et al.*, 2016; Benavente *et al.*, 2018). It has been recently shown that the choice of a matrix constitutive model has a decisive impact on the predictions accuracy and representativeness (Benavente *et al.*, 2018). Thermoset resins exhibit a viscoelastic behavior over their cure cycle, and, consequently, the composite's matrix-dominated properties inherit such behavior. Time-, temperature- and degree-of-cure-dependent models are therefore required to accurately predict and control distortions over the 3D composites manufacturing process.

The purpose of this work was to extend an existing temperature- and cure-dependent viscoelastic model to a 3D interlock woven composite by numerical finite element (FE) homogenization and compare the predictions to experimental creep data below the resin's glass transition temperature. The chapter is organized as follows: Section 5.3 recalls the studied material, the viscoelastic model equations, their implementation and homogenization principles. The thermodynamics admissibility of the model extension is demonstrated in Section 5.4. Sections 5.5 and 5.6 detail the micro-scale and meso-scale homogenization, respectively. Specimens manufacturing, thermomechanical testing procedure and comparison between actual creep tests results and the homogenized model predictions are described in Section 5.7.

Note that all stress values were normalized by an arbitrarily chosen scalar, for confidentiality reasons.

5.3 Background

5.3.1 Materials

A commercial DiGlycidyl Ether of Bisphenol F (DGEBF) epoxy resin was reinforced by a four-layer 3D interlock woven reinforcement made of Hexcel IM10 carbon fibers with an unbalanced warp/weft ratio yielding a fiber volume fraction V_f of 51%. Note that the resin's complete designation and the warp/weft ratio are not disclosed for confidentiality reasons.

5.3.2 Temperature- and cure-dependent viscoelastic behavior of the epoxy resin

The temperature- and cure-dependent viscoelastic constitutive model used in this paper was developed for the studied resin by the authors in a previous work (Courtois *et al.*, 2018). The constitutive model was based on the thermodynamics of irreversible processes framework developed by Biot (1954) and Schapery (1964), and recalled by Lévesque *et al.* (2008), and

reads

$$\boldsymbol{\sigma}(t) = \mathbf{C}_\infty : \boldsymbol{\varepsilon} +$$

$$\int_0^t p(\alpha) \sum_{k=1}^N \mathbf{C}^{(\mathbf{k})} \exp\left[-\frac{1}{\tau_k} \left(\int_0^t \frac{1}{a_{\mathrm{T}}(T,\alpha)} \mathrm{d}\rho - \int_0^\tau \frac{1}{a_{\mathrm{T}}(T,\alpha)} \mathrm{d}\rho \right) \right] : \frac{\mathrm{d}\boldsymbol{\varepsilon}}{\mathrm{d}\tau} \mathrm{d}\tau, \quad (5.1)$$

where $\mathbf{C}_\infty$ is the fully relaxed tensor and α the degree of cure. $p(\alpha) = K_1\alpha + K_2$, where K_1 and K_2 are adjustable parameters. The $\mathbf{C}^{(\mathbf{k})}$ are the discrete relaxation tensors associated to the relaxation times τ_k using a so-called spectrum equation as

$$\mathbf{C}^{(\mathbf{k})}(\tau_k) =$$

$$\frac{H}{l_{\mathrm{peak}}\sqrt{\pi}} \left[\exp\left[-\left(\frac{\log\tau_k - \log\tau_{\mathrm{peak}}}{l_{\mathrm{peak}}} \right)^2 \right] + \beta \left[1 - \mathrm{erf}\left(\frac{\log\tau_k - \log\tau_{\mathrm{peak}}}{l_{\mathrm{peak}}} \right) \right] \right]$$

$$\times \frac{\log\tau_{k+1} - \log\tau_{k-1}}{2} (\mathbf{C_0} - \mathbf{C}_\infty), \quad (5.2)$$

where $\mathbf{C_0}$ is the instantaneous relaxation tensor $\mathbf{C_0} = \mathbf{C}_\infty + p(\alpha) \sum_{k=1}^N \mathbf{C}^{(\mathbf{k})}$. β, H, l_{peak} and $\log\tau_{\mathrm{peak}}$ are adjustable parameters related to the plateau height, the peak's height, width and position on the relaxation time axis, respectively. Figure 5.1 shows the general spectrum shape for any component to visualize the corresponding parameters.
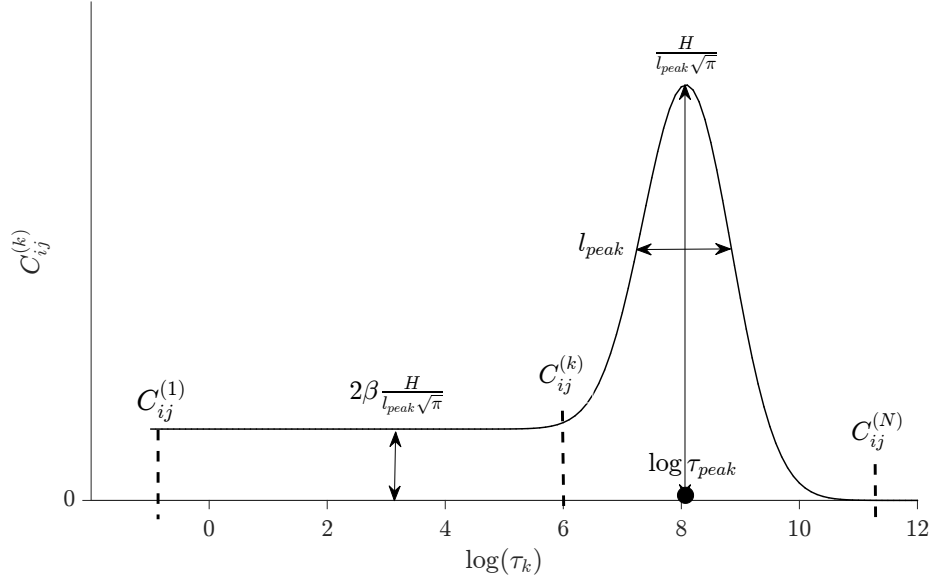
Figure 5.1 Spectrum shape for any $C_{ij}^{(k)}$. β, H, l_{peak} and $\log\tau_{\mathrm{peak}}$ are adjustable parameters related to the plateau height, the peak's height, width and position on the relaxation time axis, respectively

The erf function is defined as $\text{erf}(x) = \frac{2}{\sqrt{\pi}} \int_0^x \exp(-t^2)\mathrm{d}t$. $\xi(t) = \int_0^t \frac{1}{a_\mathrm{T}(T(\rho),\alpha(\rho))}\mathrm{d}\rho$ is defined as the reduced time and the a_T are the so-called shift factors expressed by an Arrhenius relationship as

$$\log a_\mathrm{T} = \frac{E_\mathrm{a}(\alpha)}{\ln 10 R}\left(\frac{1}{T} - \frac{1}{T_\mathrm{g}(\alpha)}\right), \quad \text{where} \quad E_\mathrm{a}(\alpha) = a\alpha + b. \tag{5.3}$$

E_a is an activation energy (J/mol), R the universal gas constant (8.314 J/(Kmol)), T_g is the reference temperature and a and b adjustable parameters. The DiBenedetto relationship (DiBenedetto, 1987) was used to express the glass transition temperature as a function of the degree of cure as

$$\frac{T_\mathrm{g} - T_\mathrm{g0}}{T_\mathrm{g\infty} - T_\mathrm{g0}} = \frac{\lambda\alpha}{1 - (1-\lambda)\alpha} , \tag{5.4}$$

where T_g0 and $T_\mathrm{g\infty}$ are the glass transition temperatures of the uncured and the fully cured resin, respectively, and λ is a material parameter. Table 5.1 lists the isotropic epoxy resin's parameters values and Figure 5.2 shows the model predictions against experimental data for two different degrees of cure. Multi-temperature relaxation tests were performed using a Dynamic Mechanical Analyser (DMA).

Table 5.1 Viscoelastic model parameters for the studied epoxy resin

a [kJ/mol]	b [kJ/mol]	K_1	K_2	β	H	l_peak	$\log \tau_\mathrm{peak}$	λ	C_∞ [MPa]
-62	257	-823	1582	0.087	1	1.28	-0.57	0.27	6.27
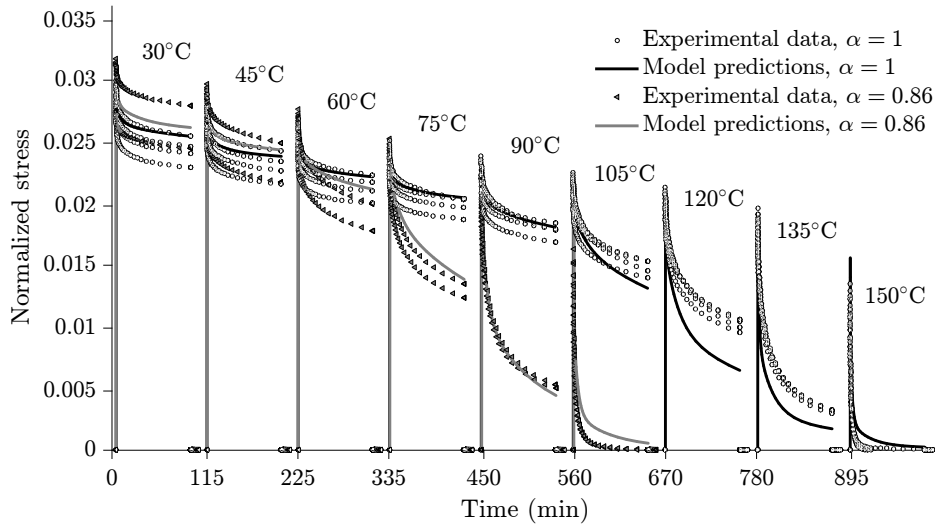
Figure 5.2 Normalized epoxy resin model predictions (continuous lines) against experimental multi-temperature relaxation data (discrete symbols) for $\alpha = 1$ and $\alpha = 0.86$

5.3.3 Viscoelastic constitutive equations implementation

Equation 5.1 can be cast under the differential shape as

$$\boldsymbol{\sigma}(t) = \mathbf{L}_1 : \boldsymbol{\varepsilon}(t) + p(\alpha)\mathbf{L}_2 : \boldsymbol{\chi}(t) \tag{5.5a}$$

$$a_{\mathrm{T}}\mathbf{B} : \dot{\boldsymbol{\chi}} + \mathbf{L}_3 : \boldsymbol{\chi} + (\mathbf{L}_2)^{\mathrm{T}} : \boldsymbol{\varepsilon} = \mathbf{0}, \tag{5.5b}$$

where $\boldsymbol{\chi}$ are internal variables, $\dot{\boldsymbol{\chi}}$ their time derivative, $\mathbf{B}$ is the identity matrix,

$$\mathbf{L}_1 = \mathbf{C}_\infty + p(\alpha)\sum_{k=1}^{N} \mathbf{C}^{(\mathbf{k})}, \tag{5.6a}$$

$$\mathbf{L}_3 = \oplus_{k=1}^{k=N} \left[\frac{1}{\tau_k}\mathbf{I}\right]. \tag{5.6b}$$

$\mathbf{L}_2$ is composed of triangular matrices obtained by the Cholesky decomposition of $\frac{1}{\tau_k}\mathbf{C}^{(\mathbf{k})}$:

$$\mathbf{L}_2 = \left(\mathbf{L}_2^{(1)}|\mathbf{L}_2^{(2)}|...|\mathbf{L}_2^{(N)}\right), \tag{5.7}$$

where
$$\mathbf{L}_2^{(k)} : \left(\mathbf{L}_2^{(k)}\right)^{\mathrm{T}} = \frac{1}{\tau_k}\mathbf{C}_k. \tag{5.8}$$

Equation 5.5 was implemented into Abaqus through a user subroutine `UMAT` using the Backward-Euler scheme (Crochon *et al.*, 2010; Benavente *et al.*, 2017) as

$$\begin{aligned}
\boldsymbol{\chi}^{n+1} &= \boldsymbol{\chi}^n + h\dot{\boldsymbol{\chi}}^{n+1} \\
&= \boldsymbol{\chi}^n - h\mathbf{A} : \left(\mathbf{L}_3 : \boldsymbol{\chi}^{n+1} + (\mathbf{L}_2)^{\mathrm{T}} : \boldsymbol{\varepsilon}^{n+1}\right) \\
&= \mathbf{W}_1 : \boldsymbol{\chi}^n + \mathbf{W}_2 : \boldsymbol{\varepsilon}^{n+1} ,
\end{aligned} \tag{5.9}$$

where h was the time increment, $\mathbf{A} = \frac{1}{a_{\mathrm{T}}(T,\alpha)}\mathbf{B}$, $\mathbf{W}_1 = (\mathbf{I} + h\mathbf{A} : \mathbf{L}_3)^{-1}$ and $\mathbf{W}_2 = -h\mathbf{W}_1 : \mathbf{A} : (\mathbf{L}_2)^{\mathrm{T}}$. The required stress at the $n+1$ step becomes

$$\boldsymbol{\sigma}^{n+1} = \mathbf{L}_1 : \boldsymbol{\varepsilon}^{n+1} + p(\alpha)\mathbf{L}_2 : \boldsymbol{\chi}^{n+1}. \tag{5.10}$$

5.3.4 Multiscale numerical homogenization

Multiscale numerical homogenization consists in computing composites effective properties from the micro- (constituents) and meso-scale (fibrous architecture) properties. 3D composites are constituted of tows arranged into a three-dimensional architecture. The tows

are themselves constituted of aligned fibers and matrix. The tows effective properties are therefore assessed from the matrix and fibers properties. Then, the composite's effective properties are computed from the tows effective properties, the tows arrangement and the matrix properties.

Full-field homogenization techniques, like finite element analyses and Fast-Fourier Transform (FFT) methods (Moulinec et Suquet, 1998), deliver local stress and strain fields and can be made as accurate as needed, irrespectively of the fibers volume fraction, provided that sufficient computational resources are available. FFT methods are mesh-free, which is a significant advantage over FE based methods. However, convergence issues arise when dealing with phases exhibiting relatively high mechanical properties contrasts. Moreover, numerical FE homogenization rely on standard commercially available codes that are supported by a wider community of users, which renders it more accessible, especially for user defined constitutive theories.

Numerical FE homogenization is typically carried out on a Representative Volume Element (RVE) to reduce the computational cost. The RVE of a 3D woven composite is typically the smallest volume whose properties are similar to those of the whole volume. Appropriate boundary conditions are applied to the RVE and the resulting stresses and strains are averaged to deduce effective properties. The effective stresses and strains $\bar{\sigma}_{ij}$ and $\bar{\varepsilon}_{ij}$ can be obtained from (Rao *et al.*, 2008; Huang et Gong, 2018)

$$\begin{cases} \bar{\sigma}_{ij} = \frac{1}{V} \int_V \sigma_{ij} dV \\ \bar{\varepsilon}_{ij} = \frac{1}{V} \int_V \varepsilon_{ij} dV \end{cases} \tag{5.11}$$

where σ_{ij} and ε_{ij} are the stresses and strains, respectively, at Gauss points, and V is the RVE volume. A linearly elastic constitutive theory is expressed as

$$\bar{\sigma}_{ij} = C_{ijkl}\bar{\varepsilon}_{kl} \tag{5.12}$$

where C_{ijkl} is the stiffness tensor.

In numerical homogenization, unit loadings are applied on a RVE and the resulting response is computed (Rao *et al.*, 2008; Choi et Sankar, 2006; Pahr et Böhm, 2008; Wang *et al.*, 2017). Then, one column of C_{ijkl} expressed under the modified Voigt notation can be obtained. For example, applying $\varepsilon = \{\varepsilon_1 = 1, \varepsilon_2 = 0, \varepsilon_3 = 0, \varepsilon_4 = 0, \varepsilon_5 = 0, \varepsilon_6 = 0\}^{\mathrm{T}}$ and computing σ_1 yields components C_{11}, C_{21}, C_{31}, C_{41}, C_{51} and C_{61} of C_{IJ}. This operation is carried out six times to obtain the full C_{ijkl} tensor.

RVE generation

Generating RVEs remains a challenge, especially for high fibers volume fraction 3D composites. Numerous software have been developed to automate RVEs construction. TexGen, based on the work of Robitaille *et al.* (1998) and Sherburn (2007), creates RVEs by accounting for the tows section variability. WiseTex, proposed by Verpoest et Lomov (2005), also accounts for tow sections variability and predicts effective properties. The recurrent issue with idealized geometry generation is the occurring of interpenetrations (when one tow penetrates through another). This situation has been dealt with by manually adding space between tows (Grail, 2013) or by extending the contact area to each surrounding tow (Perie *et al.*, 2009), for example. To prevent such issue, other authors focused on modeling the constituents and the contacts between each fiber (Wang et Sun, 2001; Zhou *et al.*, 2004; Durville, 2010; Zhou *et al.*, 2009).

The above mentioned software typically yield idealized architectures while real composites might present significant variations in their architecture. Microscopy was used to observe the real architecture of composites reinforced with 3D fabrics (Hivet et Boisse, 2005). Tomography and micro-tomography, which are non-destructive techniques, have also been used to obtain real RVEs for fibrous architectures (Stig et Hallström, 2013) and tows (Stig et Hallström, 2012). Those characterization techniques provide valuable data on effective fibers arrangement, fiber volume fraction, tows transverse sections and actual weaving, among others. However, these techniques require expensive equipment and are time-consuming (Sisodia *et al.*, 2016). Indeed, differentiating fibers/tows from the matrix and voids remains a challenge for composites with low contrast between fibers and resin. Moreover, noise is often detected during scanning, which could lead to inadmissible tows cross-sections (Madra *et al.*, 2014).

Boundary conditions

Several boundary conditions (BC) have been applied on RVEs: uniform displacement (kinematic, KUBC), uniform forces (SUBC), uniform mixed (MUBC) and periodic (PBC) boundary conditions are the most widely used (Rao *et al.*, 2008; Huang et Gong, 2018; Wang *et al.*, 2017; Van der Sluis *et al.*, 2000; Barello et Lévesque, 2008). Hazanov et Huet (1994) demonstrated that effective properties computed from MUBC lied between the effective properties computed from KUBC (upper bound) and SUBC (lower bound). Kanit *et al.* (2003), among others, demonstrated that PBC yield converged effective properties for smaller RVEs than KUBC and SUBC. Pahr et Zysset (2008) proposed a specific set of MUBC, designated as periodicity compatible mixed uniform boundary conditions (PMUBC), and proved that its

application led to the same elastic properties as the use of PBC for orthotropic materials, without the required preprocessing on the mesh when applying PBC.

Tows and composites behavior assumptions

The tows are usually considered as aligned fibers embedded into an isotropic resin, thus yielding overall transversely isotropic properties (Verpoest et Lomov, 2005; Kim *et al.*, 2008; Xu *et al.*, 2015; Staub *et al.*, 2012). In that case, the tow's stiffness matrix can be written in the form

$$\mathbf{C}_{\text{tow}} = \begin{bmatrix} C_{\text{tow},11} & C_{\text{tow},21} & C_{\text{tow},31} & 0 & 0 & 0 \\ C_{\text{tow},21} & C_{\text{tow},11} & C_{\text{tow},31} & 0 & 0 & 0 \\ C_{\text{tow},31} & C_{\text{tow},31} & C_{\text{tow},33} & 0 & 0 & 0 \\ 0 & 0 & 0 & C_{\text{tow},44} & 0 & 0 \\ 0 & 0 & 0 & 0 & C_{\text{tow},44} & 0 \\ 0 & 0 & 0 & 0 & 0 & C_{\text{tow},11} - C_{\text{tow},21} \end{bmatrix}. \tag{5.13}$$

A tranversely isotropic tensor can be decomposed with 5 projectors ($\mathbf{E_L}$, $\mathbf{J_T}$, $\mathbf{F}$, $\mathbf{K_T}$, $\mathbf{K_L}$) defined as (Bornert *et al.*, 2001b)

$$\mathbf{E_L} = \boldsymbol{n} \otimes \boldsymbol{n} \otimes \boldsymbol{n} \otimes \boldsymbol{n}, \ \mathbf{J_T} = \frac{1}{2}\boldsymbol{i_T} \otimes \boldsymbol{i_T}, \ \mathbf{F} = \frac{\sqrt{2}}{2}\left(\boldsymbol{i_T} \otimes \boldsymbol{n} \otimes \boldsymbol{n}\right)$$

$$\mathbf{K_T} = \mathbf{I_T} - \mathbf{J_T} \text{ and } \mathbf{K_L} = \mathbf{K} - \mathbf{K_T} - \mathbf{K_E} \tag{5.14}$$

where

$$\boldsymbol{i_T} = \boldsymbol{i} - \boldsymbol{n} \otimes \boldsymbol{n}, \ \mathbf{I_T} = \mathbf{I} - \boldsymbol{n} \otimes \boldsymbol{n}, \ \mathbf{K} = \mathbf{I} - \mathbf{J}$$

$$\mathbf{J} = \frac{1}{2}\boldsymbol{i} \otimes \boldsymbol{i}, \ \mathbf{K_E} = \frac{1}{6}\left(2\boldsymbol{n} \otimes \boldsymbol{n} - \boldsymbol{i_T}\right) \otimes \left(2\boldsymbol{n} \otimes \boldsymbol{n} - \boldsymbol{i_T}\right), \tag{5.15}$$

and $\boldsymbol{n}$ is the axis of transverse isotropy. A transversely isotropic tensor can then be expressed as

$$\mathbf{C}_{\text{tow}} = \kappa\mathbf{E_L} + \gamma\mathbf{J_T} + \zeta(\mathbf{F} + \mathbf{F}^T) + \delta\mathbf{K_T} + \delta'\mathbf{K_L}, \tag{5.16}$$

where κ, γ, ζ, δ, δ' are scalars. When the axis of transverse isotropy is aligned along direction 3, the stiffness matrix reads

$$\mathbf{C}_{\text{tow}} = \begin{bmatrix} \frac{\gamma+\delta}{2} & \frac{\gamma-\delta}{2} & \frac{\zeta}{\sqrt{2}} & 0 & 0 & 0 \\ \frac{\gamma-\delta}{2} & \frac{\gamma+\delta}{2} & \frac{\zeta}{\sqrt{2}} & 0 & 0 & 0 \\ \frac{\zeta}{\sqrt{2}} & \frac{\zeta}{\sqrt{2}} & \kappa & 0 & 0 & 0 \\ 0 & 0 & 0 & \delta' & 0 & 0 \\ 0 & 0 & 0 & 0 & \delta' & 0 \\ 0 & 0 & 0 & 0 & 0 & \delta \end{bmatrix}. \tag{5.17}$$

$\mathbf{C}_{\text{tow}}$ must be semi-definite positive to meet thermodynamics requirements, meaning that $\boldsymbol{v} : \mathbf{C}_{\text{tow}} : \boldsymbol{v} \geq 0$, $\forall \boldsymbol{v}$. This condition is met when

$$\begin{cases} \kappa > 0, \\ \gamma > 0, \\ \delta > 0, \\ \delta' > 0, \\ \kappa\gamma - \zeta^2 \geq 0. \end{cases} \tag{5.18}$$

Fiber tows are usually idealized by square or hexagonal fibers packings (Ansar *et al.*, 2011). Berger *et al.* (2006) evaluated the effective properties of transversely isotropic composites for both arrangements. The numerical predictions assuming a hexagonal array were similar to analytical results for fibers randomly oriented. Liu *et al.* (2012) also observed that randomly distributed fibers or fibers distributed in a regular hexagonal array yielded very close effective properties, except for the shear modulus. A rectangular geometry was usually chosen by authors to represent hexagonal packings (Choi et Sankar, 2006; Kari *et al.*, 2008; Xu *et al.*, 2012; Pathan *et al.*, 2017a) since this simplifies the imposition of PBC (Berger *et al.*, 2006). Liu *et al.* (2012) also compared experimentally measured elastic properties of unidirectionally reinforced pre-preg carbon/epoxy composites with numerical predictions using idealized fibers arrangements (random and hexagonal fibers distributions). The macroscopic elastic properties predictions using randomly distributed fibers were closer to experimental data than using hexagonal fibers distribution. However, both underestimated the transverse modulus by more than 10%.

Woven composites are often considered as orthotropic (Kim *et al.*, 2008; Xu *et al.*, 2015; Wu,

2009) and their stiffness can be expressed as

$$
\mathbf{C}_{\text{comp}} =
\begin{bmatrix}
C_{\text{comp},11} & C_{\text{comp},21} & C_{\text{comp},31} & 0 & 0 & 0 \\
C_{\text{comp},21} & C_{\text{comp},22} & C_{\text{comp},32} & 0 & 0 & 0 \\
C_{\text{comp},31} & C_{\text{comp},32} & C_{\text{comp},33} & 0 & 0 & 0 \\
0 & 0 & 0 & C_{\text{comp},44} & 0 & 0 \\
0 & 0 & 0 & 0 & C_{\text{comp},55} & 0 \\
0 & 0 & 0 & 0 & 0 & C_{\text{comp},66}
\end{bmatrix},
\tag{5.19}
$$

with 9 independent constants.

Homogenization for viscoelastic materials

Homogenization approaches considering linearly viscoelastic materials were first developed in the 1960s by Hashin (1970) and Christensen (1969). These approaches relied on the correspondence principle and analytical models such as the dilute solution, the self-consistent (Hill, 1965) and the Mori-Tanaka (Mori et Tanaka, 1973) models. Viscoelastic constitutive equations in the Laplace-Carson domain are analogous to elastic equations in the time domain. Effective properties in the Laplace-Carson domain are obtained by simply replacing the elastic properties appearing in the homogenization scheme by the transformed viscoelastic properties. The correspondence principle is widely used with analytical models (Barello et Lévesque, 2008; Lévesque *et al.*, 2004; Sullivan, 2006; Friebel *et al.*, 2006; Blanc *et al.*, 2011; El Mourid *et al.*, 2013) but was also applied in FE approaches for multiphase viscoelastic composites (Brinson et Knauss, 1992; Brinson et Lin, 1998). However, the inversion of the Laplace-Carson transform to effective properties in the time domain remains a challenge. Some authors proposed analytical time-domain approaches to bypass the inversion issue (Lahellec et Suquet, 2007; Ricaud et Masson, 2009; Sanahuja, 2013) while others proposed numerical inversions (Lévesque *et al.*, 2007; Hassanzadeh et Pooladi-Darvish, 2007).

Some authors studied the viscoelastic behavior of spherical particles reinforced matrices (Lévesque *et al.*, 2004; Fisher et Brinson, 2001; Muliana et Kim, 2007; Zhang et Li, 2009; Tran *et al.*, 2011). Fisher et Brinson (2001) predicted the mechanical properties of three-phase viscoelastic composites featuring viscoelastic interphases between the spherical inclusions and the matrix. Lévesque *et al.* (2004) worked on the behavior of nonlinearly viscoelastic composites reinforced with randomly generated spherical inclusions. Muliana et Kim (2007) proposed also a micromechanics model for composites made of linearly elastic spherical solids embedded in a nonlinearly viscoelastic matrix. Others worked on short fibers reinforced composites, like Gusev (2017) who predicted the viscoelastic stiffness for short fibers rein-

forced composites, or Staub *et al.* (2012) who proposed a preprocessing procedure to capture the fibers local orientations for speeding the finite element macroscale homogenization for anisotropic viscoelastic short fibers composites. Time-dependent unidirectional (UD) composites behavior was also studied by numerical homogenization (Zobeiry *et al.*, 2016; Pathan *et al.*, 2017b). El Mourid *et al.* (2013) studied the linearly viscoelastic behavior of woven and braided composites considering a linearly viscoelastic resin with a constant Poisson's ratio and elastic yarns.

Temperature-dependence was studied by few authors (Muliana et Haj-Ali, 2008; Sawant et Muliana, 2008). Cai et Sun (2014) predicted the thermoviscoelastic behavior of 3D braided composites and used the same time-temperature superposition relationship for the composite and for the resin. Zobeiry *et al.* (2016) implemented a temperature-dependent viscoelastic model into a FE software to model isotropic and transversely isotropic behaviors.

Experimental comparison was not included in the previously cited papers. Only few authors dealt with experimental tests to validate their predictions. Xu *et al.* (2015), who proposed a numerical time-dependent model for plain weave composites, compared their predictions against uniaxial tension relaxation tests at room temperature. Haj-Ali et Muliana (2004) proposed a numerical FE approach for nonlinearly viscoelastic composites and validated their predictions against creep and stress relaxation experimental data. The same authors extended their model to thermo-rheologically complex materials with time-temperature variations and compared homogenized predictions to experimental creep results on multi-layered composites (Muliana et Haj-Ali, 2008) and orthotropic laminates (Sawant et Muliana, 2008).

The aim of this paper was to develop and validate a numerical homogenization approach to determine the temperature-dependent viscoelastic properties of 3D interlock woven composite structures.

5.4 Model extension to anisotropic degree of cure-dependence

The previously developed model for the studied isotropic epoxy resin presented in Section 5.3.2 considered an isotropic cure-dependence through the scalar function $p(\alpha)$. As stated in Section 5.3.4, tows and woven composites are usually assumed as transversely isotropic and orthotropic, respectively. The cure-dependence was therefore adapted to such behaviors, while remaining thermodynamically admissible. The following general development was based on the work of Lévesque *et al.* (2008) and Delorme *et al.* (2017), with square matrices for mathematical practicality.

Let the internal variables $\boldsymbol{\chi}$ be decomposed into N second-order tensors, $\boldsymbol{\varepsilon_r}^k$ ($k = [1, N]$). **B**

and $\mathbf{L_3}$, which are $6N \times 6N$ fourth-order tensors, and $\mathbf{L_2}$, which is a $6 \times 6N$ fourth-order tensor, could be decomposed into 6×6 fourth-order tensors constituted of $\mathbf{B}^k$, $\mathbf{L_2}^k$ and $\mathbf{L_3}^k$ as:

$$\begin{cases} \mathbf{B} = \begin{bmatrix} \mathbf{B}^1 & 0 & & \ldots & 0 \\ 0 & \mathbf{B}^2 & & \ldots & 0 \\ \ldots & & & & \ldots \\ 0 & \ldots & \mathbf{B}^k & \ldots & 0 \\ \ldots & & & & \ldots \\ 0 & 0 & 0 \ldots & 0 & \mathbf{B}^N \end{bmatrix}, \quad \mathbf{L_3} = \begin{bmatrix} \mathbf{L_3}^1 & 0 & & \ldots & 0 \\ 0 & \mathbf{L_3}^2 & & \ldots & 0 \\ \ldots & & & & \ldots \\ 0 & \ldots & \mathbf{L_3}^k & \ldots & 0 \\ \ldots & & & & \ldots \\ 0 & 0 & 0 \ldots & 0 & \mathbf{L_3}^N \end{bmatrix}, \\ \text{and} \quad \mathbf{L_2} = \left(\mathbf{L}_2^1 | \mathbf{L}_2^2 | \ldots | \mathbf{L}_2^k | \ldots | \mathbf{L}_2^N \right). \end{cases} \tag{5.20}$$

The first and second law of thermodynamics leads to the Clausius-Duhem inequality, which becomes, for an adiabatic and isothermal loading history (Delorme *et al.*, 2017),

$$\left(\sigma - \frac{\partial \Psi}{\partial \varepsilon} \right) : \dot{\varepsilon} - \sum_{k=1}^{N} \left(\frac{\partial \Psi}{\partial \varepsilon_r^k} : \dot{\varepsilon}_r^k \right) \geq 0, \tag{5.21}$$

where Ψ is the Helmotz's free energy and ε_r^k are the internal variables. Equation 5.21 can be written as

$$\dot{\varepsilon} : \mathbf{A} : \dot{\varepsilon} + \sum_{k=1}^{N} \left(\dot{\varepsilon}_r^k : \mathbf{D}^k : \dot{\varepsilon}_r^k \right) \geq 0, \tag{5.22}$$

where

$$\mathbf{A} : \dot{\varepsilon} = \sigma - \frac{\partial \Psi}{\partial \varepsilon} \tag{5.23a}$$

$$\mathbf{D}^k : \dot{\varepsilon}_r^k = -\frac{\partial \Psi}{\partial \varepsilon_r^k} . \tag{5.23b}$$

$\mathbf{A}$ and $\mathbf{D}^k$ are symmetric positive definite. Define $\mathbf{D}^k$ as:

$$\mathbf{D}^k = \mathbf{p} \odot \mathbf{B}^k, \tag{5.24}$$

where $\mathbf{p}$ (previously a scalar function) is now a fourth order tensor to introduce transversely isotropic, orthotropic or anisotropic cure-dependence through $p_{ij} = K_{1,ij}\alpha + K_{2,ij}$, $\forall i, j$. $\odot$ refers to the Hadamard product (Styan, 1973), which is associative, distributive and commutative. The Schur product theorem states that the Hadamard product of two positive definite matrices is also positive definite (Styan, 1973). Therefore, if $\mathbf{B}^k$ and $\mathbf{p}$ are symmetric and positive definite, then $\mathbf{D}^k$ is symmetric and positive definite. This results also holds for

semi-definite positive matrices. In linear viscoelasticity, Ψ can be expressed as a second-order Taylor expansion of the internal variables around a reference state (Lévesque *et al.*, 2008). The reference state can be set to $\boldsymbol{\varepsilon} = \boldsymbol{\varepsilon}_r^k = \mathbf{0}$ and it is assumed that Ψ is minimum in the reference state so that its gradient is null. A degree of cure-dependent free energy becomes therefore

$$\Psi = \frac{1}{2}\boldsymbol{\varepsilon} : \mathbf{L_1} : \boldsymbol{\varepsilon} + \sum_{k=1}^{N} \left[\boldsymbol{\varepsilon_r}^k : \left(\mathbf{p} \odot \mathbf{L_2}^k \right) : \boldsymbol{\varepsilon} + \frac{1}{2}\boldsymbol{\varepsilon_r}^k : \left(\mathbf{p} \odot \mathbf{L_3}^k \right) : \boldsymbol{\varepsilon_r}^k \right] \tag{5.25}$$

where

$$\mathbf{L_1} = \frac{\partial^2 \Psi}{\partial^2 \boldsymbol{\varepsilon}}, \tag{5.26a}$$

$$\mathbf{L_2}^k = \frac{\partial^2 \Psi}{\partial \boldsymbol{\varepsilon} \partial \boldsymbol{\varepsilon_r}^k}, \tag{5.26b}$$

$$\text{and} \quad \mathbf{L_3}^k = \frac{\partial^2 \Psi}{\partial^2 \boldsymbol{\varepsilon_r}^k}. \tag{5.26c}$$

Inserting Equation 5.25 into Equation 5.23b yields a coupled system as

$$\forall k \in [1; N], \quad \left(\mathbf{p} \odot \mathbf{L_3}^k : \boldsymbol{\varepsilon_r}^k + \mathbf{p} \odot \mathbf{L_2}^k : \boldsymbol{\varepsilon} \right) = -\mathbf{p} \odot \mathbf{B}^k : \dot{\boldsymbol{\varepsilon}}_r^k. \tag{5.27}$$

If $\mathbf{p}_{ij} \neq 0 \quad \forall i, j$, Equation 5.27 can be multiplied by $\mathbf{p}^{-1,H}$ (Hadamard inverse) and becomes

$$\forall k \in [1; N], \ \dot{\boldsymbol{\varepsilon}}_r^k + \left(\left(\mathbf{B}^k \right)^{-1} : \mathbf{L_3}^k \right) : \boldsymbol{\varepsilon_r}^k = - \left(\left(\mathbf{B}^k \right)^{-1} : \mathbf{L_2}^k \right) : \boldsymbol{\varepsilon}. \tag{5.28}$$

Since $\mathbf{B}^k$, $\mathbf{L_2}^k$ and $\mathbf{L_3}^k$ are symmetric positive definite and commutable pairwise (proof in the work of Delorme *et al.* (2017)), Equation 5.28 can be diagonalized. Differential equations 5.28 can then be dissociated and their solution reads

$$\forall k \in [1; N], \quad \boldsymbol{\varepsilon_r}^k = - \int_0^t \left[1 - \exp\left(-\frac{t - \tau}{a_\mathrm{T} \tau_k} \right) \right] \left(\mathbf{L_3}^k \right)^{-1} : \mathbf{L_2}^k : \frac{\mathrm{d}\boldsymbol{\varepsilon}}{\mathrm{d}\tau} \mathrm{d}\tau, \tag{5.29}$$

where

$$\frac{1}{a_\mathrm{T} \tau_k} \mathbf{I} = \left(\mathbf{B}^k \right)^{-1} : \mathbf{L_3}^k. \tag{5.30}$$

a_T is the shift factor scalar function and temperature and degre of cure are assumed constant over time increment. Since the Clausius-Duhem inequality must be met for all load history, it must be met for a reversible loading history, for which the internal variables remain constant

(Lévesque *et al.*, 2008):

$$\boldsymbol{\sigma} = \left.\frac{\partial \Psi}{\partial \varepsilon}\right|_{\varepsilon_r{}^k = \text{cte}} = \mathbf{L_1} : \boldsymbol{\varepsilon} + \sum_{k=1}^{N} \left(\mathbf{p} \odot \mathbf{L_2}^k\right) : \boldsymbol{\varepsilon}_r{}^k. \tag{5.31}$$

Combining Equations 5.29 and 5.31 yields

$$\boldsymbol{\sigma} = \mathbf{L_1} : \boldsymbol{\varepsilon} - \sum_{k=1}^{N} \left(\mathbf{p} \odot \mathbf{L_2}^k\right) : \left[\left(\mathbf{L_3}^k\right)^{-1} : \mathbf{L_2}^k\right] : \boldsymbol{\varepsilon}$$

$$+ \int_0^t \sum_{k=1}^{N} \left(\mathbf{p} \odot \mathbf{L_2}^k\right) : \left[\left(\mathbf{L_3}^k\right)^{-1} : \mathbf{L_2}^k\right] \exp\left(-\frac{t - \tau}{a_{\mathrm{T}} \tau_k}\right) : \frac{\mathrm{d}\varepsilon}{\mathrm{d}\tau} \mathrm{d}\tau. \tag{5.32}$$

If $\mathbf{L_1}$, $\mathbf{L_2}^k$ and $\mathbf{L_3}^k$ are set to

$$\mathbf{L_1} = \mathbf{C}_\infty + \sum_{k=1}^{N} \mathbf{p} \odot \mathbf{C}^k, \tag{5.33a}$$

$$\mathbf{L_2}^k = -\mathbf{C}^k, \tag{5.33b}$$

$$\text{and} \quad \mathbf{L_3}^k = \mathbf{C}^k, \tag{5.33c}$$

Equation 5.32 becomes

$$\boldsymbol{\sigma} = \mathbf{C}_\infty : \boldsymbol{\varepsilon} + \int_0^t \sum_{k=1}^{N} \mathbf{p} \odot \mathbf{C}^k \exp\left(-\frac{t - \tau}{a_{\mathrm{T}} \tau_k}\right) : \frac{\mathrm{d}\varepsilon}{\mathrm{d}\tau} \mathrm{d}\tau. \tag{5.34}$$

Equation 5.34 is equivalent to Equation 5.1, except that the scalar function $p(\alpha)$ is now a symmetric positive definite fourth-order tensor $\mathbf{p}(\alpha)$ with non-zero components.

5.5 Microscale model: effective tows properties

5.5.1 Assumptions

The carbon fibers were considered as linearly elastic and the epoxy resin obeyed the temperature - and cure-dependent linearly viscoelastic behavior described in Equations 5.1 and 5.2. The fibers packing was assumed to be hexagonal for the warp and weft tows. The warp and weft tows' fiber volume fractions were set to 68% and 58%, respectively, to be consistent with the warp/weft ratio and the composite's fiber volume fraction (51%). The fibers diameter was $4.4\mu m$ and their properties were obtained from their manufacturer technical data sheet: $E_{f,11} = E_{f,22} = 10300$ MPa, $E_{f,33} = 310000$ MPa, $G_{f,12} = 4000$ MPa, $G_{f,13} = G_{f,23} = 27900$ MPa, $\nu_{f,12} = 0.3$, $\nu_{f,13} = \nu_{f,23} = 0.01$.

5.5.2 Finite Element simulations methodology

An hexagonal cell of 8.8 μm × 5.08 μm × 1 μm was generated in Abaqus, as shown in Figure 5.3. 12840 quadratic wedge elements were used in the mesh after a mesh convergence study. Elastic analysis, with no cure or temperature dependence, was run with the resin's and fibers' elastic properties. Figure 5.4 shows the total CPU time and the relative error, err_m, between the elastic stress σ_1 resulting from a unit strain application in the direction 1 for different numbers of elements, $N_{elements}$, and the finest mesh stress response. The chosen mesh is highlighted by a dashed line and convergence was assumed to all the other components of stress for the warp and weft tows. The number of elements was increased by uniformly decreasing their sizes throughout the whole mesh. Periodic boundary conditions application on all sides and post-processing were done with home-made python scripts, inspired by Barbero (2013), and the homogenization toolbox for Abaqus, Homtools (Lejeunes et Bourgeois, 2011).

Once the converged mesh was identified, isothermal relaxation tests of 120 minutes were simulated for three different degrees of cure (0.65, 0.85 and 1) and for temperatures from 30°C to a temperature just below the resin's degree of cure dependent glass transition temperature. The unitary load cases discussed at Section 5.3.4 were applied to compute the full tensorial warp and weft tows effective properties. Table 5.2 summarizes the simulations performed for each load case, for the warp and weft tows.

5.5.3 Finite Element simulations results

The resulting stiffness tensors, $\mathbf{C}_m(t) = \mathbf{C}_\infty + \sum_{k=1}^{N} \mathbf{p} \odot \mathbf{C}_m^{(k)} \exp\left(-\frac{t-\tau}{a_T \tau_k}\right)$ (m for microscopic scale), at any t, were symmetric but not exactly transversely isotropic, as expected by using the hexagonal fibers packing rectangular geometry. Discrepancies ranging from 0.3% at 30°C to 2% at 150°C were observed between $C_{m,11}$ and $C_{m,22}$, and $C_{m,13}$ and $C_{m,23}$. These discrepancies were deemed sufficiently small to assume a transversely isotropic behavior.

Figure 5.5 plots the components evolution as a function of time resulting from the applied unitary load in direction 1 at 120°C for $\alpha = 1$ ($C_{m,11}(t)$, $C_{m,21}(t)$ and $C_{m,31}(t)$), for the warp

Table 5.2 Summary of the 120 minutes FE relaxation simulations run for each of the six unit load cases to compute the full tensorial warp and weft tows effective properties

	$\alpha = 0.65$	$\alpha = 0.85$	$\alpha = 1$	simulations
Temperature (°C)	30, 45, 60, 75	30, 45, 60, 75, 90, 105	30, 45, 60, 75, 90, 105, 120, 135, 150	19
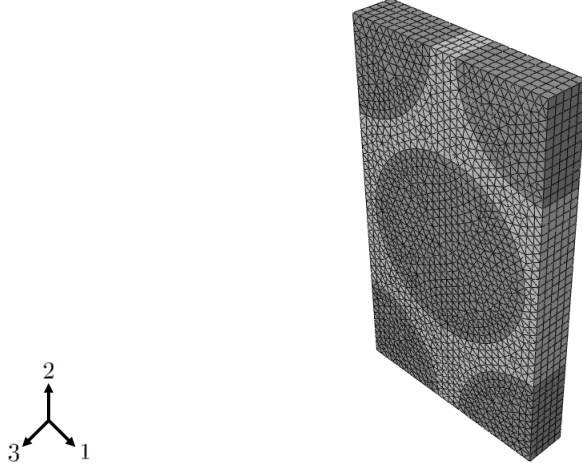
Figure 5.3 Warp tows microscopic homogenization meshed RVE. Dimensions: $8.8\mu m \times 5.08\mu m \times 1\mu m$, $V_f = 68\%$, 12840 wedge elements. Periodic boundary conditions were applied on all sides

tows. The simulations were repeated for every conditions (degree of cure and temperature) indicated in Table 5.2 for each unit load case. Master curves were then constructed for each component from the multi-temperature relaxation results to compute the corresponding shift factors for the warp tows. Figure 5.6 shows the master curves for the warp tows stiffness component $C_{m,11}$ only, for clarity, for the three different degrees of cure. The parameter $E_a(\alpha)$ (Equation 5.3) was then optimized to fit the shift factors using the `fminsearch` algorithm in Matlab R2015b, for each component. The parameters from the DiBenedetto relationship (Equation 5.4) were fixed to the values obtained for the neat resin as it relates the degrees of cure and T_g. Figure 5.7 compares the neat resin's linear model for E_a as a function of the degree of cure against the $C_{m,11}$'s optimized values for E_a and their corresponding linear model. $E_a(\alpha)$ for $C_{m,11}$ seems to obey a similar linear model as that of the epoxy resin (Figure 5.7) and, therefore, a similar Arrhenius law. The same results were obtained for the other components. The parameters a and b (Equation 5.3) were therefore set to the values obtained for the neat resin (see Table 5.1) for the rest of this work. The warp tows experienced actually the same temperature-dependence as the neat resin.

5.5.4 Tows effective properties determination

Table 5.3 outlines the general model parameters for any behavior in 3D. Different spectra for each component could then be identified. The parameters a and b (Equation 5.3) and λ (Equation 5.4) were fixed to the values identified for the neat resin (see Section 5.5.3). The relaxed moduli $\mathbf{C}_{m,\infty}$ components were independently set to the last values ($t = 120$ minutes) of the corresponding relaxation curves for the fully cured composite loaded at the highest

Figure 5.4 Mesh convergence study for the microscale homogenization. Relative error (%), between the elastic stress σ_1 resulting from a unit strain application in the direction 1 and the finest mesh stress response, and total CPU time are plotted as a function of the number of elements $N_{elements}$. The chosen mesh is emphasized by a dashed line.
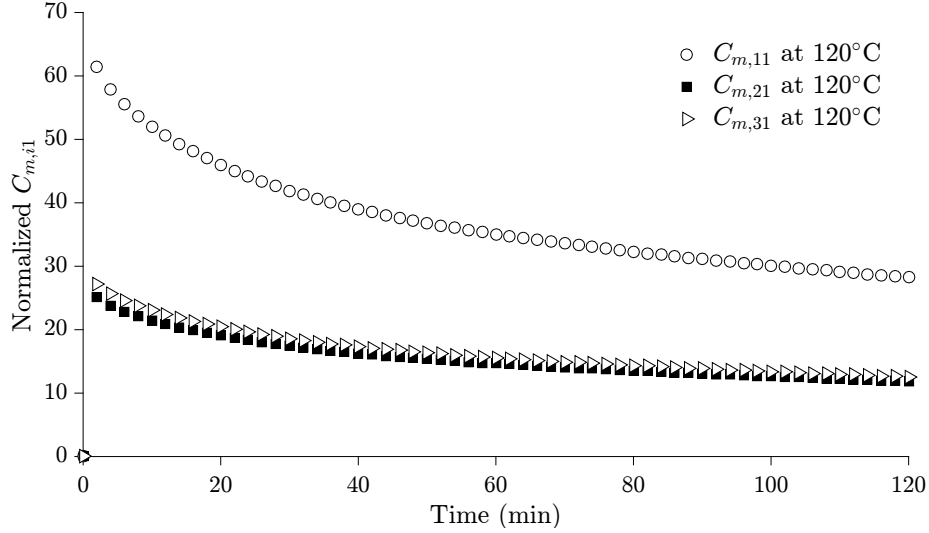
Figure 5.5 Resulting warp tows stiffness components evolution at 120°C for $\alpha = 1$, applying unitary load in direction 1

Table 5.3 Summary of the general viscoelastic model parameters for any behavior

Parameters								
$\mathbf{C}_\infty$	$\mathbf{p}_{ij}(\alpha)$		$\mathbf{C}_{ij}^{(k)}$				a_{T}	
	$K_{1,ij}$	$K_{2,ij}$	H_{ij}	β_{ij}	$l_{\mathrm{peak},ij}$	$\log \tau_{\mathrm{peak},ij}$	E_a	T_g
							a b	λ
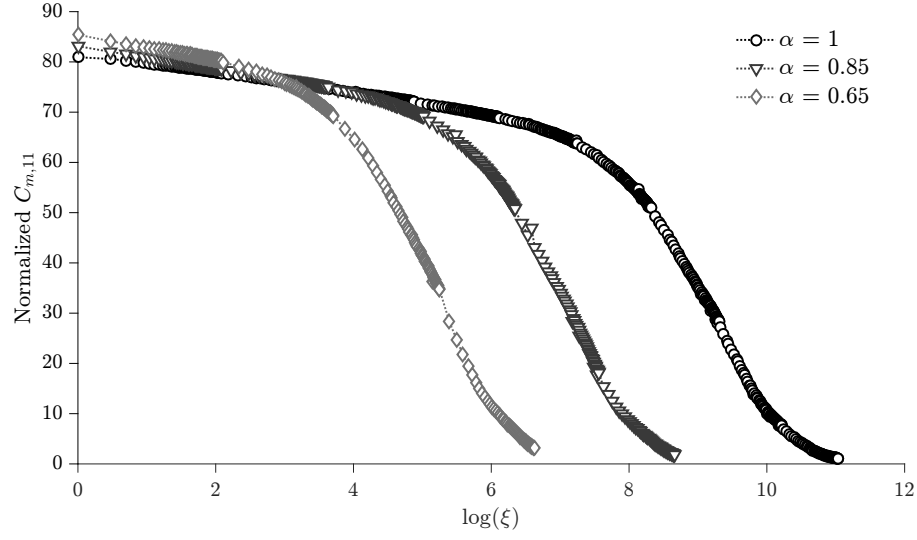
Figure 5.6 $C_{m,11}$ master curves for $\alpha = 1$, 0.85 and 0.65 with $T_{\text{ref}} = 30°$C, from the loading case $\boldsymbol{\varepsilon_1} = 1$, $\boldsymbol{\varepsilon_i} = 0$ $\quad \forall i \neq 1$, for the warp tows. ξ is the reduced time
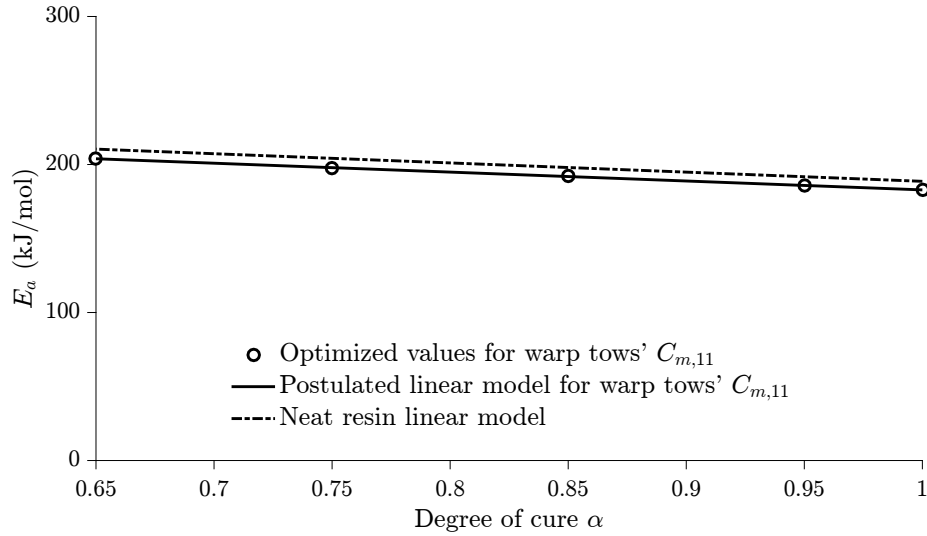
Figure 5.7 E_a optimized values for $C_{m,11}$, from $\alpha = 0.65$ to $\alpha = 1.0$, together with the postulated linear model and the resin's linear model

temperature to reduce the number of parameters. The parameters $K_{1,ij}$, $K_{2,ij}$, H_{ij}, β_{ij}, $l_{\text{peak},ij}$, $\log \tau_{\text{peak},ij}$ (Equation 5.2) remained to be determined for each component.

Based on Equations 5.17 and 5.34, the transversely isotropic behavior was identified from:

$$\mathbf{E}_m^{(k)} = \mathbf{p}_m(\alpha) \odot \mathbf{C}_m^{(k)} =$$

$$\begin{bmatrix} p_{m,11}\dfrac{\left(C_{m,11}^{(k)}+C_{m,66}^{(k)}\right)}{2} & p_{m,11}\dfrac{\left(C_{m,11}^{(k)}-C_{m,66}^{(k)}\right)}{2} & p_{m,11}\dfrac{C_{m,31}^{(k)}}{\sqrt{2}} & 0 & 0 & 0 \\ p_{m,11}\dfrac{\left(C_{m,11}^{(k)}-C_{m,66}^{(k)}\right)}{2} & p_{m,11}\dfrac{\left(C_{m,11}^{(k)}+C_{m,66}^{(k)}\right)}{2} & p_{m,11}\dfrac{C_{m,31}^{(k)}}{\sqrt{2}} & 0 & 0 & 0 \\ p_{m,11}\dfrac{C_{m,31}^{(k)}}{\sqrt{2}} & p_{m,11}\dfrac{C_{m,31}^{(k)}}{\sqrt{2}} & p_{m,11}C_{m,33}^{(k)} & 0 & 0 & 0 \\ 0 & 0 & 0 & p_{m,44}C_{m,44}^{(k)} & 0 & 0 \\ 0 & 0 & 0 & 0 & p_{m,44}C_{m,44}^{(k)} & 0 \\ 0 & 0 & 0 & 0 & 0 & p_{m,11}C_{m,66}^{(k)} \end{bmatrix} \quad (5.35)$$

where $p_{m,ii} = K_{1,ii}\alpha + K_{2,ii}$, $i = \{1,4\}$.

$E_{m,44}^{(k)} = E_{m,55}^{(k)}$ and $E_{m,66}^{(k)}$ were first determined independently by minimizing the cost function:

$$r = \frac{\sum_l (q(t_l) - s(t_l))^2}{\sum_l [s(t_l)]^2} \quad (5.36)$$

where $q(t_l)$ are the predicted and $s(t_l)$ the Abaqus simulated shear components, with the conditions $p_{m,44} > 0$, $C_{m,44}^{(k)} > 0$ and $p_{m,11} > 0$, $C_{m,66}^{(k)} > 0$, respectively, so that $E_{m,44}^{(k)} = E_{m,55}^{(k)} > 0$ and $E_{m,66}^{(k)} > 0$ (see Equation 5.18). The optimized parameters are listed in Table 5.4 and Figure 5.8 shows the simulated shear components with their corresponding predicted evolution for $\alpha = 1$ at 30°C and 120°C.
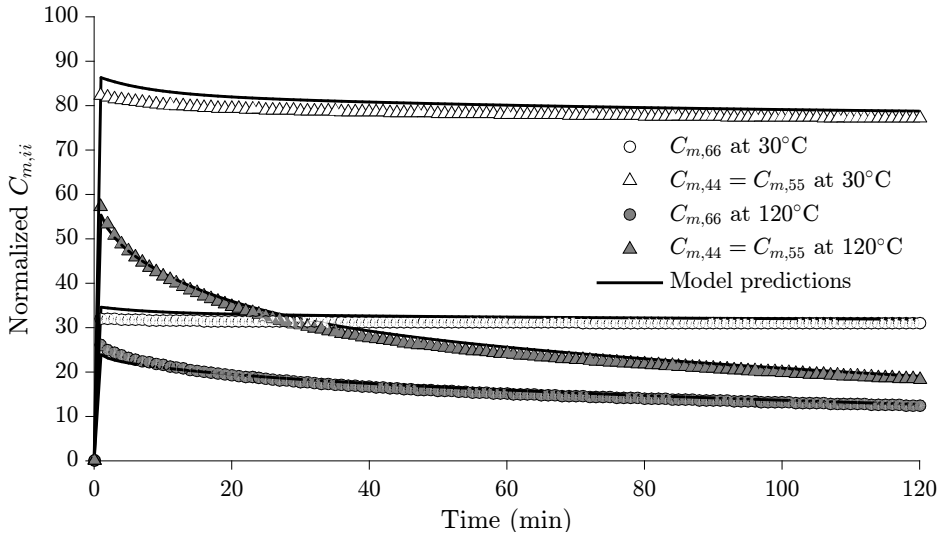
Figure 5.8 Normalized shear components evolution ($C_{m,ii}$, $i = \{4, 5, 6\}$) at 30°C and 120°C for $\alpha = 1$: simulations results are presented against the model predictions for the warp tows

$E_{m,11}^{(k)} = E_{m,22}^{(k)}$, $E_{m,21}^{(k)} = E_{m,12}^{(k)}$, $E_{m,33}^{(k)}$ and $E_{m,31}^{(k)} = E_{m,32}^{(k)} = E_{m,13}^{(k)} = E_{m,23}^{(k)}$ were then determined by minimizing the cost function

$$r_a = \sum r_{ij} \quad \text{where} \quad r_{ij} = \frac{\sum_l (q_{ij}(t_l) - s_{ij}(t_l))^2}{\sum_l [s_{ij}(t_l)]^2}, \quad i,j = \{1,2,3\}. \tag{5.37}$$

$q_{ij}(t_l)$ are the predicted and $s_{ij}(t_l)$ the Abaqus simulated stiffness components evolution, with the conditions $C_{m,11}^{(k)} > 0$, $C_{m,33}^{(k)} > 0$ and $C_{m,11}^{(k)} C_{m,33}^{(k)} - \left(C_{m,31}^{(k)}\right)^2 > 0$, so that Equation 5.18 was fulfilled and $E_m^{(k)} > 0$, using $C_{m,66}^{(k)}$ from the previous optimization. The optimized parameters are listed in Table 5.4 and Figure 5.9 shows the $E_{m,ij}$, $i,j = \{1,2,3\}$, with their corresponding predictive evolution for $\alpha = 1$ at 30°C. Table 5.5 lists the parameter sets for
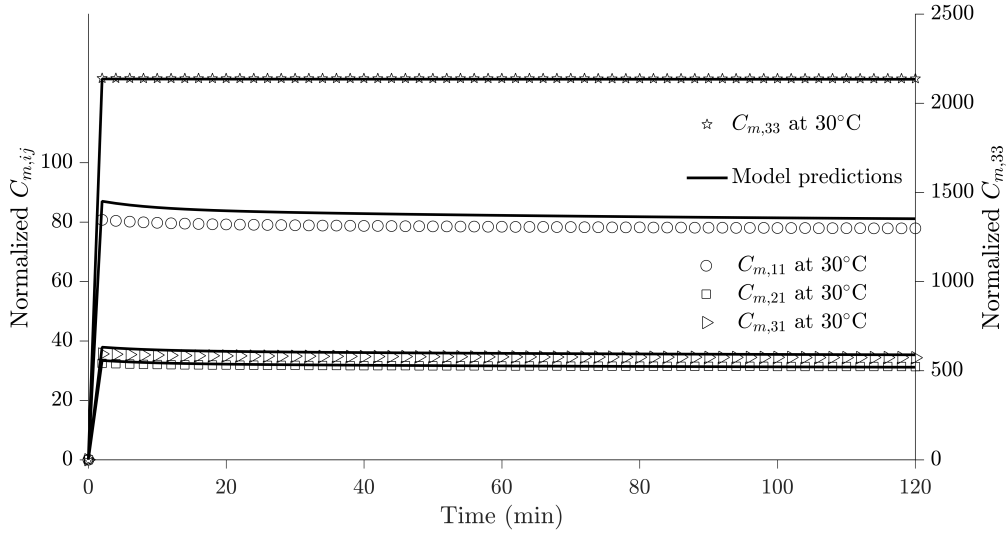
Figure 5.9 Normalized $C_{m,ij}$, $i,j = \{1,2,3\}$, at 30°C, for $\alpha = 1$: simulations results are presented against the model predictions for the warp tows

the weft tows obtained following the same methodology. Figures 5.8 and 5.9 show some discrepancies between the simulations and the model predictions, probably due to the fact that an idealized hexagonal packing was used. Indeed, the maximal scatter is 6% between the predictions and the simulations and a maximal deviation of 2% from a transversely isotropic behavior was already noticed in Section 5.5.3. A similar discrepancy was observed by Berger *et al.* (2006).

Table 5.4 Normalized identified parameters for the warp tows

	$K_{1,ij}$	$K_{2,ij}$	H_{ij}	β_{ij}	$log\tau_{\mathbf{peak},ij}$	$l_{\mathbf{peak},ij}$
$p_{m,11}C_{m,11}^{(k)}$	-0.76	1.83	175	0.049	0.16	0.88
$p_{m,11}C_{m,33}^{(k)}$	-0.76	1.83	40	0.049	0.16	0.88
$p_{m,11}C_{m,31}^{(k)}$	-0.76	1.83	78	0.049	0.16	0.88
$p_{m,44}C_{m,44}^{(k)}$	-3.05	6.20	50	0.077	-0.22	1.03
$p_{m,11}C_{m,66}^{(k)}$	-0.76	1.83	74	0.053	0.28	0.82

Table 5.5 Normalized identified parameters for the weft tows

	$K_{1,ij}$	$K_{2,ij}$	H_{ij}	β_{ij}	$log\tau_{\mathbf{peak},ij}$	$l_{\mathbf{peak},ij}$
$p_{m,11}C_{m,11}^{(k)}$	-0.84	1.89	172	0.060	0.011	0.94
$p_{m,11}C_{m,33}^{(k)}$	-0.84	1.89	35	0.060	0.011	0.94
$p_{m,11}C_{m,31}^{(k)}$	-0.84	1.89	77	0.060	0.011	0.94
$p_{m,44}C_{m,44}^{(k)}$	-2.66	5.27	48	0.083	-0.28	1.05
$p_{m,11}C_{m,66}^{(k)}$	-0.84	1.89	70	0.058	0.066	0.92

5.6 Mesoscale model: effective 3D interlock woven composite RVE properties

5.6.1 Representative volume element

The 3D interlock woven RVE architecture was an idealized Abaqus mesh of 23.44 mm $\times$ 16.96 mm $\times$ 3.37 mm constructed with WiseTex (Verpoest et Lomov, 2005). Figure 5.10 shows the voxelized RVE after compaction for a $V_f = 51\%$. Local orientation axes were attributed to each element to account for the weaviness. The mesh was composed of 1,056,000 eight-node brick elements. Figure 5.11 shows a mesh convergence study performed on the RVE. Relative error, err_M, between the elastic stress σ_1 resulting from a unit strain application in the longitudinal direction for different numbers of elements, $N_{elements}$, and the finest mesh stress response is plotted, as well as the total CPU time. Resin and fibers elastic properties (see Section 5.5.1) were used as resin and tows properties for the convergence study (the resin being around 80 times more compliant than the fibers). The mesh used in this work is indicated by a dashed line. Figure 5.11 suggests that the chosen mesh is not fully converged. This mesh was adopted as a compromise between accuracy and available computational resources.

5.6.2 Assumptions

The temperature dependence for the mesoscale RVE was assumed to be the same as that of the neat resin because the tows Arrhenius parameters were already the same as that of the
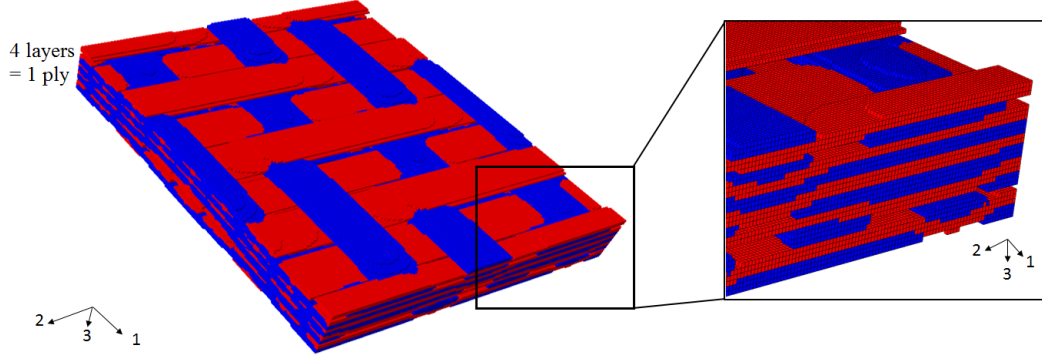
Figure 5.10 3D interlock woven reinforcement voxelized RVE after compaction to a V_f of 51% (warp tows in blue, weft tows in red)
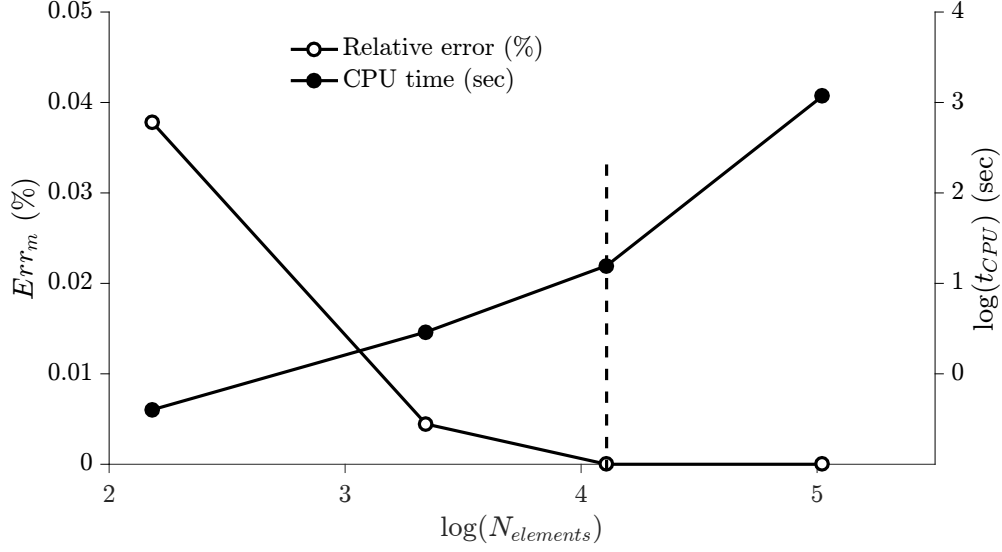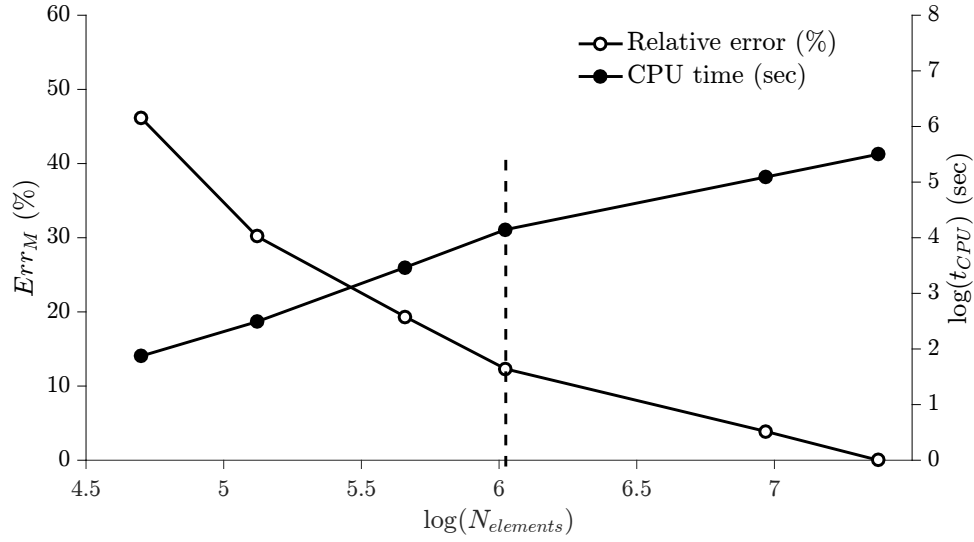

Figure 5.11 Mesh convergence study for the mesoscopic RVE. Relative error (%), between the elastic stress σ_1 resulting from a unit strain application in the longitudinal direction and the finest mesh stress response, and total CPU time (sec) are plotted as a function of the number of elements $N_{elements}$. The chosen mesh is emphasized by a dashed line

neat resin (see Section 5.5.3). The Arrhenius and DiBenedetto equations parameters were then set equal to the values in Table 5.1.

5.6.3 Finite Element simulations and parameters identification

The warp and weft tows mechanical properties, identified in Section 5.5, were added into the `UMAT` subroutine with the resin properties as well. MUBC were applied and 90 minutes isothermal relaxation tests were simulated at 30°C. Figure 5.12 details the applied boundary conditions. As the temperature-dependence was already determined, simulations at different

temperatures were not required, except for the relaxed tensor $\mathbf{C}_{M,\infty}$: its components were independently set to the last values ($t = 90$ minutes) of the corresponding relaxation curves for the fully cured composite loaded at $150°C$ to reduce the number of parameters. The parameters $K_{1,ij}$, $K_{2,ij}$, H_{ij}, β_{ij}, $l_{\text{peak},ij}$, $\log \tau_{\text{peak},ij}$ (Equation 5.2, Table 5.3) remained to be determined for each component.

	Xmin	Xmax	Ymin	Ymax	Zmin	Zmax
Tensile 1	$u_1 = 0$	$u_1 = L_1$	$u_2 = 0$	$u_2 = 0$	$u_3 = 0$	$u_3 = 0$
Tensile 2	$u_1 = 0$	$u_1 = 0$	$u_2 = 0$	$u_2 = L_2$	$u_3 = 0$	$u_3 = 0$
Tensile 3	$u_1 = 0$	$u_1 = 0$	$u_2 = 0$	$u_2 = 0$	$u_3 = 0$	$u_3 = L_3$
Shear 12	$u_2 = -\frac{L_1}{4}$ $u_3 = 0$	$u_2 = \frac{L_1}{4}$ $u_3 = 0$	$u_1 = -\frac{L_2}{4}$ $u_3 = 0$	$u_1 = \frac{L_2}{4}$ $u_3 = 0$	$u_3 = 0$	$u_3 = 0$
Shear 13	$u_3 = -\frac{L_1}{4}$ $u_2 = 0$	$u_3 = \frac{L_1}{4}$ $u_2 = 0$	$u_2 = 0$	$u_2 = 0$	$u_1 = -\frac{L_3}{4}$ $u_2 = 0$	$u_1 = \frac{L_3}{4}$ $u_2 = 0$
Shear 23	$u_1 = 0$	$u_1 = 0$	$u_3 = -\frac{L_2}{4}$ $u_1 = 0$	$u_3 = \frac{L_2}{4}$ $u_1 = 0$	$u_2 = -\frac{L_3}{4}$ $u_1 = 0$	$u_2 = \frac{L_3}{4}$ $u_1 = 0$
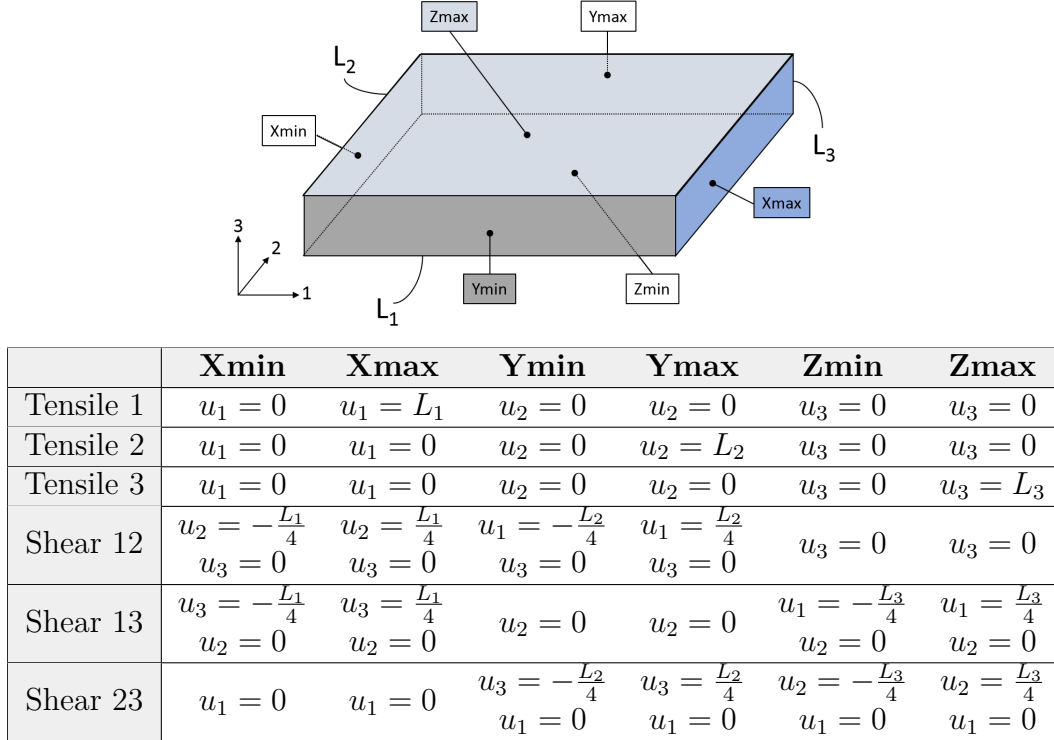
Figure 5.12 Mixed boundary conditions applied on the voxelized RVE for the mesoscale homogenization. u_i denote displacements and L_i the volume element edges lengths along the direction i

The resulting stiffness matrix, $\mathbf{C}_M$ (M for mesoscopic sacle), at any t, showed an orthotropic behavior. For example, at $t = 1$ min (normalized):

$$\mathbf{C}_M(t = 1) = \begin{bmatrix} 976.2 & 38.7 & 43 & 0 & 0 & 0 \\ 38.7 & 425 & 32.3 & 0 & 0 & 0 \\ 43 & 32.3 & 73.9 & 0 & 0 & 0 \\ 0 & 0 & 0 & 36.4 & 0 & 0 \\ 0 & 0 & 0 & 0 & 52.5 & 0 \\ 0 & 0 & 0 & 0 & 0 & 65.1 \end{bmatrix} \tag{5.38}$$

Therefore, the nine independent components were identified from

$$\mathbf{E}_M^{(k)} = \mathbf{p}_M(\alpha) \odot \mathbf{C}_M^{(k)} =$$

$$\begin{bmatrix} p_{M,11}C_{M,11}^{(k)} & p_{M,21}C_{M,21}^{(k)} & p_{M,31}C_{M,31}^{(k)} & 0 & 0 & 0 \\ p_{M,21}C_{M,21}^{(k)} & p_{M,22}C_{M,22}^{(k)} & p_{M,32}C_{M,32}^{(k)} & 0 & 0 & 0 \\ p_{M,31}C_{M,31}^{(k)} & p_{M,32}C_{M,32}^{(k)} & p_{M,33}C_{M,33}^{(k)} & 0 & 0 & 0 \\ 0 & 0 & 0 & p_{M,44}C_{M,44}^{(k)} & 0 & 0 \\ 0 & 0 & 0 & 0 & p_{M,55}C_{M,55}^{(k)} & 0 \\ 0 & 0 & 0 & 0 & 0 & p_{M,66}C_{M,66}^{(k)} \end{bmatrix} \tag{5.39}$$

where $p_{M,ij} = K_{1,ij}\alpha + K_{2,ij}, \; \forall i,j$.

The three components associated with the shear properties were first determined independently by minimizing the cost function (Equation 5.36) for each shear components, with the conditions $C_{M,ii}^{(k)} > 0$ and $p_{M,ii} > 0$, $i = \{4,5,6\}$. The optimized parameters are listed in Table 5.6 and Figure 5.13 shows the simulated shear components with their corresponding predicted evolution for $\alpha = 1$ at $30°$C.

$E_{M,ij}^{(k)}$, $i,j = \{1,2,3\}$, were then determined by minimizing the cost function (Equation 5.37), with the condition that the eigenvalues of $\mathbf{E}_M^{(k)}$ were positive to ensure the positiveness of $\mathbf{E}_M^{(k)}$. The optimized parameters are listed in Table 5.6 and Figures 5.13 and 5.14 show the simulated components with their corresponding predicted evolution for $\alpha = 1$ at $30°$C. The model predictions were in good agreement with the simulated results for all the components, even if almost no viscoelasticity appeared for the three first diagonal components.

Nine spectra (Table 5.6) were thus determined to model the RVE temperature- and cure-dependent linearly viscoelastic behavior. Figure 5.15 shows the six spectra related to the diagonal components. The higher are the composite properties, the higher are the spectra. Indeed, the highest relaxation modulus was obtained in the warp direction (1) and the $E_{M,11}^{(k)}$ is the highest curve.

5.7 Comparison with experimental data

5.7.1 Specimens manufacturing

One-ply rectangular composite plates of $280mm \times 139mm$ were manufactured by RTM and a fiber volume fraction of 51% was targeted. Figure 5.16 shows the process set-up used. 3D interlock woven fabric plies were cut along three directions: warp tows oriented at $45°$ from the longitudinal future plate direction and weft and warp tows respectively oriented along the
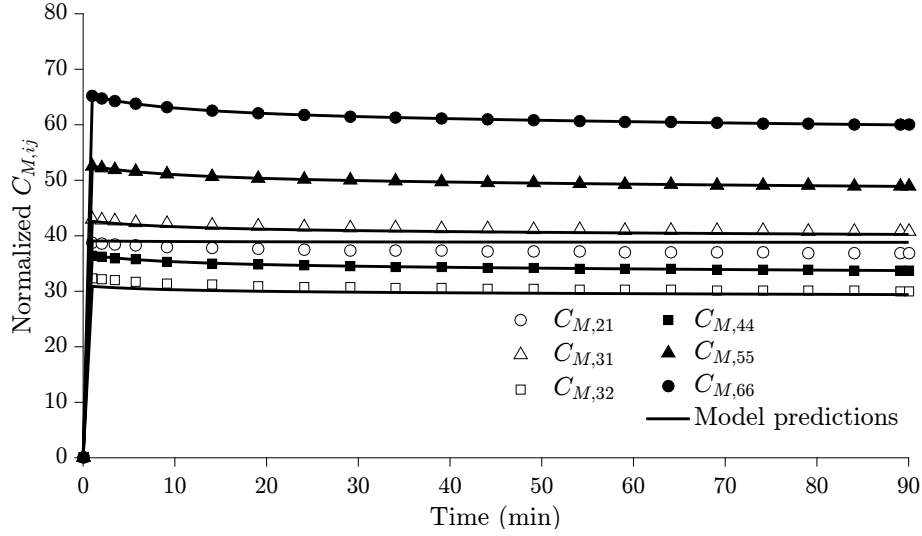
Figure 5.13 Normalized $C_{M,ij}$, $i,j = \{1,2,3,4,5,6\}$ components evolution at 30°C for $\alpha = 1$: simulations results are presented against the model predictions
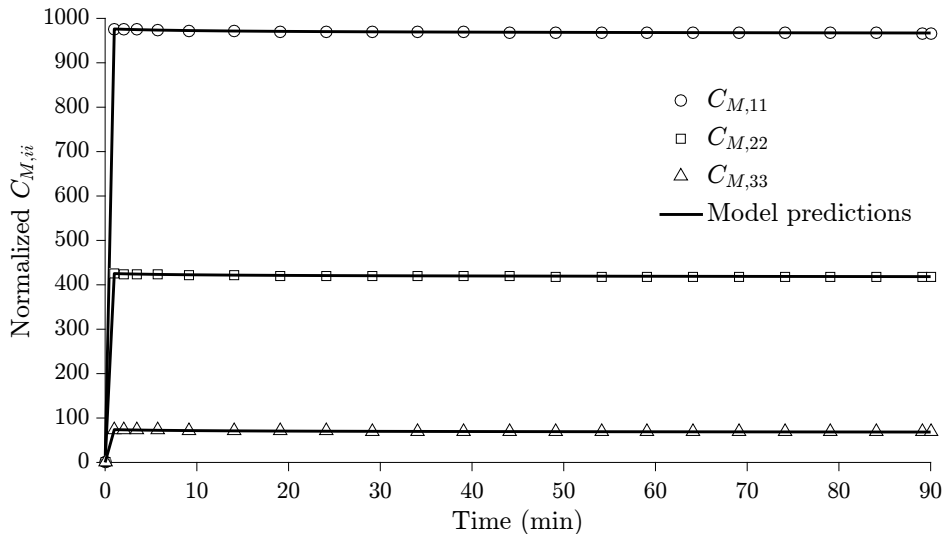
Figure 5.14 Normalized $C_{M,ii}$, $i = \{1,2,3\}$ components evolution at 30°C for $\alpha = 1$: simulations results for $C_{M,11}$, $C_{M,22}$ and $C_{M,33}$ are presented against the model predictions

longitudinal future plate direction. Figure 5.17 schematized the studied configurations. Two plates were manufactured with warp tows oriented at 45°, three with warp tows oriented along the longitudinal plate direction and three with weft tows oriented along the longitudinal plate direction. Thermocouples were installed on the steel mold cavity surfaces before placing a reinforcement ply. The epoxy resin was preheated at 100°C and degassed during 30 minutes. The resin was then injected into the heated mold at a constant flow rate of 20 ml/min. A compaction pressure was applied right after and during the whole process to prevent porosities in the final part. After longitudinal injection, the mold was submitted to two

Table 5.6 Normalized identified parameters for the composite

	$K_{1,ij}$	$K_{2,ij}$	H_{ij}	β_{ij}	$log\tau_{peak_{ij}}$	$l_{peak_{ij}}$
$E_{M,11}^{(k)}$	-0.45	2.63	900	0.027	0.83	2.4
$E_{M,22}^{(k)}$	-0.88	3.6	400	0.05	1.16	2.54
$E_{M,33}^{(k)}$	-3.49	7.63	70	0.15	0.94	2.26
$E_{M,44}^{(k)}$	-1.66	3.51	74	0.15	0.93	2.14
$E_{M,55}^{(k)}$	-2.74	5.97	74	0.17	1.38	2.63
$E_{M,66}^{(k)}$	-3.13	6.31	74	0.17	0.94	2.05
$E_{M,12}^{(k)}$	-0.7	0.99	38	0.72	0.22	3.15
$E_{M,13}^{(k)}$	-1.14	2.69	43	0.06	1.48	1.03
$E_{M,23}^{(k)}$	-4.32	9	30.50	0.18	0.76	2.75
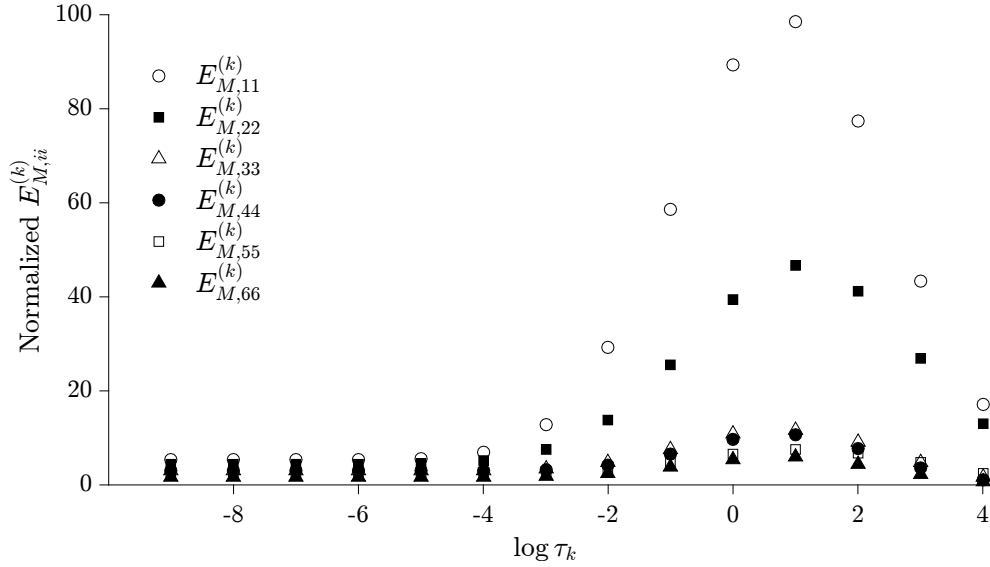
Figure 5.15 Normalized $E_{M,ii}^{(k)}$, $i = \{1, 2, 3, 4, 5, 6\}$ components as a function of the relaxation times for $\alpha = 1$ and $T_{\mathrm{ref}} = T_g$

temperature steps to ensure the resin's complete curing. The parts were cooled down in the closed mold until the internal temperature reached 100°C. Finally, the plates were ejected and cooled down by air convection at room temperature. Four specimens of 250 mm × 25 mm × 3.35 mm were then water jet cut in each of the manufactured composite plates. The average fiber volume fraction for each specimen was 51% as expected, except for the warp oriented samples which reached 54% due to thickness variability. The fiber volume fractions were calculated from the mass and volume of the composite specimens and the constituents densities.
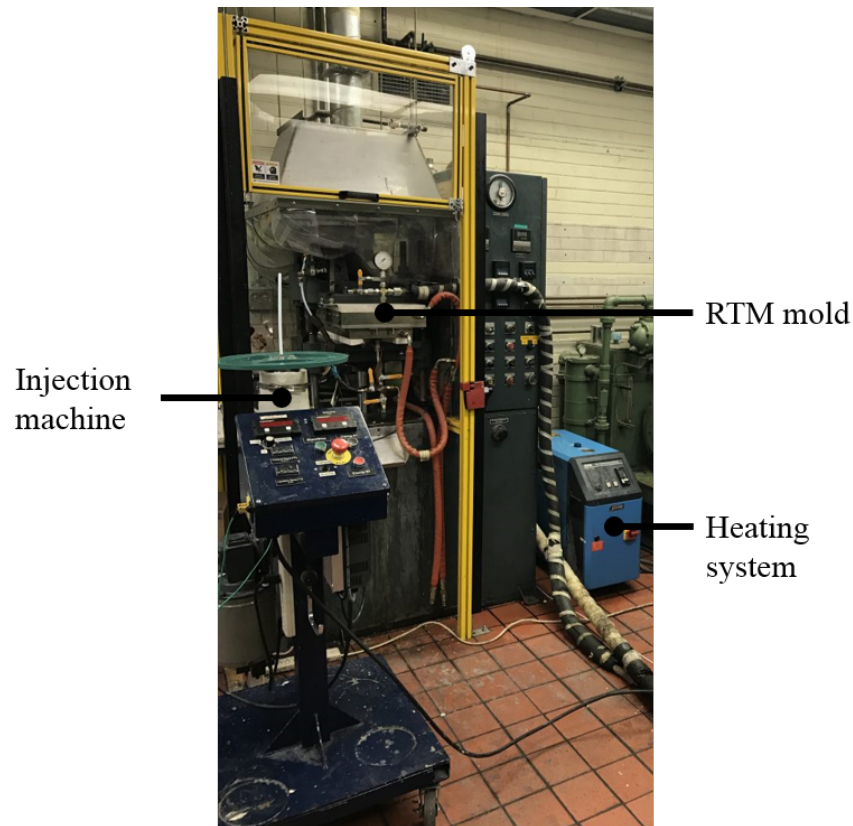
Figure 5.16 Experimental set-up to manufacture composite specimens by RTM: an RTM mold with an injection machine and an oil heating system
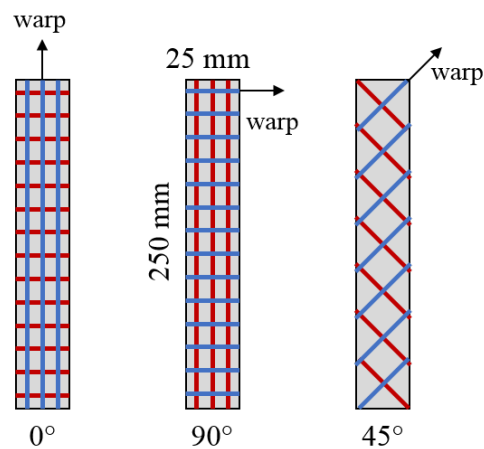
Figure 5.17 Schematics of the three studied configurations: from left to right, warp oriented specimens, weft oriented specimens and 45° oriented specimens

5.7.2 Thermo-mechanical testing in the linearly viscoelastic domain

The linearly viscoelastic domain was first investigated for the wrap and weft oriented configurations at 140°C. Isothermal creep tests were performed on two different weft oriented

samples for stress levels of $\sigma = 40$ MPa and $\sigma = 40 \times 2.225 = 89$ MPa, respectively. An Insight testing machine using a tension fixture, coupled with an oven, was used to perform the tests. A biaxial extensometer from Epsilon Technology Corporation (model 3560) was installed on the specimen to measure the strain evolution in longitudinal and transversal directions. Thermocouples were also put onto the samples to record the specimens' temperature evolution. Figure 5.18 shows the experimental set-up. The response of the first specimen was multiplied by 2.225 and compared to the response of the second specimen. Figure 5.19 plots the two specimens responses. The figure shows that the two responses were similar and we assumed that composites lied in the linearly viscoelastic range for stresses lower than 89 MPa. The results were assumed to be valid for the warp oriented specimens as well and for tests at 120°C, as mechanical properties are higher in that configuration and temperature. Isothermal creep tests were then performed on two to three samples in each of these two configurations at 120°C and 140°C and for stress levels of $\sigma = 40$ MPa and $\sigma = 46$ MPa. The specimens were heated for two hours, free of loading, to ensure the apparatus and specimen thermal equilibrium.

Isothermal creep tests were also carried out on 45° oriented specimens at 140°C for stress levels of $\sigma = 8$ MPa and $\sigma = 8 \times 1.25 = 10$ MPa. Figure 5.20 shows that no linearity was observed between the corresponding strain responses. The curves would have been similar if this range of stresses was in the viscoelastic linear domain. No further investigation on the linearly viscoelastic domain for the 45° oriented specimens was done due to the restricted number of specimens. Few tests were still performed for very small stress levels of $\sigma = 2.9$ MPa and $\sigma = 3.9$ MPa at 140°C. Table 5.7 lists the performed creep experiments.

Table 5.7 Summary of the creep tests performed on composite plates

Specimens	Temperature (°C)	Applied stress (MPa)
warp-plate1-sp1	120	40
warp-plate1-sp2	120	40
warp-plate2-sp1	120	40
warp-plate2-sp2	140	46.2
warp-plate2-sp4	140	46.5
weft-plate2-sp2	120	40
weft-plate2-sp4	120	40
weft-plate3-sp1	120	40
weft-plate3-sp2	140	40
weft-plate2-sp3	140	40
45-plate1-sp1	140	2.9
45-plate2-sp2	140	3.9
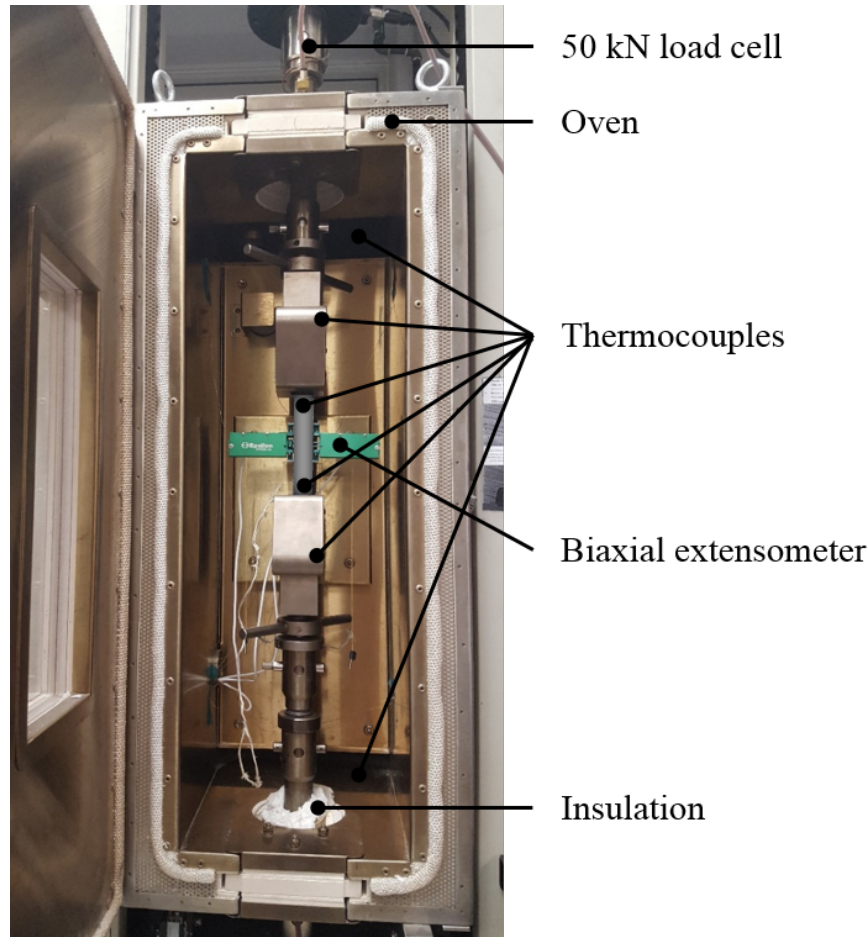
Figure 5.18 Experimental set-up to perform isothermal creep tests on composite specimens: an Insight machine with a 50 kN load cell coupled to an oven, thermocouples and extensometer to record the temperature and strain evolution respectively

5.7.3 Results and model predictions comparison

Figures 5.21 to 5.25 compare the experimental isothermal creep responses and the model predictions for the three studied configurations, at 120°C and/or 140°C. The heating phase was not considered as several phenomena simultaneously occurred (thermal expansion of the apparatus, of the extensometer and of the composite specimens). The recovery was not studied either as occurring at the same time as the cooling, making the measurements unreliable for the same reason as for the heating phase. Figures 5.21 and 5.22 show minor overestimations of around 10% for the model predictions at 120°C and 140°C for warp oriented specimens. A reasonable correlation was observed between the model predictions and the experimental data on weft oriented specimens at 120°C, as presented in Figure 5.23. The maximum relative difference was 3.6%. However, the model could not reproduce the experimental values at 140°C for the same configuration (see Figure 5.24). Finally, Figure 5.25 shows the compari-
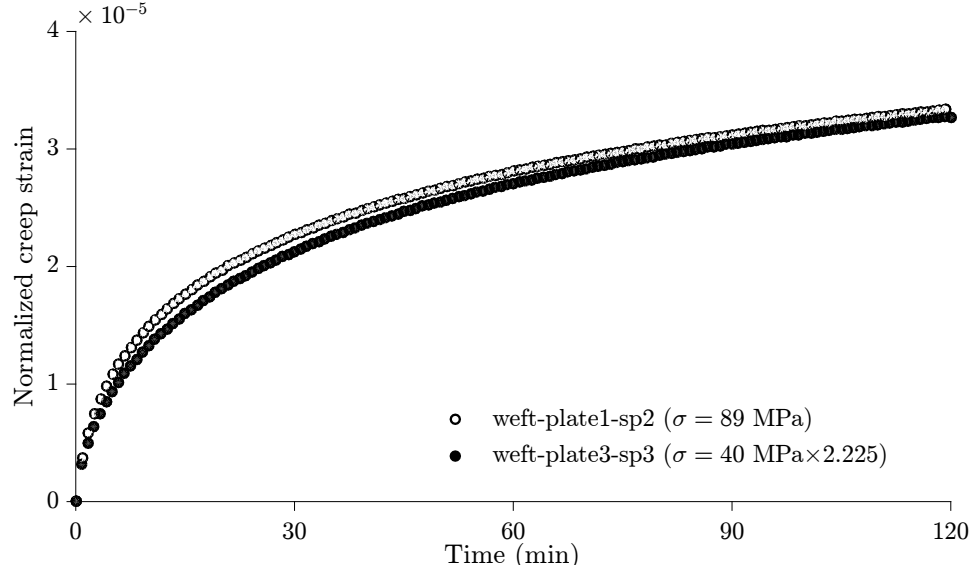
Figure 5.19 Determination of the linear viscoelastic range: axial creep experiments at 140°C at two stress levels on two different weft oriented specimens, respectively. The two responses are similar, the studied composite lied in the linearly viscoelastic range for stresses lower than 89 MPa for the warp and weft directions
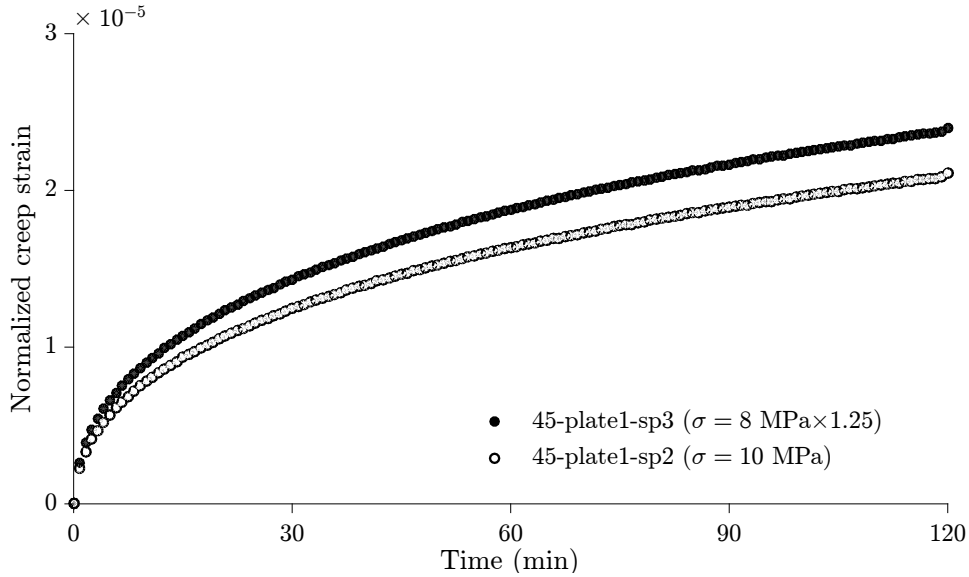
Figure 5.20 Determination of the linear viscoelastic range: creep experiments at 140°C at two stress levels on two different 45° oriented specimens, respectively. The curve are not similar. The viscoelastic linear domain is exceeded

son between the experimental creep responses of 45° oriented specimens at 140°C for stress levels of $\sigma = 2.9$ MPa and $\sigma = 3.9$ MPa. The maximum discrepancies were 3% and 15%, respectively.
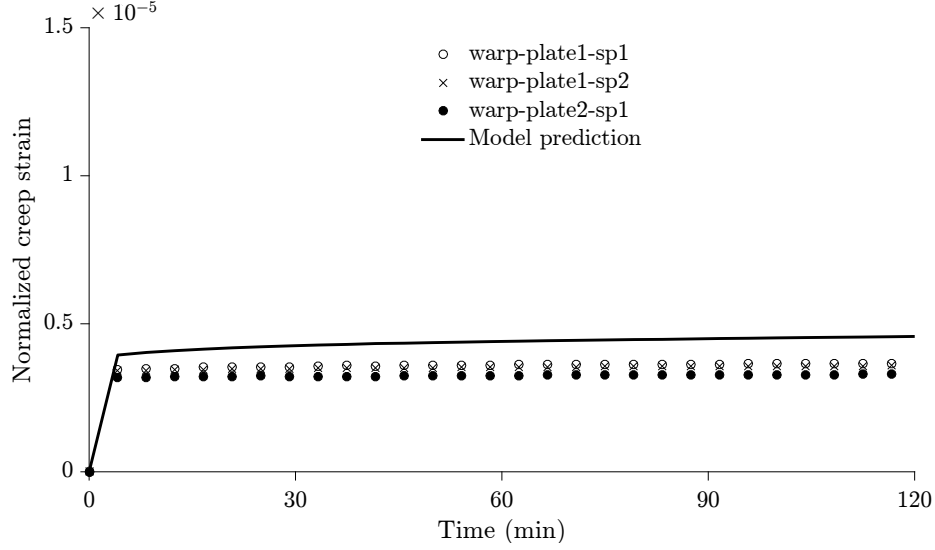
Figure 5.21 Comparison between the model predictions and experimental results of axial creep tests carried out on wrap oriented specimens at 120°C for a stress level of $\sigma = 40$ MPa. A slight overestimation is observed, probably due to the idealized fiber volume fractions used in the model
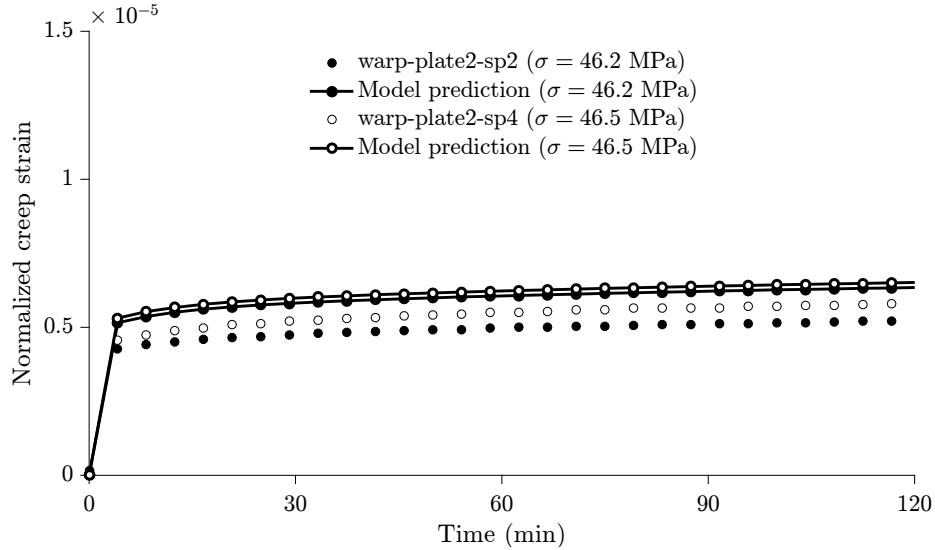
Figure 5.22 Comparison between the model predictions and experimental results of axial creep tests carried out on warp oriented specimens at 140°C for stress levels of $\sigma = 46.2$ MPa and $\sigma = 46.5$ MPa. A slight overestimation is observed, probably due to the idealized fiber volume fractions used in the model

5.7.4   Discussion

The homogenization method was performed using an idealized RVE with a fiber volume fraction of 51%. The slight overestimation of the model for the warp oriented specimens could be justified by the fact that their effective fiber volume fractions were closer to 54% in
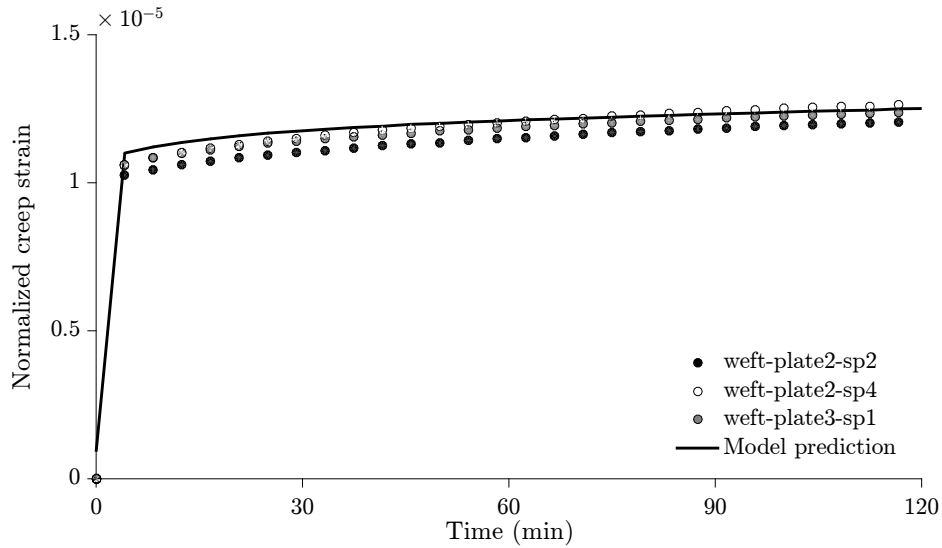
Figure 5.23 Comparison between the model predictions and experimental results of axial creep tests carried out on weft oriented specimens at 120°C for a stress level of $\sigma = 40$ MPa. The predictions are in good agreement with the experimental data
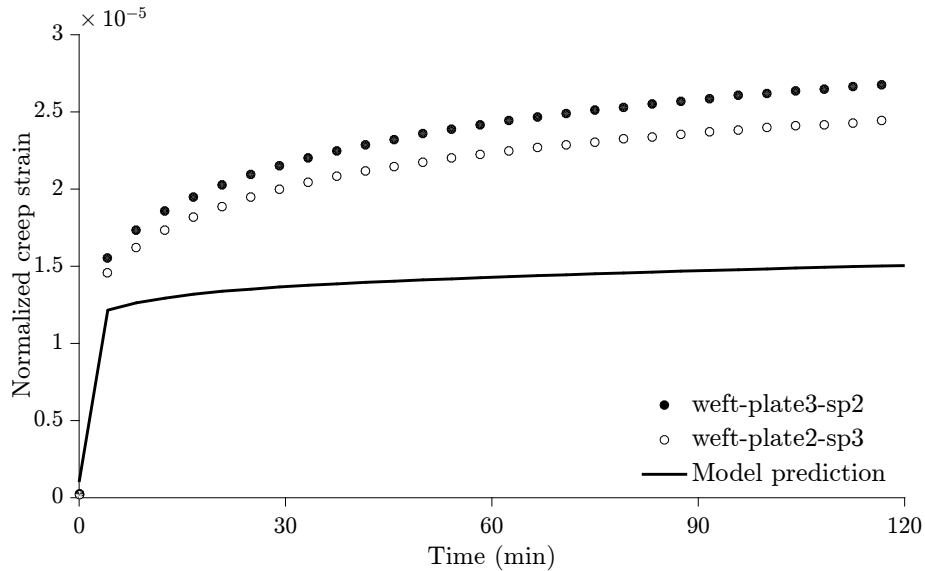
Figure 5.24 Comparison between the model predictions and experimental results of creep tests carried out on weft oriented specimens at 140°C for a stress level of $\sigma = 40$ MPa. The model could not predict the composite behavior in the weft direction at 140°C

that configuration (see Section 5.7.1), suggesting better mechanical properties and a smaller effect of the resin viscoelastic behavior. Therefore, the specimens showed smaller creep. The model predictions for the 45° oriented samples were accurate for a stress level of $\sigma = 2.9$ MPa but underestimated the creep response for a stress level of $\sigma = 3.9$ MPa. The linear domain ascertainment was not conclusive on the 45° oriented composite specimens (see section 5.7.2) and its limit was probably reached. The linear domain was assumed for applied stresses lower
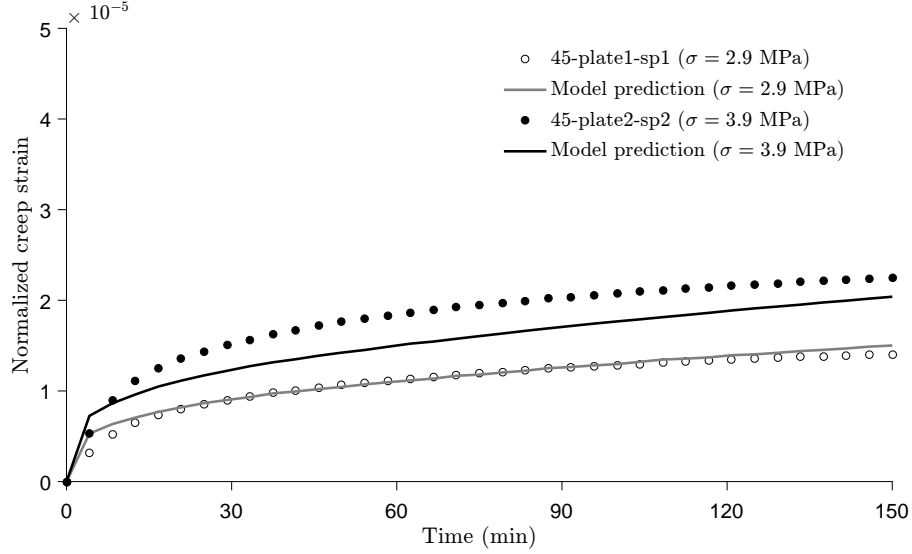
Figure 5.25 Comparison between the model predictions and experimental results of axial creep tests carried out on 45° oriented specimens at 140°C for stress levels of $\sigma = 2.9$ MPa and $\sigma = 3.9$ MPa. The predictions are in very good agreement with the experimental data for a stress level of $\sigma = 2.9$ MPa but less for a stress level of $\sigma = 3.9$ MPa

than 3.9 MPa, based on previous work (Courtois *et al.*, 2018). However, it was ascertained by three-point-bending tests using a DMA in Courtois *et al.* (2018) and could therefore differ. The model predicted reasonably well the strain responses of the weft oriented specimens heated at 120°C. However, the discrepancies observed at 140°C could be related to the mesh coarseness. Indeed, discrepancies around 10% were observed on elastic properties from a finer mesh through the convergence study detailed in Section 5.6.1 and the elastic properties decreased when increasing the number of elements. It could also be related to the glass transition. Indeed, the model was developed and validated for temperatures below the glass transition temperature of the neat resin (Courtois *et al.*, 2018) and 140°C is already close to this limit. Moreover, the assumed T_g was determined by Differential Scanning Calorimetry (DSC) on neat resin. Other means of characterization of T_g should be explored.

Moreover, surface tows misalignment were observed on the specimens and could have affected the material behavior, especially for an only four layers reinforcement, as that studied. Then, the use of an idealized RVE could have induced discrepancies with the experimental data. Indeed, it does not take into account the observed misalignment. Moreover, the fiber volume fraction of warp and weft tows could be slightly different from the idealized RVE to the effective values.

5.8 Conclusion

A temperature- and cure-dependent viscoelastic model previously developed for a neat epoxy resin was extended to a 3D interlock woven composite material by numerical FE multiscale homogenization in the time domain. The homogenized model was successfully validated on experimental composite's creep responses. Its temperature-dependent predictions have shown a good agreement with experimental data in the composite's linear domain below the glass transition temperature. The composite temperature-dependence was the same as that of the resin and an orthotropic degree of cure-dependence was identified. Simulations on an idealized RVE with periodic boundary conditions and a finer mesh could probably reduce the observed small discrepancies. Numerical predictions could also be improved by using RVEs from tomography in order to take into account the exact fiber volume fraction of the parts and tows and the real textile configuration. More creep tests could also be performed to widen the experimental validation dataset.

5.9 Acknowledgements

CHAPTER 6   GENERAL DISCUSSION

6.1   Matrix mechanical properties

6.1.1   Characterization

Multi-temperature tests implication

Multi-temperature relaxation tests were performed using a three point bending fixture in a DMA Q800 from TA Instruments. The specimens were successively tested every 15°C at temperatures ranging from 30°C to the samples glass transition temperature. A ten minutes recovery was allowed between each relaxation phase. Fully cured specimens were tested at 30°C, 45°C, 60°C, 75°C, 90°C, 105°C, 120°C, 135°C and 150°C, successively.

Supplementary tests were performed at 120°C on a fully cured specimen with no load or temperature history to study the effect of load and temperature history on the specimens' relaxation responses. Figure 6.1 shows the stress evolution at 120°C for a 180-minute relaxation test for $\varepsilon = 0.1\%$, for two fully cured specimens: specimen A, which experienced the multi-temperature test, and specimen B, with no prior load or temperature history. The results are normalized by the measured stress at the beginning of relaxation, on fully cured samples at 30°C, for confidentiality reasons (as in Chapter 4). A difference of around 7% was observed between the two samples responses at the beginning of relaxation. After 30 minutes, the two specimen responses were very similar. Therefore, the load and temperature history experienced by the multi-temperature tested specimens did not have a significant influence on the long-term relaxation responses.

Characterization above the glass transition temperature

This work focused on the mechanical behavior below the glass transition temperature. As the glass transition temperature is usually exceeded during the manufacturing process, characterization above would be recommended to extend the model to this wider range of temperatures. The resin state changes through T_g and another behavior could be identified above T_g. Additional relaxation tests were performed on fully cured specimens above their glass transition temperature using the same configuration as the tests below the glass transition temperature. However, the results were not reliable. Negative stress values for a strain level of $\varepsilon = 0.1\%$ were recorded during 90-minute experiments on five different fully cured specimens at 165°C, as shown in Figure 6.2. These results could be explained by the fact that
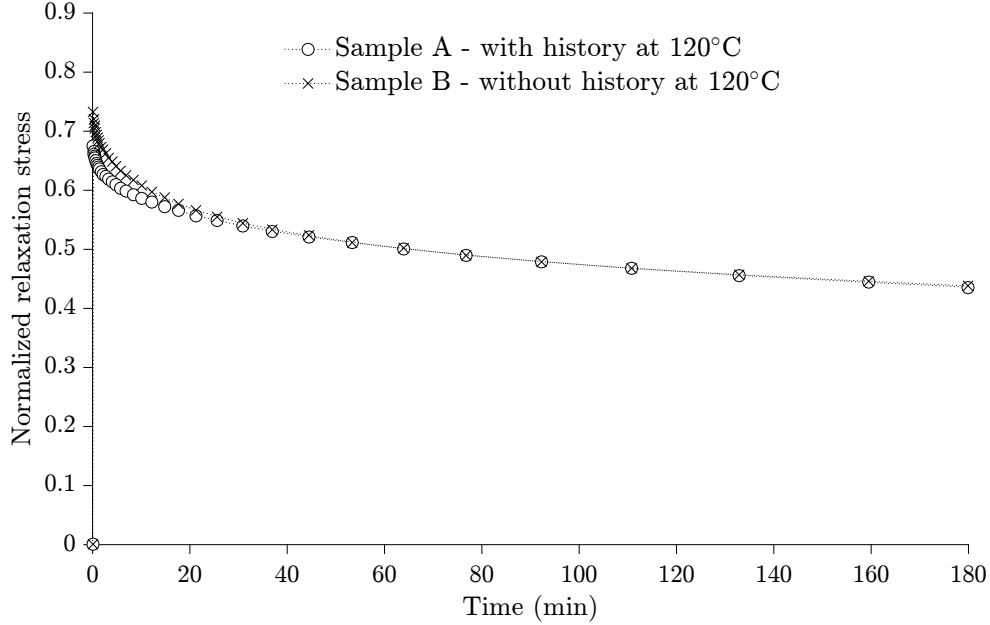
Figure 6.1 Normalized stress responses to a strain level of $\varepsilon = 0.1\%$ during 180 minutes at 120°C, for two fully cured specimens: specimen A with load and temperature histories and specimen B without history. Discrepancies are observed at the beginning of the test but both responses converged after 40 minutes

the three point bending DMA test set-up was not adapted to measure the stress response near the glass transition temperature for the studied epoxy resin. Four fully cured specimens were subsequently tested at 180°C for a strain level of $\varepsilon = 0.1\%$. Figure 6.3 shows that the relaxation results are more repeatable at 180°C than at 165°C. However, the figure suggests that the stress increases in the early stages of the process. Although the reasons for this behavior are unknown at this stage, an equipment misreading could be the cause. The results are normalized by the measured stress at the beginning of relaxation, on fully cured samples at 30°C, for confidentiality reasons (as in Chapter 4).

6.1.2 Modeling

Epoxy resins are widely used in structural components and their viscoelastic behavior was studied by several authors (Kim et White, 1996; Simon *et al.*, 2000; O'Brien *et al.*, 2001; Saseendran *et al.*, 2016, 2017b). O'Brien *et al.* (2001) predicted the cure- and temperature-dependent viscoelastic behavior of an epoxy resin below, near and its the glass transition temperature through a unique model. Saseendran et al., however, distinguished the behavior below and above the glass transition temperature.

This thesis was focused on the behavior below the glass transition temperature. A linearly
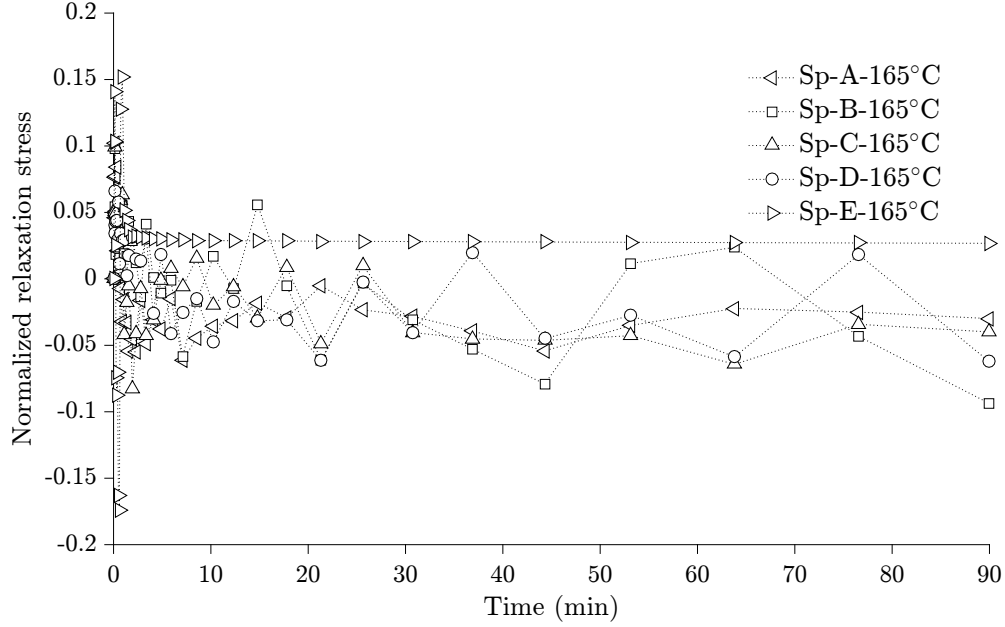
Figure 6.2 Normalized stress responses to a strain level of $\varepsilon = 0.1\%$ during 90 minutes at 165°C, for five fully cured specimens. The relaxation response exhibits significant scatter, which renders its analysis impossible
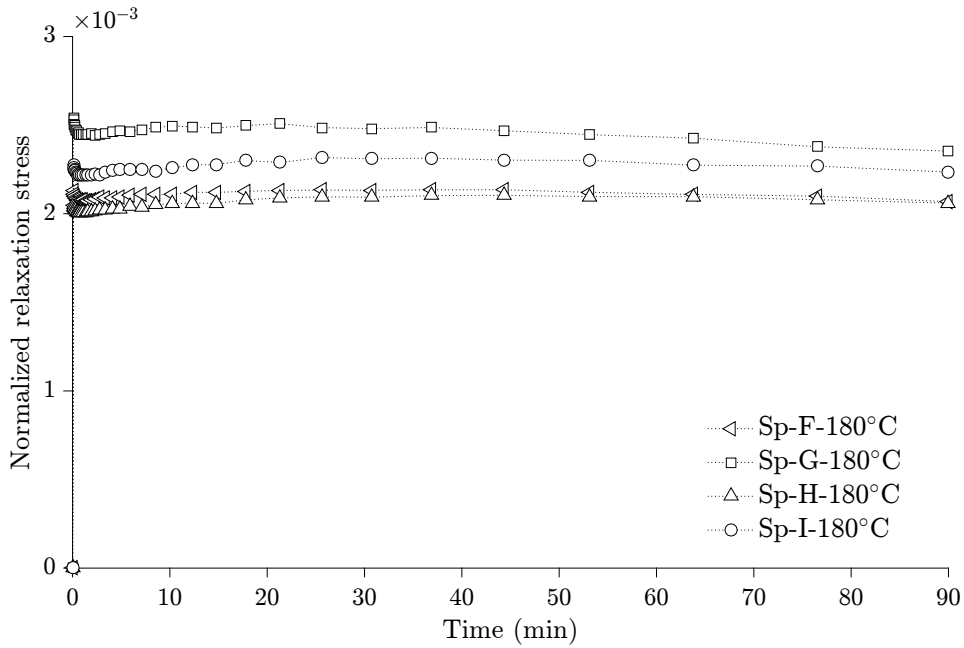
Figure 6.3 Normalized stress responses to a strain level of $\varepsilon = 0.1\%$ during 90 minutes at 180°C, for four fully cured specimens. The figure shows that stresses increase during the relaxation

viscoelastic behavior was assumed and validated for the studied strain range. Moreover, the model relied on the Thermodynamics of irreversible processes approach to ensure a thermo-

dynamically admissible model with an easily implementable formulation. The temperature- and cure-dependences were added through the shift factors using the Arrhenius relationship, with the glass transition temperature as the reference temperature, and the DiBenedetto relationship related the degree of cure and the T_g. The degree of cure was also added through the activation energy in the Arrhenius equation, as a cure dependence was observed on the relaxation mechanisms. Moreover, the degree of cure seemed to influence the instantaneous elastic stiffness of the studied epoxy resin in a counterintuitive tendency: the resin's instantaneous elastic stiffness increased when the degree of cure decreased. No physical or chemical explanation could be drawn at this stage but Chapter 4 showed that the tendency was statistically significant. This behavior was taken into account through the parameter $p(\alpha)$. Figures 6.4 and 6.5 compare the actual developed viscoelastic model predictions and model predictions without the factor $p(\alpha)$ against the experimental relaxation data obtained in Chapter 4 for the neat resin, for $\alpha = 1$ and $\alpha = 0.74$, respectively. The values are normalized by the measured stress at the beginning of relaxation, on fully cured samples at 30°C, for confidentiality reasons (as in the Chapter 4). Figure 6.4 shows that the predictions accounting for $p(\alpha)$ and without $p(\alpha)$ are both in the experimental relaxation data range. However, the relevance of using $p(\alpha)$ is clearly noticeable in Figure 6.5. This parameter allows the model to accurately predict the resin behavior at 30°C and 45°C for $\alpha = 0.74$.
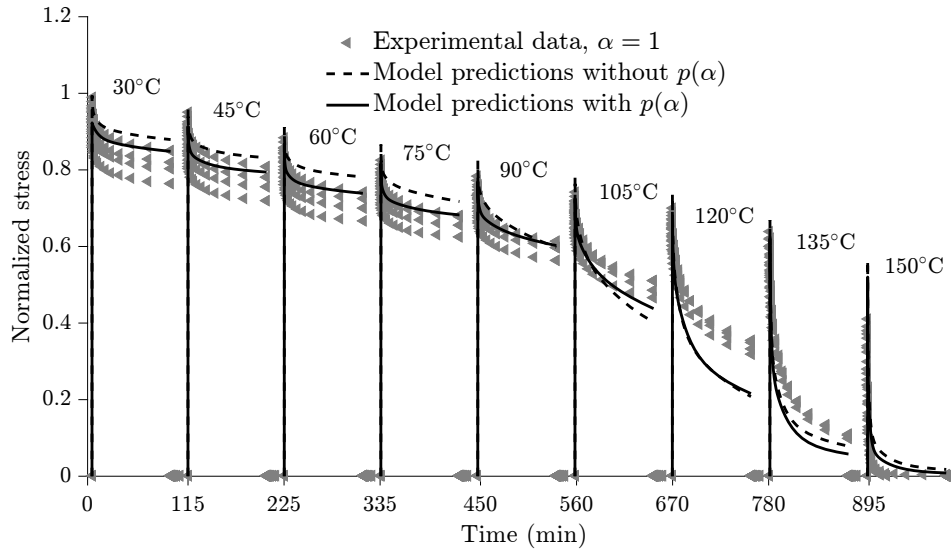
Figure 6.4 Normalized experimental relaxation data for $\alpha = 1$ against model predictions accounting for, or not, $p(\alpha)$. Both model predictions are closed to the experimental data

Recent studies have shown that epoxy resins presented a time-, temperature- and cure-dependent Poisson's ratio (Saseendran *et al.*, 2017a). However, during this work, the Poisson's ratio was assumed to be constant with time, temperature and degree of cure because model
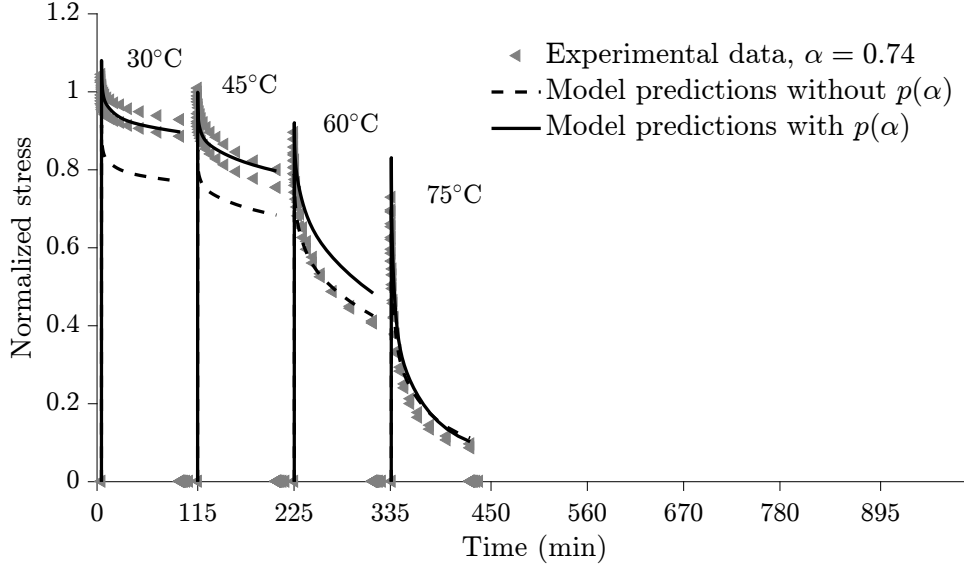
Figure 6.5 Normalized experimental relaxation data for $\alpha = 0.74$ against model predictions accounting for, or not, $p(\alpha)$. Only the model accounting for $p(\alpha)$ accurately predicted the resin's behavior at 30°C and 45°C

predictions accuracy considering a temperature and/or DoC-dependent viscoelastic Poisson's ratio was not demonstrated in the literature. The results revealed that the model was in agreement with the experimental data on neat resin and was successfully validated on an independent creep data set.

6.2 Homogenization

6.2.1 Computational time

The homogenization approach used in this thesis relies on 252 simulations: 228 for the microscale homogenization and 24 for the mesoscale homogenization. Table 6.1 details the simulations and their computing time. The microscale homogenization includes 19 simulations of 100 minutes for different degrees of cure and temperatures, for six different unit loads, for the warp and weft tows. Since the temperature-dependence for the tows was identified to be the same as that of the neat resin, the temperature-dependence for the composite was assumed to be the same as well. Fewer mesoscale simulations were therefore required. The model was not identified a second time for a higher V_f to compare the predictions with the warp tows because a change in the mesoscale V_f implies a change in the microscopic scale V_f. Therefore, both warp and weft tows would have been computed again and the mesoscopic homogenization performed too. The computation time required was thus a liability.

Table 6.1 Number of simulations with their computational time required to identify the homogenized viscoelastic model developed in this thesis

	Simulations	Computational time	Data retrieval
warp tows[1]	114	1 h 40 min each	1 min
weft tows[1]	114	1 h 40 min each	1 min
mesoscale RVE[2]	24	6 h each	120 min
TOTAL	**252**	**906 h**	3336 min = **56 h**

[1] *Computed on a dual-core computer with 16 Go RAM, allocating 1 CPU*
[2] *Computed on a 64 CPU server with 1.5 TB RAM, allocating 10 CPU*

6.2.2 Mesoscale computations

Eight-node brick elements with reduced integration (C3D8R) were used for the mesoscale homogenization for their computational efficiency. A comparison with fully integrated eight-node elements (C3D8) was performed to ensure the results validity of using C3D8R elements. Figure 6.6 shows the stress responses to unit loads $\varepsilon_2 = 1$, $\varepsilon_i = 0$ for $i \neq 2$ and $\varepsilon_5 = 1$, $\varepsilon_i = 0$ for $i \neq 5$, using C3D8R and C3D8 elements. The results are normalized by the same arbitrary value as in Chapter 5. 90-minute relaxation tests were computed at 30°C for $\alpha = 1$. The maximum relative difference was 1.4%. Since the temperature affects the material behavior, comparison between the stress responses to a unit load $\varepsilon_1 = 1$, $\varepsilon_i = 0$ for $i \neq 1$, using C3D8R and C3D8 elements was also done at 30°C and 120°C for $\alpha = 1$. The stress responses are plotted in Figure 6.7. The maximum relative error was 0.8% at 30°C and 2.7% at 120°C.

Simulation with C3D8R elements yielded stiffer responses than those using fully integrated elements, in each studied case. This could be explained by the fact that Abaqus automatically stiffens the material if elements with reduced integration are chosen. The difference between results from fully integrated elements and reduced integrated elements computations were however deemed negligible, while computations with C3D8 elements required 21 hours, i.e. 3.5 more time than those with C3D8R elements. The choice of reduced integration elements could also explain some discrepancies between the model predictions and experimental creep data (cf. Chapter 5).

6.3 Composite mechanical properties characterization

Creep tests were performed on composite specimens at 120°C and 140°C in Chapter 5. A biaxial extensometer was installed on the specimens to measure the strain evolution in longitudinal and transverse directions. The measurements in the longitudinal direction were dealt in Chapter 5 to validate the developed model against experimental creep data.
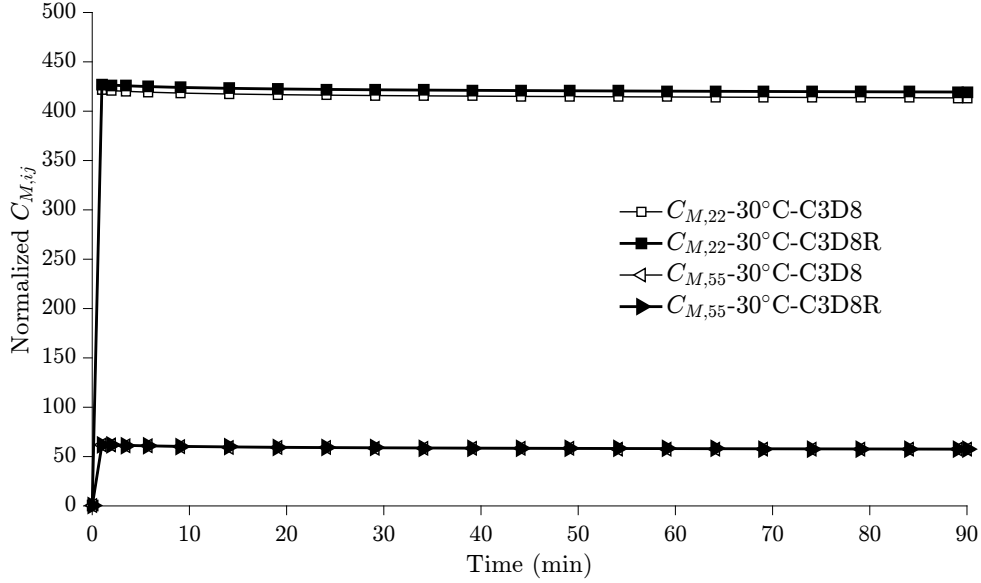
Figure 6.6 Normalized stress responses to unit loads $\varepsilon_2 = 1$, $\varepsilon_i = 0$ for $i \neq 2$ and $\varepsilon_5 = 1$, $\varepsilon_i = 0$ for $i \neq 5$, during 90 minutes at 30°C, for $\alpha = 1$. Computations results using fully integrated elements (C3D8) and elements with reduced integration (C3D8R) are quite similar
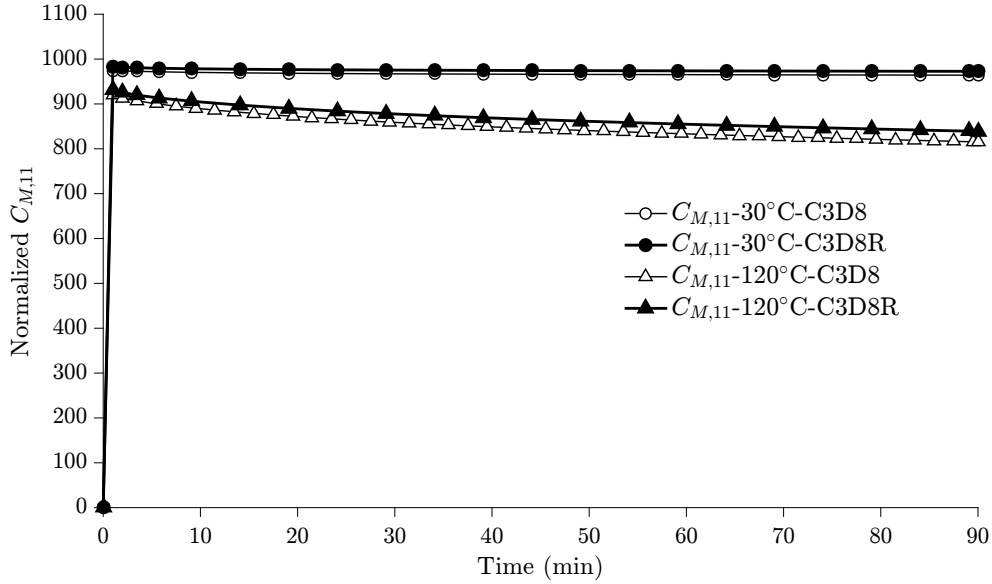
Figure 6.7 Normalized stress responses to a unit load $\varepsilon_1 = 1$, $\varepsilon_i = 0$ for $i \neq 1$, during 90 minutes at 30°C and 120°C, for $\alpha = 1$. Computations results using fully integrated elements (C3D8) and elements with reduced integration (C3D8R) are similar. The difference increases with temperatures

Extensometer longitudinal displacement acquisition was validated at room temperature through monotonic tensile tests on warp and weft specimens. Displacement ramps of 1 mm/min were applied onto a warp and a weft oriented specimens. The elastic moduli in warp and weft

directions were computed and compared to analytical values. Relative difference between the experimental and the analytical values was 0.3% and 2% respectively. The longitudinal displacement acquisition was therefore assumed reliable.

The extensometer transverse displacement acquisition was investigated on a known aluminum specimen. Monotonic tensile tests were performed at room temperature. The Poisson's ratio, as the ratio of transverse strain to axial strain during a tensile test where the force is applied, was computed and its values varied from 0.33 to 0.44. Therefore, the transversal measurements of the extensometer was not deemed reliable and was not studied in this work.

CHAPTER 7   CONCLUSION AND RECOMMENDATIONS

A multiscale temperature- and degree of cure-dependent linearly viscoelastic model was developed and experimentally validated to predict the behavior of a 3D interlock woven composite.

The first step was to characterize the epoxy resin temperature- and DoC-dependent viscoelastic behavior. Partially and fully cured specimens were manufactured and tested with a three point bending clamp in a DMA Q800 from TA Instruments. Relaxation tests were performed at several temperatures, successively, ranging from room temperature to the specimens glass transition temperature. The glass transition temperature was never exceeded for the partially cured samples to prevent further polymerization. Relaxation data was therefore acquired for different degrees of cure and temperatures. The relaxation results revealed that the instantaneous elastic stiffness increased with decreasing degree of cure. This unexpected tendency was statistically investigated and deemed significant.

The second step was to develop a thermodynamically consistent viscoelastic model based on the experimental data previously acquired. The thermodynamics of irreversible processes approach was chosen to ensure the respect of thermodynamics and to obtain an easily implementable formulation. The Time-Temperature Superposition Principle (TTSP) was applied and master curves were constructed to study the temperature dependence. Horizontal shift factors were computed and compared as a function of temperature and degree of cure. An Arrhenius law was identified with the glass transition temperature as the reference temperature. The DiBenedetto equation was used to model the DoC-dependent T_g. The relaxation tensors were associated with the relaxation times through a continuous spectra equation and an additional DoC-dependent parameter $p(\alpha)$ was multiplied to the relaxation tensors to account for the instantaneous elastic stiffness DoC-dependence. A total of ten parameters were defined, including three for the shift factors. The developed model was successfully validated by comparing the model predictions against independent experimental creep data on fully cured specimens below their glass transition temperature. The proposed linearly viscoelastic model is thus thermodynamically consistent and able to predict the resin's relaxation and creep behaviors, as a function of temperature and degree of cure, below the resin's glass transition temperature.

The third step was to compute the homogenized temperature- and degree of cure-dependent mechanical properties for a 3D interlock woven composite. The warp and weft tows mechanical properties were computed from an idealized hexagonal packing converged RVE in Abaqus. Periodic boundary conditions were applied and the responses to unitary loads were

computed to obtain the full warp and weft tows' stiffness tensors for different temperatures and degrees of cure. 19 simulations have been done for six unit loads for the warp and weft tows, leading to 228 simulations. The ten viscoelastic model parameters were identified to fit the simulation results, assuming a transverse isotropic behavior. Small discrepancies were observed between the simulations and the model predictions as the hexagonal fibers arrangement RVE behavior slightly differs from the transversely isotropy. The degree of cure-dependence was adapted to differ accordingly to the stiffness components, if necessary, and the temperature-dependence appeared to be the same as that of the neat resin. The resulting transversely isotropic viscoelastic model for the warp and weft tows was then used for the mesoscale homogenization, as well as the resin's behavior. Unitary loads were applied on an idealized voxelized RVE with mixed uniform boundary conditions to compute the full composite's stiffness tensor. The composite's temperature dependence was assumed to be the same as that of the neat resin since the tows' temperature-dependence was the same as that of the resin. 18 simulations of 6 h were performed using eight-node brick elements with reduced integration. The three shift factors parameters were set to the resin's model values and seven parameters remained to be identified in order to fit the simulation results. A good correlation was observed between the simulated stiffness tensor components and the model predictions after identification. An orthotropic degree of cure-dependence was identified. The respect of the thermodynamics principles was a major concern for the parameters identification for either the tows or composite behavior.

The final step was to compare the homogenized model predictions against experimental temperature-dependent viscoelastic responses of composite specimens. Three configurations were studied: warp, weft and 45° oriented specimens were manufactured by RTM. Creep tests at 120°C and 140°C were then performed for each configuration. The model slightly overestimated the warp oriented specimens responses at 120°C and 140°C, probably due to the discrepancies in fiber volume fractions. The model predicted accurately the weft oriented specimens behavior at 120°C but failed to reproduce the experimental values at 140°C. It could be explained by the mesh coarseness and the use of idealized RVEs. As for the 45° oriented specimens, their creep responses at 140°C were accurately predicted for stress levels in their linear viscoelastic domain. The homogenized viscoelastic model was therefore successfully validated on composite specimens at high temperatures.

The proposed linearly viscoelastic model has been implemented by another Ph.D. student into a numerical tool to predict the residual stress development during 3D composites manufacturing. The model succeeded to predict the viscoelastic behavior during the post-curing (Benavente Miana, 2017).

In conclusion, the overall methodology to compute composite homogenized properties from resin's behavior experimental results was performed. This study showed that the viscoelastic properties of composites reinforced with 3D interlock woven fabric were temperature- and DoC-dependent below the glass transition temperature. The composite's temperature-dependence was the same as that of the resin and the composite DoC-dependence was orthotropic.

Limitations and recommendations for future work

The developed model was limited below the glass transition temperature, assuming a constant Poisson's ratio and adiabatic conditions.

- **Extend the model to temperature near and above the glass transition temperature**
  The developed temperature- and degree of cure- dependent viscoelastic model was identified on experimental data acquired below the glass transition temperature and validated for the same temperature range. It would be of interest to extend the model to temperatures above the glass transition temperature as the material experiences temperatures higher than T_g during their manufacturing. The three point bending fixture in a DMA showed its limits to temperatures near and above the glass transition temperature. Thus, another characterization methodology has to be investigated. Tension tests using an universal tensile machine or rheological tests with a rheometer could be performed.

- **Investigate the degree of cure influence on the instantaneous elastic stiffness.**
  A counterintuitive tendency relating the instantaneous elastic stiffness and the degree of cure was observed and proved statistically for the studied epoxy resin. It would be interesting to investigate further this behavior. Other characterization techniques could be used to determine if this tendency stems from the three point bending relaxation test or the material itself.

- **Investigate the Poisson's ratio evolution relevance**
  The Poisson's ratio was assumed constant in this study. It would be of interest to determine the Poisson's ratio impact on the viscoelastic material response and if its viscoelasticity, temperature- and/or cure-dependences should be investigated.

- **Investigate other numerical implementation techniques**
  A first-order backward Euler scheme was used to implement the proposed linearly

viscoelastic model. Considering the computation time discussed in Chapter 6, it would be interesting to use higher-order schemes, such as Crank-Nicholson or Runge-Kutta to reduce the computation time.

- **Compute homogenization procedures with more accurate microscale and mesoscale RVEs**

  The multiscale homogenization approaches were performed on idealized RVEs for the microscopic and mesoscopic scales. Discrepancies between the microscopic homogenized model and simulations were observed due to the hexagonal packing assumption. Microscopic RVEs considering randomly distributed fibers or constructed from microtomography could improve the first parameters identification. For the mesoscale, a good correlation was observed between model predictions and experimental data on composite specimens, except at 140°C for the weft oriented specimens. This could be related to several aspects: the use of a non converged mesh and an idealized RVE. It would be of interest to compute the homogenized composite properties from a converged mesh based on tomographic scans, which would account for surface defects and effective fiber volume fractions, and to investigate the relevance of the applied boundary conditions.

- **Carry out a more extensive experimental campaign on composite specimens**

  Few creep tests on fully cured composite specimens have been performed during this thesis. It would be interesting to widen the experimental dataset on composite specimens at high temperatures to gain more confidence in the results and reduce the experimental scatter. Moreover, experiments on partially cured composite samples could validate the homogenized model's cure-dependence.

REFERENCES

Adolf, Douglas and Chambers, Robert (1997). Verification of the capability for quantitative stress prediction during epoxy cure. Polymer, *38*(21), 5481–5490.

Adolf, Douglas B and Chambers, Robert S (2007). A thermodynamically consistent, nonlinear viscoelastic approach for modeling thermosets during cure. Journal of Rheology, *51*(1), 23–50.

Adolf, Douglas B and Chambers, Robert S and Caruthers, James M (2004). Extensive validation of a thermodynamically consistent, nonlinear viscoelastic model for glassy polymers. Polymer, *45*(13), 4599–4621.

Ansar, Mahmood and Xinwei, Wang and Chouwei, Zhou (2011). Modeling strategies of 3d woven composites: a review. Composite structures, *93*(8), 1947–1963.

Barbero, Ever J (2013). Finite element analysis of composite materials using AbaqusTM. CRC press.

Barello, Romina B and Lévesque, Martin (2008). Comparison between the relaxation spectra obtained from homogenization models and finite elements simulation for the same composite. International Journal of Solids and structures, *45*(3-4), 850–867.

Bayraktar, Harun and Tsukrov, Igor and Giovinazzo, Michael and Goering, Jon and Gross, Todd and Fruscello, Monica and Martinsson, Lars (2012). Predicting cure-induced microcracking in 3d woven composites with realistic simulation technology. Proceedings of Society for the Advancement of Material and Process Engineering (SAMPE) Conference.

Benavente, Maria and Marcin, Lionel and Courtois, Alice and Lévesque, Martin and Ruiz, Edu (2018). Numerical analysis of viscoelastic process-induced residual distortions during manufacturing and post-curing. Composites Part A: Applied Science and Manufacturing.

Benavente, M and Marcin, L and Godon, T and Courtois, A and Lévesque, M and Ruiz, E (2017). Numerical analysis of process-induced residual distortions in asymmetric plates : Fe implementation of different constitutive laws. Journal of Composite Materials, submitted.

Benavente Miana, Maria (2017). Viscoelastic Distortion During Manufacturing and Post-Curing of Thermoset Composites: Characterization and Modeling. Thèse de doctorat, École Polytechnique de Montréal.

Berger, H and Kari, S and Gabbert, U and Rodriguez-Ramos, R and Bravo-Castillero, J and Guinovart-Diaz, R and Sabina, FJ and Maugin, GA (2006). Unit cell models of piezoelectric fiber composites for numerical and analytical calculation of effective properties. Smart Materials and Structures, *15*(2), 451.

Billotte, C and Bernard, FM and Ruiz, Edu (2013). Chemical shrinkage and thermomechanical characterization of an epoxy resin during cure by a novel in situ measurement method. European Polymer Journal, *49*(11), 3548–3560.

Biot, MA (1954). Theory of stress-strain relations in anisotropic viscoelasticity and relaxation phenomena. Journal of Applied Physics, *25*(11), 1385–1391.

Blanc, V and Barbie, L and Largeiiton, R and Masson, R (2011). Homogenization of linear viscoelastic three phase media: Internal variable formulation versus full-field computation. Procedia Engineering, *10*, 1889–1894.

Bogetti, Travis A and Gillespie, John W (1992). Process-induced stress and deformation in thick-section thermoset composite laminates. Journal of Composite Materials, *26*(5), 626–660.

Bornert, Michel and Bretheau, Thierry and Gilormini, Pierre (2001a). Homogénéisation en mécanique des matériaux, Tome 1: Matériaux aléatoires élastiques et milieux périodiques. Hermes science.

Bornert, Michel and Bretheau, Thierry and Gilormini, Pierre (2001b). Homogénéisation en mécanique des matériaux, tome 2: Comportements non linéaires et problèmes ouverts.

Brauner, Christian and Frerich, Tim and Herrmann, Axel S (2017). Cure-dependent thermomechanical modelling of the stress relaxation behaviour of composite materials during manufacturing. Journal of Composite Materials, *51*(7), 877–898.

Brinson, LC and Knauss, WG (1992). Finite element analysis of multiphase viscoelastic solids. Journal of Applied Mechanics, *59*(4), 730–737.

Brinson, LC and Lin, WS (1998). Comparison of micromechanics methods for effective properties of multiphase viscoelastic composites. Composite Structures, *41*(3-4), 353–367.

Cai, Yongming and Sun, Huiyu (2014). Dynamic response of thermo-viscoelasticity of three-dimensionally braided composites. Journal of Composite Materials, *48*(13), 1575–1583.

Caruthers, James M and Adolf, Douglas B and Chambers, Robert S and Shrikhande, Prashant (2004). A thermodynamically consistent, nonlinear viscoelastic approach for modeling glassy polymers. Polymer, *45*(13), 4577–4597.

Chaboche, Jean-Louis (1997). Thermodynamic formulation of constitutive equations and application to the viscoplasticity and viscoelasticity of metals and polymers. International Journal of Solids and Structures, *34*(18), 2239–2254.

Chamis, Christos C (1989). Mechanics of composite materials: past, present and future. Journal of composites technology & research, *11*(1), 3–14.

Charmetant, Adrien and Orliac, Jean-Guillaume and Vidal-Sallé, Emmanuelle and Boisse, Philippe (2012). Hyperelastic model for large deformation analyses of 3d interlock composite preforms. Composites Science and Technology, *72*(12), 1352–1360.

Charron, Morgan (2017). Modélisation basée images du comportement thermomécanique de composite C/C. Thèse de doctorat, Bordeaux.

Choi, Sukjoo and Sankar, Bhavani V (2006). Micromechanical analysis of composite laminates at cryogenic temperatures. Journal of composite materials, *40*(12), 1077–1091.

Christensen, RM (1969). Viscoelastic properties of heterogeneous media. Journal of the Mechanics and Physics of Solids, *17*(1), 23–41.

Couégnat, Guillaume (2008). Approche multiéchelle du comportement mécanique de matériaux composites à renfort tissé. Thèse de doctorat, Université Sciences et Technologies-Bordeaux I.

Courtois, Alice and Hirsekorn, Martin and Benavente, Maria and Jaillon, Agathe and Marcin, Lionel and Ruiz, Edu and Lévesque, Martin (2018). Viscoelastic behavior of an epoxy resin during cure below the glass transition temperature: Characterization and modeling. Journal of Composite Materials, accepted.

Cox, Brian N and Dadkhah, Mahyar S and Morris, WL (1996). On the tensile failure of 3d woven composites. Composites Part A: Applied Science and Manufacturing, *27*(6), 447–458.

Crochon, Thibaut (2014). Modeling of the Viscoelastic Behavior of a Polyimide Matrix at elevated Temperature. Thèse de doctorat, Ph. D. thesis, École Polytechnique de Montréal.

Crochon, Thibaut and Schönherr, Tony and Li, Chun and Lévesque, Martin (2010). On finite-element implementation strategies of schapery-type constitutive theories. Mechanics of Time-Dependent Materials, *14*(4), 359–387.

Crowson, Roger J. and Arridge, Robert G.C. (1979). Linear viscoelastic properties of epoxy resin polymers in dilatation and shear in the glass transition region. 1. Time-temperature superposition of creep data. Polymer, *20*(6), 737–746.

Delorme, Rolland and Tabiai, Ilyass and Laberge Lebel, Louis and Levesque, Martin (2017). Generalization of the ordinary state-based peridynamic model for isotropic linear viscoelasticity. Mech Time-Depend Mater, (doi:10.1007/s11043-017-9342-3).

DiBenedetto, AT (1987). Prediction of the glass transition temperature of polymers: a model based on the principle of corresponding states. Journal of Polymer Science Part B: Polymer Physics, *25*(9), 1949–1969.

Ding, Anxin and Li, Shuxin and Sun, Jiuxiao and Wang, Jihui and Zu, Lei (2016). A comparison of process-induced residual stresses and distortions in composite structures with different constitutive laws. Journal of Reinforced Plastics and Composites, *35*(10), 807–823.

Dixit, A and Mali, Harlal Singh (2013). Modeling techniques for predicting the mechanical properties of woven-fabric textile composites: a review. Mechanics of composite Materials, *49*(1), 1–20.

Drouin, Eric (2017). Materials and processes, lighter engines and aircrafts. Website. `https://www.safran.cn/en/materials-and-processes`, Last accessed on 2018-05-16.

Durville, Damien (2009). A finite element approach of the behaviour of woven materials at microscopic scale. Mechanics of microstructured solids, Springer. 39–46.

Durville, Damien (2010). Simulation of the mechanical behaviour of woven fabrics at the scale of fibers. International journal of material forming, *3*(2), 1241–1251.

El Mourid, Amine (2014). Mechanical behavior of a triaxially braided textile composite at high temperature.

El Mourid, Amine and Ganesan, Rajamohan and Lévesque, Martin (2013). Comparison between analytical and numerical predictions for the linearly viscoelastic behavior of textile composites. Mechanics of Materials, *58*, 69–83.

Ersoy, Nuri and Garstka, Tomasz and Potter, Kevin and Wisnom, Michael R and Porter, David and Clegg, Martin and Stringer, Graeme (2010). Development of the properties of a carbon fibre reinforced thermosetting composite through cure. Composites Part A: Applied Science and Manufacturing, *41*(3), 401–409.

Ferry, John D (1980). Viscoelastic properties of polymers. John Wiley & Sons.

Fisher, FT and Brinson, LC (2001). Viscoelastic interphases in polymer–matrix composites: theoretical models and finite-element analysis. Composites Science and technology, *61*(5), 731–748.

Friebel, C and Doghri, I and Legat, V (2006). General mean-field homogenization schemes for viscoelastic composites containing multiple phases of coated inclusions. International journal of solids and structures, *43*(9), 2513–2541.

Ghossein, Elias and Lévesque, Martin (2014). A comprehensive validation of analytical homogenization models: The case of ellipsoidal particles reinforced composites. Mechanics of Materials, *75*, 135–150.

Gommers, Bart and Verpoest, Ignace and Van Houtte, Paul (1998). The mori–tanaka method applied to textile composite materials. Acta Materialia, *46*(6), 2223–2235.

Grail, Gaël (2013). Approche multimodèle pour la conception de structures composites à renfort tissé. Thèse de doctorat, Université d'Orléans.

Green, SD and Matveev, MY and Long, AC and Ivanov, D and Hallett, SR (2014). Mechanical modelling of 3d woven composites considering realistic unit cell geometry. Composite Structures, *118*, 284–293.

Guinovart-Díaz, Raúl and Bravo-Castillero, Julián and Rodríguez-Ramos, Reinaldo and Sabina, Federico J (2001). Closed-form expressions for the effective coefficients of fibre-reinforced composite with transversely isotropic constituents. i: Elastic and hexagonal symmetry. Journal of the Mechanics and Physics of Solids, *49*(7), 1445–1462.

Gusev, Andrei A (2017). Finite element estimates of viscoelastic stiffness of short glass fiber reinforced composites. Composite Structures, *171*, 53–62.

Haj-Ali, Rami M and Muliana, Anastasia H (2004). Numerical finite element formulation of the schapery non-linear viscoelastic material model. International Journal for Numerical Methods in Engineering, *59*(1), 25–45.

Hashin, ZVI (1970). Complex moduli of viscoelastic composites—i. general theory and application to particulate composites. International Journal of Solids and Structures, *6*(5), 539–552.

Hassanzadeh, Hassan and Pooladi-Darvish, Mehran (2007). Comparison of different numerical laplace inversion methods for engineering applications. Applied mathematics and computation, *189*(2), 1966–1981.

Hazanov, Sergej and Huet, Christian (1994). Order relationships for boundary conditions effect in heterogeneous bodies smaller than the representative volume. Journal of the Mechanics and Physics of Solids, *42*(12), 1995–2011.

Hill, R1 (1965). A self-consistent mechanics of composite materials. Journal of the Mechanics and Physics of Solids, *13*(4), 213–222.

Hivet, Gilles and Boisse, Philippe (2005). Consistent 3d geometrical model of fabric elementary cell. application to a meshing preprocessor for 3d finite element analysis. Finite Elements in Analysis and Design, *42*(1), 25–49.

Hojjati, Mehdi and Johnston, Andrew and Hoa, Suong V and Denault, Johanne (2004). Viscoelastic behavior of cytec fm73 adhesive during cure. Journal of applied polymer science, *91*(4), 2548–2557.

Huang, Tao and Gong, Yaohua (2018). A multiscale analysis for predicting the elastic properties of 3d woven composites containing void defects. Composite Structures, *185*, 401–410.

Hwang, SJ and Gibson, RF and Singh, J (1992). Decomposition of coupling effects on damping of laminated composites under flexural vibration. Composites Science and Technology, *43*(2), 159–169.

Johnston, Andrew and Vaziri, Reza and Poursartip, Anoush (2001). A plane strain model for process-induced deformation of laminated composite structures. Journal of composite materials, *35*(16), 1435–1469.

Johnston, Andrew A (1997). An integrated model of the development of process-induced deformation in autoclave processing of composite structures. Thèse de doctorat, University of British Columbia.

Julian, François (2013-11-16). Les secrets du leap de cfm international. Website. `https://www.isae-alumni.net/gene/main.php?base=840&id_news=1273`, Last accessed on 2018-05-16.

Kanit, T and Forest, S and Galliet, Ia and Mounoury, Va and Jeulin, D (2003). Determination of the size of the representative volume element for random composites: statistical and numerical approach. International Journal of solids and structures, *40*(13-14), 3647–3679.

Kari, Sreedhar and Berger, Harald and Gabbert, Ulrich and Guinovart-Dıaz, Raul and Bravo-Castillero, Julian and Rodrıguez-Ramos, Reinaldo (2008). Evaluation of influence of interphase material parameters on effective material properties of three phase composites. Composites Science and Technology, *68*(3-4), 684–691.

Khoun, Loleï and Centea, Timotei and Hubert, Pascal (2009). Characterization methodology of thermoset resins for the processing of composite materials-case study: Cycom 890rtm epoxy resin. Journal of Composite Materials.

Khoun, Loleï and de Oliveira, Rui and Michaud, Véronique and Hubert, Pascal (2011). Investigation of process-induced strains development by fibre bragg grating sensors in resin transfer moulded composites. Composites Part A: Applied Science and Manufacturing, *42*(3), 274–282.

Khoun, L and Hubert, P (2007). Processing characterization of a rtm carbon epoxy system for aeronautical applications. CANCOM 2007, Winnipeg. August 2007.

Khoun, Loleï and Hubert, Pascal (2010). Cure shrinkage characterization of an epoxy resin system by two in situ measurement methods. Polymer Composites, *31*(9), 1603–1610.

Kim, Hyung Joo and Swan, Colby C (2003). Voxel-based meshing and unit-cell analysis of textile composites. International Journal for Numerical Methods in Engineering, *56*(7), 977–1006.

Kim, Seung Jo and Ji, Kuk Hyun and Paik, Seung Hoon (2008). Numerical simulation of mechanical behavior of composite structures by supercomputing technology. Advanced Composite Materials, *17*(4), 373–407.

Kim, Yeong K and Daniel, Isaac M (2002). Cure cycle effect on composite structures manufactured by resin transfer molding. Journal of composite materials, *36*(14), 1725–1743.

Kim, Yeong K and White, Scott R (1996). Stress relaxation behavior of 3501-6 epoxy resin during cure. Polymer Engineering & Science, *36*(23), 2852–2862.

Lahellec, Noël and Suquet, Pierre (2007). Effective behavior of linear viscoelastic composites: a time-integration approach. International Journal of Solids and Structures, *44*(2), 507–529.

Lapeyronnie, Patrick and Le Grognec, Philippe and Binétruy, Christophe and Boussu, François (2011). Homogenization of the elastic behavior of a layer-to-layer angle-interlock composite. Composite Structures, *93*(11), 2795–2807.

Lejeunes, Stéphane and Bourgeois, Stéphane (2011). Une toolbox abaqus pour le calcul de propriétés effectives de milieux hétérogènes. 10th Colloque National en calcul des structures.

Lévesque, Martin and Derrien, Katell and Baptiste, Didier and Gilchrist, Michael D (2008). On the development and parameter identification of schapery-type constitutive theories. Mechanics of Time-Dependent Materials, *12*(2), 95–127.

Lévesque, Martin and Derrien, Katell and Mishnaevski Jr, Leon and Baptiste, Didier and Gilchrist, Michael D (2004). A micromechanical model for nonlinear viscoelastic particle reinforced polymeric composite materials—undamaged state. Composites Part A: Applied Science and Manufacturing, *35*(7-8), 905–913.

Lévesque, Martin and Gilchrist, Michael D and Bouleau, Nicolas and Derrien, Katell and Baptiste, Didier (2007). Numerical inversion of the laplace–carson transform applied to homogenization of randomly reinforced linear viscoelastic media. Computational mechanics, *40*(4), 771–789.

Liu, YuJia and Yan, Ying and Yang, Lei and She, Haiqiang and He, Mingze (2012). Prediction on macroscopic elastic properties of interphase-contained long-fiber-reinforced composites and multiple nonlinear regression analysis. Journal of Reinforced Plastics and Composites, *31*(17), 1143–1157.

Lomov, Stepan Vladimirovitch and Huysmans, G and Luo, Yiwen and Parnas, RS and Prodromou, Andreas and Verpoest, Ignace and Phelan, FR (2001). Textile composites: modelling strategies. Composites Part A: applied science and manufacturing, *32*(10), 1379–1394.

Lomov, Stepan Vladimirovitch and Ivanov, DS and Perie, G and Verpoest, Ignace (2008). Modelling 3d fabrics and 3d reinforced composites: challenges and solutions. Conference proceedings: 1st world conference on 3D fabrics. Manchester.

Lomov, Stepan V and Ivanov, Dmitry S and Verpoest, Ignaas and Zako, Masaru and Kurashiki, Tetsusei and Nakai, Hiroaki and Hirosawa, Satoru (2007). Meso-fe modelling of textile composites: Road map, data flow and algorithms. Composites Science and Technology, *67*(9), 1870–1891.

Long, Andrew Craig (2005). Design and manufacture of textile composites. Elsevier.

Luk-Cyr, Jacques and Crochon, Thibaut and Li, Chun and Lévesque, Martin (2013). Interconversion of linearly viscoelastic material functions expressed as prony series: a closure. Mechanics of Time-Dependent Materials, *17*(1), 53–82.

Machado, Martín and Cakmak, Umut D and Kallai, Imre and Major, Zoltan (2016). Thermomechanical viscoelastic analysis of woven-reinforced thermoplastic-matrix composites. Composite Structures, *157*, 256–264.

Madra, Anna and Breitkopf, Piotr and Rassineux, Alain and Trochu, François (2017). Image-based model reconstruction and meshing of woven reinforcements in composites. International Journal for Numerical Methods in Engineering, *112*(9), 1235–1252.

Madra, Anna and El Hajj, Nemr and Benzeggagh, Malk (2014). X-ray microtomography applications for quantitative and qualitative analysis of porosity in woven glass fiber reinforced thermoplastic. Composites Science and Technology, *95*, 50–58.

Mahnken, Rolf (2013). Thermodynamic consistent modeling of polymer curing coupled to visco–elasticity at large strains. International Journal of Solids and Structures, *50*(13), 2003–2021.

Maire, Jean-François (1992). Etudes théorique et expérimentale du comportement de matériaux composites en contraintes planes. Thèse de doctorat, Besançon.

Marcin, Lionel (2010). Modélisation du comportement, de l'endommagement et de la rupture de matériaux composites à renforts tissés pour le dimensionnement robuste de structures. Thèse de doctorat, Université Bordeaux 1.

Marsh, George (2006). Composites get in deep with new-generation engine. Reinforced plastics, *50*(11), 26–29.

Melo, José Daniel D and Radford, Donald W (2003). Viscoelastic characterization of transversely isotropic composite laminae. Journal of composite materials, *37*(2), 129–145.

Meng, Yan and Bernazzani, Paul and O'Connell, Paul A and McKenna, Gregory B and Simon, Sindee L (2009). A new pressurizable dilatometer for measuring the time-dependent bulk modulus and pressure-volume-temperature properties of polymeric materials. Review of Scientific Instruments, *80*(5), 053903.

Misra, Sarthak and Ramesh, K.T. and Okamura, Allison (2008). Modeling of tool-tissue interactions for computer-based surgical simulation: A literature review. *17*, 463.

Miyano, Yasushi and Nakada, Masayuki and Cai, Hongneng (2007). Characterization of time-temperature dependent static and fatigue behavior of unidirectional cfrp. 16th International Conference on Composite Materials, Kyoto, Japan, July 8–13. vol. 13.

Miyano, Yasushi and Nakada, Masayuki and Cai, Hongneng (2008). Formulation of long-term creep and fatigue strengths of polymer composites based on accelerated testing methodology. Journal of composite materials.

Mori, Tanaka and Tanaka, K (1973). Average stress in matrix and average elastic energy of materials with misfitting inclusions. Acta metallurgica, *21*(5), 571–574.

Moulinec, H and Suquet, P (1998). A numerical method for computing the overall response of nonlinear composites with complex microstructure. Computer methods in applied mechanics and engineering, *157*(1-2), 69–94.

Mouritz, AP and Bannister, MK and Falzon, PJ and Leong, KH (1999). Review of applications for advanced three-dimensional fibre textile composites. Composites Part A: applied science and manufacturing, *30*(12), 1445–1461.

Msallem, Y Abou and Jacquemin, F and Boyard, N and Poitou, A and Delaunay, D and Chatel, S (2010). Material characterization and residual stresses simulation during the manufacturing process of epoxy matrix composites. Composites Part A: Applied Science and Manufacturing, *41*(1), 108–115.

Muliana, A and Rajagopal, KR and Tscharnuter, D and Pinter, Gerald (2016). A nonlinear viscoelastic constitutive model for polymeric solids based on multiple natural configuration theory. International Journal of Solids and Structures, *100*, 95–110.

Muliana, Anastasia H and Haj-Ali, Rami (2008). A multi-scale framework for layered composites with thermo-rheologically complex behaviors. International Journal of Solids and Structures, *45*(10), 2937–2963.

Muliana, Anastasia H and Kim, Jeong Sik (2007). A concurrent micromechanical model for predicting nonlinear viscoelastic responses of composites reinforced with solid spherical particles. International Journal of Solids and Structures, *44*(21), 6891–6913.

Nguyen, V-D and Béchet, Eric and Geuzaine, Christophe and Noels, Ludovic (2012). Imposing periodic boundary condition on arbitrary meshes by polynomial interpolation. Computational Materials Science, *55*, 390–406.

Nie, Jingjiang and Xu, Yongdong and Zhang, Litong and Yin, Xiaowei and Cheng, Laifei and Ma, Junqiang (2008). Effect of stitch spacing on mechanical properties of carbon/silicon carbide composites. Composites Science and Technology, *68*(12), 2425–2432.

O'Brien, Daniel J and Mather, Patrick T and White, Scott R (2001). Viscoelastic properties of an epoxy resin during cure. Journal of composite materials, *35*(10), 883–904.

O'Brien, Daniel J and Sottos, NR and White, Scott R (2007). Cure-dependent viscoelastic poisson's ratio of epoxy. Experimental mechanics, *47*(2), 237–249.

Pahr, Dieter H and Böhm, Helmut J (2008). Assessment of mixed uniform boundary conditions for predicting the macroscopic mechanical behavior of composite materials. na.

Pahr, Dieter H and Zysset, Philippe K (2008). Influence of boundary conditions on computed apparent elastic properties of cancellous bone. Biomechanics and modeling in mechanobiology, *7*(6), 463–476.

Palerosi, Antonio Claret and de Almeida, Sergio Frascino Müller (2007). Thermoelastic evaluation of composite laminates using digital imaging processing. Composites Part A: Applied Science and Manufacturing, *38*(11), 2283–2293.

Pathan, MV and Tagarielli, VL and Patsias, S (2017a). Effect of fibre shape and interphase on the anisotropic viscoelastic response of fibre composites. Composite Structures, *162*, 156–163.

Pathan, MV and Tagarielli, VL and Patsias, S (2017b). Numerical predictions of the anisotropic viscoelastic response of uni-directional fibre composites. Composites Part A: Applied Science and Manufacturing, *93*, 18–32.

Perie, G and Lomov, Stepan Vladimirovitch and Verpoest, Ignace and Marsal, D (2009). Meso-scale modelling and homogenisation of interlock reinforced composite. 17th International Conference on Composite Materials (ICCM-17).

Peron, Mael and Sobotka, Vincent and Boyard, Nicolas and Le Corre, Steven (2014). Thermomechanical effects in pvtα measurements. Key Engineering Materials. vol. 611, 1584–1591.

Potluri, P and Hogg, P and Arshad, M and Jetavat, D and Jamshidi, P (2012). Influence of fibre architecture on impact damage tolerance in 3d woven composites. Applied Composite Materials, *19*(5), 799–812.

Prasatya, Patricia and McKenna, Gregory B and Simon, Sindee L (2001). A viscoelastic model for predicting isotropic residual stresses in thermosetting materials: effects of processing parameters. Journal of Composite Materials, *35*(10), 826–848.

Rao, M Venkat and Mahajan, P and Mittal, RK (2008). Effect of architecture on mechanical properties of carbon/carbon composites. Composite Structures, *83*(2), 131–142.

Renaud, Joffrey (2016). Préformage de tissus 3D interlock de carbone pour la fabrication de composites en injection flexible. Thèse de doctorat, Ecole Polytechnique, Montreal (Canada).

Ricaud, Jean-Marc and Masson, Renaud (2009). Effective properties of linear viscoelastic heterogeneous media: Internal variables formulation and extension to ageing behaviours. International Journal of Solids and Structures, *46*(7), 1599–1606.

Robitaille, F and Souter, BJ and Long, AC and Rudd, CD (1998). A geometrical model for textile preforms. Society for the Advancement of Material and Process Engineering. International SAMPE Europe conference. 151–162.

Ropers, Steffen and Kardos, Marton and Osswald, Tim A (2016). A thermo-viscoelastic approach for the characterization and modeling of the bending behavior of thermoplastic composites. Composites Part A: Applied Science and Manufacturing, *90*, 22–32.

Ruiz, Edu and Trochu, Francois (2005a). Comprehensive thermal optimization of liquid composite molding to reduce cycle time and processing stresses. Polymer composites, *26*(2), 209–230.

Ruiz, Edu and Trochu, Francois (2005b). Thermomechanical properties during cure of glass-polyester rtm composites: elastic and viscoelastic modeling. Journal of Composite Materials, *39*(10), 881–916.

Ruiz, Edu and Trochu, F (2006). Multi-criteria thermal optimization in liquid composite molding to reduce processing stresses and cycle time. Composites Part A: Applied Science and Manufacturing, *37*(6), 913–924.

Ruiz, Edu and Trochu, Francois and Gauvin, Raymond (2004). Internal stresses and warpage of thin composite parts manufactured by rtm. Advanced Composites Letters, *13*(1), 49–57.

Sadeghinia, M. and Jansen, K.M.B. and Ernst, L.J. (2012). Characterization and modeling the thermo-mechanical cure-dependent properties of epoxy molding compound. International Journal of Adhesion and Adhesives, *32*, 82–88.

Sanahuja, Julien (2013). Effective behaviour of ageing linear viscoelastic composites: Homogenization approach. International Journal of Solids and Structures, *50*(19), 2846–2856.

Saseendran, Sibin and Wysocki, Maciej and Varna, Janis (2016). Evolution of viscoelastic behavior of a curing ly5052 epoxy resin in the glassy state. Advanced Manufacturing: Polymer & Composites Science, *2*(2), 74–82.

Saseendran, Sibin and Wysocki, Maciej and Varna, Janis (2017a). Cure-state dependent viscoelastic poisson's ratio of ly5052 epoxy resin. Advanced Manufacturing: Polymer & Composites Science, *3*(3), 92–100.

Saseendran, Sibin and Wysocki, Maciej and Varna, Janis (2017b). Evolution of viscoelastic behaviour of a curing ly5052 epoxy resin in the rubbery state. Advanced Composite Materials, *26*(6), 553–567.

Sawant, Sourabh and Muliana, Anastasia (2008). A thermo-mechanical viscoelastic analysis of orthotropic materials. Composite Structures, *83*(1), 61–72.

Schapery, RA (1970). On a thermodynamic constitutive theory and its application to various nonlinear materials. Thermoinelasticity, Springer. 259–285.

Schapery, Richard A (1962). Approximate methods of transform inversion for viscoelastic stress analysis. Proceedings Fourth US National Congress of Applied Mechanics. vol. 2, 1075–1085.

Schapery, Richard Allan (1964). Application of thermodynamics to thermomechanical, fracture, and birefringent phenomena in viscoelastic media. Journal of Applied Physics, *35*(5), 1451–1465.

Schapery, Richard A (1969). On the characterization of nonlinear viscoelastic materials. Polymer Engineering & Science, *9*(4), 295–310.

Schapery, Richard Allan (1974). Viscoelastic behavior and analysis of composite materials. Mechanics of composite materials.(A 75-24868 10-39) New York, Academic Press, Inc., 1974,, 85–168.

Schieffer, Anne and Maire, Jean-Francois and Lévêque, David (2002). A coupled analysis of mechanical behaviour and ageing for polymer-matrix composites. Composites Science and Technology, *62*(4), 543–549.

Schneider, Konrad and Klusemann, Benjamin and Bargmann, Swantje (2017). Fully periodic rves for technological relevant composites: not worth the effort! Journal of Mechanics of Materials and Structures, *12*(4), 471–484.

Sherburn, Martin (2007). Geometric and mechanical modelling of textiles. Thèse de doctorat, University of Nottingham.

Sihn, Sangwook and Tsai, Stephen W (1999). Automated shift for time-temperature superposition. Proceedings of the 12th International Comittee on Composite Materials, *51*.

Simon, Sindee L and Mckenna, Gregory B and Sindt, Olivier (2000). Modeling the evolution of the dynamic mechanical properties of a commercial epoxy during cure after gelation. Journal of Applied Polymer Science, *76*(4), 495–508.

Sisodia, Sanjay M and Garcea, SC and George, AR and Fullwood, DT and Spearing, SM and Gamstedt, EK (2016). High-resolution computed tomography in resin infused woven carbon fibre composites with voids. Composites Science and Technology, *131*, 12–21.

Staub, S and Andrä, H and Kabel, M and Zangmeister, T (2012). Multi-scale simulation of viscoelastic fiber-reinforced composites. Tech. Mech, *32*(1), 70–83.

Stig, Fredrik and Hallström, Stefan (2012). Spatial modelling of 3d-woven textiles. Composite structures, *94*(5), 1495–1502.

Stig, Fredrik and Hallström, Stefan (2013). Influence of crimp on 3d-woven fibre reinforced composites. Composite Structures, *95*, 114–122.

Styan, George PH (1973). Hadamard products and multivariate statistical analysis. Linear algebra and its applications, *6*, 217–240.

Sullivan, RW (2006). On the use of a spectrum-based model for linear viscoelastic materials. Mechanics of Time-Dependent Materials, *10*(3), 215–228.

Sun, Xuekun and Sun, Changjie (2004). Mechanical properties of three-dimensional braided composites. Composite structures, *65*(3), 485–492.

Svanberg, JM and Altkvist, C and Nyman, T (2005). Prediction of shape distortions for a curved composite c-spar. Journal of reinforced plastics and composites, *24*(3), 323–339.

Tan, P and Tong, L and Steven, GP (1997). Modelling for predicting the mechanical properties of textile composites-a review. Composites Part A: Applied Science and Manufacturing, *28*(11), 903–922.

Taylor, Robert L and Pister, Karl S and Goudreau, Gerald L (1970). Thermomechanical analysis of viscoelastic solids. International Journal for Numerical Methods in Engineering, *2*(1), 45–59.

Tran, AB and Yvonnet, Julien and He, Q-C and Toulemonde, C and Sanahuja, J (2011). A simple computational homogenization method for structures made of linear heterogeneous viscoelastic materials. Computer Methods in Applied Mechanics and Engineering, *200*(45-46), 2956–2970.

Van der Sluis, O and Schreurs, PJG and Brekelmans, WAM and Meijer, HEH (2000). Overall behaviour of heterogeneous elastoviscoplastic materials: effect of microstructural modelling. Mechanics of Materials, *32*(8), 449–462.

Verpoest, Ignaas and Lomov, Stepan V (2005). Virtual textile composites software wisetex: Integration with micro-mechanical, permeability and structural analysis. Composites Science and Technology, *65*(15), 2563–2574.

Vieille, B and Albouy, W and Taleb, L (2016). Viscoelastic viscoplastic model for aeronautical thermoplastic laminates at high temperature: Validation on high stress gradient structures. Composites Part B: Engineering, *90*, 278–286.

Wang, Rongqiao and Zhang, Long and Hu, Dianyin and Liu, Chunhui and Shen, Xiuli and Cho, Chongdu and Li, Bo (2017). A novel approach to impose periodic boundary condition on braided composite rve model based on rpim. Composite Structures, *163*, 77–88.

Wang, Youqi and Miao, Yuyang and Swenson, Daniel and Cheeseman, Bryan A and Yen, Chian-Feng and LaMattina, Bruce (2010). Digital element approach for simulating impact and penetration of textiles. International Journal of Impact Engineering, *37*(5), 552–560.

Wang, Youqi and Sun, Xuekun (2001). Digital-element simulation of textile processes. Composites science and technology, *61*(2), 311–319.

White, SR and Hahn, HT (1990). Mechanical property and residual stress development during cure of a graphite/bmi composite. Polymer Engineering & Science, *30*(22), 1465–1473.

Williams, Malcolm L and Landel, Robert F and Ferry, John D (1955). The temperature dependence of relaxation mechanisms in amorphous polymers and other glass-forming liquids. Journal of the American Chemical society, *77*(14), 3701–3707.

Wu, Zhangjian (2009). Three-dimensional exact modeling of geometric and mechanical properties of woven composites. Acta Mechanica Solida Sinica, *22*(5), 479–486.

Xu, Yaoling and Du, Sansan and Xiao, Junhua and Zhao, Qingxin (2012). Evaluation of the effective elastic properties of long fiber reinforced composites with interphases. Computational Materials Science, *61*, 34–41.

Xu, Yingjie and Zhang, Pan and Zhang, Weihong (2015). Two-scale micromechanical modeling of the time dependent relaxation modulus of plain weave polymer matrix composites. Composite Structures, *123*, 35–44.

Yanjun, Chang and Guiqiong, Jiao and Bo, Wang and Wei, Liu (2006). Elastic behavior analysis of 3d angle-interlock woven ceramic composites. Acta Mechanica Solida Sinica, *19*(2), 152–159.

Zarrelli, Mauro and Partridge, Ivana K and D'Amore, A (2006). Warpage induced in bi-material specimens: Coefficient of thermal expansion, chemical shrinkage and viscoelastic modulus evolution during cure. Composites Part A: Applied Science and Manufacturing, *37*(4), 565–570.

Zarrelli, M and Skordos, AA and Partridge, IK (2002). Investigation of cure induced shrinkage in unreinforced epoxy resin. Plastics, Rubber and Composites, *31*(9), 377–384.

Zarrelli, M and Skordos, Alexandros A and Partridge, Ivana K (2010). Toward a constitutive model for cure-dependent modulus of a high temperature epoxy during the cure. European Polymer Journal, *46*(8), 1705–1712.

Zhang, HH and Li, LX (2009). Modeling inclusion problems in viscoelastic materials with the extended finite element method. Finite Elements in Analysis and Design, *45*(10), 721–729.

Zhou, E and Mollenhauer, DH and Larve, EV (2009). A realistic 3-d textile geometric model. Seventeenth international conference on composite materials ICCM-17, Edinburgh, United Kingdom.

Zhou, Guangming and Sun, Xuekun and Wang, Youqi (2004). Multi-chain digital element analysis in textile mechanics. Composites science and Technology, *64*(2), 239–244.

Zobeiry, Nima (2006). Viscoelastic Constitutive Models For Evaluation of Residual Stresses in Thermoset Composites During Cure. Thèse de doctorat, The University of British Columbia.

Zobeiry, Nima and Malek, Sardar and Vaziri, Reza and Poursartip, Anoush (2016). A differential approach to finite element modelling of isotropic and transversely isotropic viscoelastic materials. Mechanics of Materials, *97*, 76–91.